PICO-60: A Dark Matter Search Experiment with C_3F_8 in a Bubble Chamber

by

Pitam Mitra

A thesis submitted in partial fulfillment of the requirements for the degree of

Doctor of Philosophy

Department of Physics

University of Alberta

Abstract

The PICO-60 experiment was a bubble chamber for the search of Weakly Interacting Massive Particle (WIMP) dark matter. The previous run of PICO-60, conducted in 2013, was limited in sensitivity by background events that were most likely caused by particulate contamination and the buffer liquid. These backgrounds have been eliminated in the PICO-60 data presented in this thesis. Significant upgrades to the optics system enabled a new analysis leading to a larger fiducial volume and improved exposure. A new method to measure the temperature inside the PICO-60 vessel, which is otherwise impossible to instrument, was devised but not fully verified.

The data presented in this thesis shows that the PICO-60 bubble chamber runs stably at low threshold down to 2.45 keV and the ability to discriminate nuclear recoil events from α background events remains unchanged. A dark matter search was performed with $(51.96 \pm 0.14)\,\mathrm{kg}$ of C_3F_8 at nucleation threshold energies of $(3.29 \pm 0.05)\,\mathrm{keV}$ and $(2.45 \pm 0.05)\,\mathrm{keV}$. No dark matter candidate events were observed in the 3.29 keV data and three candidate events were recorded in the 2.45 keV data. PICO-60 established a world-leading upper limit on the spin-dependent WIMP-proton cross section of $\sigma = 3.15 \times 10^{-41} cm^2$ for a WIMP mass of $31.6\,\mathrm{GeV}$ from the 3.3 keV dataset.

Dedicated to my mother,
who is no longer here in person but in spirit to see me through completion.

It is important to do everything with passion, it embellishes life enormously.

– Lev D. Landau.

Acknowledgements

This dissertation has been work in progress for a long time and it would not have been possible without the support of many people who have come forward to stand by me over the years.

First and foremost, I would like to offer my deepest thanks and gratitude to my adviser, Dr. Carsten Krauss, for giving me the chance to work on this intellectually stimulating and challenging project. Through your exemplary mentorship and guidance I have become a better person today. Your enthusiasm, passion and dedication to experimental research have motivated me throughout my time as a graduate student. I admire you, have learned a great deal from you and you have shown me how to be a good scientist. I really appreciate the time and effort that you have dedicated towards me.

I would also like to express my special gratitude to Scott Fallows (who at the time was not yet the PICO analysis coordinator) for helping and supporting me throughout the project. To Scott: I appreciate the amount of time and effort you have put into helping me with everything, from my struggles using ROOT, to helping me decide on a clarinet to buy! I am thankful for the amount of patience and dedication that you have invested in me. You have pushed and inspired me to be a better scientist as we both learned a lot about the experiment together.

I also appreciate the encouragement and support I received from all the members of the PICO collaboration, especially Guillaume Giroux, Ken Clark, Hugh Lippincott, Andrew Sonnenschein, Dan Baxter, Mike Crisler, Ian Lawson, and Eric Dahl. I will fondly remember the days we spent working underground at SNOLAB and going for that pint of cold beer after the refreshing walk through the drift at the end of shift. I would also like to thank the personnel of SNOLAB, especially Lina Anselmo, for their support and teaching me a thing or twenty about cleanliness. I am grateful to Isaac Arnquist and Nicole Overman of PNNL, who trained me and offered technical guidance on assessing cleanliness. My work would not have been possible without the assistance I received from the technical staff at the University of Alberta NanoFab and the Department of Physics. Thanks to Shihong Xu for spending many hours training me on the technical equipment at the NanoFab. I would also like to acknowledge the assistance that Paul Davis and Len Wampler offered me throughout my program.

I would like to thank my peers at the department for their help and support, especially Logan Sibley for the words of wisdom as a senior graduate student. To Pawel, Courtney, Tom, Jie, Tania and Sarah: it was really a lot of fun to be here with you.

I am thankful for the endless amount of fun and love that my "Lindy-family" (Sugar Swing!) has given me. Birkley, Jenna, Krystal, Turlough, my friends in Mad Kittens and Cats and the dance floor: I could not have done it without you and I hope to be a part of the family for years to come!

No amount of thanks and gratitude would be enough to express the love and support that my mom and dad have given me unconditionally. I am grateful to them for the numerous struggles they had to go through in order to give me a better future in Canada. Without their dedication in my upbringing, I would not be where I am today.

Table of Contents

List of Figures

List of Tables

Statement of Originality

The research presented here was conducted as part of the PICO dark matter search collaboration. My contributions to the experiment were:

- I built a part of the optics hardware including building the camera acquisition system, and designing its controls and testing the hardware based trigger mechanism of the cameras. Relevant elements of this work are presented in Chapter 4.
- I performed the studies of the particulate background, their characterization and was instrumental in the determination that radioactivity alone cannot explain the anomalous events. I helped establish and developed procedures for cleaning and automated evaluation of samples at various stages of the experiment. Relevant parts of this work are reported in Chapter 5.
- I was responsible for a significant part of the detector operations.
- I designed, implemented and performed the optical reconstruction and analysis (AutoBub, cXYZ and Optometrist). This resulted in the complete elimination of human "hand scanning" of the data (Chapter 6).
- I analysed the data labelled as the 'complete exposure' of PICO-60 (Chapter 6 and 9).
- I conducted the radon timing studies presented in Chapter 7.
- The attempt at an event by event temperature reconstruction, presented in Chapter 8, is my work.

In the analysis of the PICO-60 data I used the acoustic analysis developed by other collaboration members and based the new 3D reconstruction algorithm on the existing ray tracing model. The analysis of the fast pressure excursion 'dytran' data is based on the work of other members of the PICO collaboration. I have also used the results of the GEANT4 simulations performed by the collaboration in the interpretation.

I certify that the content is my own and to the best of my knowledge has not previously been submitted to any other institute or university as a thesis. Any received assistance or used sources have been acknowledged.

Chapter 1

Introduction

The dark matter problem is one of the most fundamental and exciting open questions of particle physics. A modern day survey [1] of the universe reveals that only about 5% is baryonic matter. Many astrophysical observations have independently confirmed that the majority of matter in the universe accounting for the gravitational interactions is unidentified [2]. This unidentified matter does not interact with light, so it is invisible to direct observations [3].

One way to reconcile the astrophysical observations (explained in detail in Chapter 2) is to introduce “dark matter" consisting of cold, non-baryonic and neutral relic [4] elementary particles known as Weakly Interacting Massive Particles (WIMPs). The nature of these elementary particles is believed to be unlike any other fundamental particles decribed by the Standard Model of Particle Physics. WIMPs have a very low interaction cross section with ordinary matter. Dark matter search is an active area of investigation, with experiments around the world attempting to detect a WIMP signal. PICO (portmanteau of PICASSO and COUPP - two experiments that merged to form PICO) is one such experiment located at SNOLAB, near Sudbury, Ontario.

The PICO detectors use superheated liquid C_3F_8 as the target for elastic scattering measurement of WIMPs. Particle interaction causes a fluorine or carbon nucleus to recoil and subsequently deposit energy. If the energy deposition is larger than a threshold energy, the superheated liquid to undergo a phase change and boils locally. Piezoelectric sensors detect an acoustic signal produced from the rapid expansion of the resultant bubble, that can be used to distinguish between alpha decays and nuclear recoils. The fluorine present has an expected enhanced cross section to spin-dependent coherent WIMP-nucleus interactions, making PICO a primarily spin dependent dark matter search experiment (explained in Chapter 3).

This causes the detector to be insensitive to backgrounds with low energy density such as gamma rays or electrons. The threshold energy in a PICO detector is controlled by setting pressure and temperature.

PICO-60 CF_3I was the largest experiment operated by the PICO collaboration between 2013 and 2015 using 36.8 kg of CF_3I as an active liquid. The detector was upgraded and dark matter searches were performed with $(51.96 \pm 0.14)\,\mathrm{kg}$ of C_3F_8 at a threshold energy of $(3.29 \pm 0.05)\,\mathrm{keV}$, $(2.45 \pm 0.05)\,\mathrm{keV}$ and $(1.81 \pm 0.05)\,\mathrm{keV}$ in 2016 and 2017. A large fraction of the background events in the previous run of the PICO-60 experiment with CF_3I exhibited behaviours that acoustically mimicked nuclear recoils but were otherwise inconsistent with a dark matter signal [5]. Particulate contamination (see Chapter 5) was identified as the most probable cause of the anomalous background. A procedure was developed to identify the particulates and characterize them. This thesis describes the strategies developed to isolate, identify and mitigate particulates inside the active volume. A dark matter search was performed. An analysis of the data along with updated exclusion limits of dark matter search are presented in this thesis.

Chapter 2 discusses the known evidence for dark matter in our universe and possible candidates for the missing matter. The chapter touches on several independent astrophysical observations leading to constraints on dark matter properties. The chapter also includes a summary of the field and an overview of selected experiments that are looking for dark matter using a variety of targets and techniques.

Chapter 3 describes the theory of nucleation and particle detection using a superheated liquid. It also includes a review of the strengths of a bubble chamber in the scope of dark matter detection and the choice of target fluid for PICO.

Chapter 4 presents a discussion of the present PICO detectors and their construction. Details of the operation and the data collection are also presented.

Chapter 5 describes the mitigation of the particulate backgrounds. A method developed to sample particulate sources is described in this chapter. Results from the mitigation efforts are presented.

Chapter 6 introduces a new analysis of the PICO-60 dark matter search data including a new imaging technique that was developed. The selection criteria for runs, the fiducial volume selection and the methods used in the analysis of the acoustic data are presented in this chapter.

Chapter 7 describes the analysis of alpha particles in the PICO-60 detector using the C_3F_8 data. Timing correlations were used to identify alpha triplets arising from the decay of Uranium chain elements. The behaviour of their acoustic power was studied and is also described in this chapter.

Chapter 8 describes the growth of the bubbles observed in the detector. The work is ongoing and it paves a way to determining the thermodynamic conditions in the detector using this data.

Chapter 9 describes the improved dark matter search limit that PICO-60 was able to achieve. The conclusion and future scope of work is presented in Chapter 10.

Chapter 2

The Dark Matter Problem

First indications of the existence of dark matter were observed in the early 1920's [6]. In 1933, Fritz Zwicky provided detailed observations of the dynamics of the Coma cluster [7], demonstrating that the luminosity of a galaxy can provide at best the lower limits of its mass. By applying the virial theorem to the motion of the galaxies in the Coma cluster, he concluded that the galaxies in that cluster should have an average mass of 4.5×10^{10} solar masses. This corresponds to a mass-to-luminosity (M/L) ratio of about 500, in striking contrast with values of M/L = 3 that were considered normal. He conferred this missing mass the name âĂIJdunkle (kalte) MaterieâĂİ, meaning âĂIJdark (cold) matterâĂİ (also known as CDM). Today, there is an abundance of evidence for the existence of dark matter including that from galactic rotation curves [8], merger of galaxy clusters [9] and from the Cosmic Microwave Background (CMB) angular power spectrum [1]. This chapter introduces the concept of dark matter and motivates direct searches.

2.1 Evidence for Existence

In the past 30 years, significant effort has gone into understanding the nature of dark matter, and theories have been formulated in an attempt to explain the missing matter. Astrophysical observations of galactic rotation and of the large-scale mass distribution in the universe, measured using gravitational lensing, have been constructed [10] showing large deviations from the expectation based on visible matter alone. Observations of anisotropies of the CMB have determined the dark matter density of the universe [11]. These observations have been further improved with the Hubble expansion constraints calculated from Cepheid variable stars [12] and the luminosity-distance-redshift relations from distant type I-a supernova events [13]. All these different observations can consistently be explained by the existence of dark matter. Currently the model that best describes all available data is the Λ-CDM (Cold Dark Matter) model [14]. In this model, dark matter (CDM) is non-relativistic, non baryonic and has a very weak self interaction. A few examples showing the evidence of dark matter have been selected from a large range of fields such as observational astrophysics, microwave astronomy, and big bang nucleosynthesis, and are summarized below.

- **Rotation Curves**: Galactic rotation curves were one of the breakthrough pieces of evidences in support of dark matter in the universe. In 1970, Vera Rubin, Kent Ford and Norbert Thonnard measured the orbital velocity of stars in the Andromeda Galaxy (M31) and found that the velocity profile was not what was expected from Newtonian gravity [15]. In Newtonian mechanics, the rotational velocity of objects in the gravitational potential of a galaxy at a radius beyond the extent of the stellar disk is expected to follow $v(r) \propto r^{-1/2}$. Instead, it was found that the rotation curves exhibit a flat behaviour. This behaviour was seen in every spiral galaxy observed by Rubin in the next decade [8]. Rotational velocities of clouds of neutral hydrogen gas that extend far beyond the galactic disk were measured using the H-α spectral line. This allowed for a measurement of the orbital velocity of objects extended far beyond the galactic disk. The observed velocity profile remained flat in these objects, in agreement with Rubin's observation [16, 17]. An illustration is shown in Figure 2.1

  The rotation curves observed are consistent with the spiral galaxies being modelled by a flat disk, a central bulge and a spherical halo of dark matter that extends beyond the disk of a galaxy.

- **Mass to luminosity ratio of galaxy clusters**: Fritz Zwicky's analy-

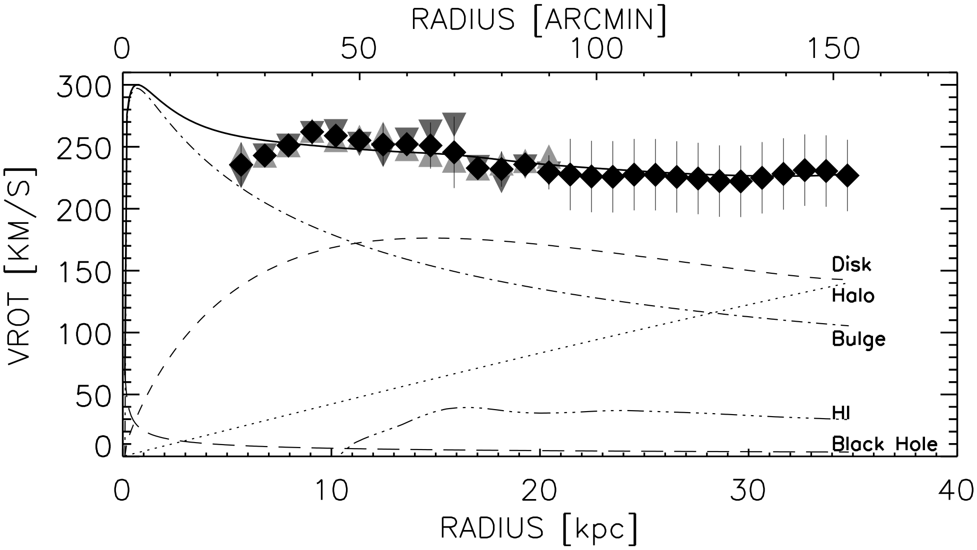

Figure 2.1: Rotation curve and mass model for M31 as presented in [17]. The upward pointing triangles (light grey) are for the receding side and the downward pointing (dark grey) triangles for the approaching side. Each mass component is identified. The solid line is the summation of the components contributing to the mass of the galaxy. A mass of $1.0 \times 10^8 M_\odot$ is used for the central black hole where $M_\odot$ is the mass of the sun.

sis of galaxy clusters using the visible stars, applying the virial theorem and comparing the mass to luminosity ratio, presented one of the earliest evidences of dark matter [7]. A modern version of the observation measures the X-rays emitted from the interstellar gas in such a cluster instead of the visible stars. Galaxy clusters contain plasma that is heated in the gravitational potential well of the cluster. The plasma then emits bremsstrahlung radiation (X-rays). By measuring the X-ray emission from such clusters with X-ray satellites like XMM-Newton [18] and Chandra [19], the mass of such a cluster can be calculated. The mass can then be compared with that of the visible baryonic matter and interstellar gas. Such a comparison reveals that the mass required to explain the dynamics of the cluster is much higher than the sum of the visible matter and the gas, indicating the presence of dark matter. A more comprehensive review of the baryon content of galaxy clusters in the local universe is given in [20].

- **Weak field lensing of colliding galaxy clusters**: The Bullet Cluster 1E 0657-558 [19] and the cluster MACS J0025.4-1222 [21] shown in Figure 2.2, are two pairs of galaxy clusters, each consisting of galaxy clusters which have collided in the past. The pink region is the hot gas as measured by X-ray images from Chandra. The blue region is the mass density as measured from gravitational lensing. The majority of the hydrogen is within the region near the center of the clusters while the majority of the mass extends much further away from the core. The explanation for this distribution is that the dark matter traversed the collision unhindered, while the baryonic component experienced drag. Thus the two centers of mass of the galaxy clusters (shown as the red outer contours in 2.2) have separated from the visible X-ray emitting components (shown as the yellow centre contours). The spatial offset of the center of total mass from the center of the baryonic mass peaks cannot be explained by modified gravity theories like MOND [22] and TeVeS [23]. The evidence here also supports the expectation that dark matter particles interact weakly [24].

- **CMB power spectrum**: The CMB is the electromagnetic radiation left over from the early stages of the universe and can be described by the Λ-CDM model. Today the CMB spectrum follows that of a blackbody at 2.73 K. In the early universe, the temperature was high enough that photons could not propagate freely. As the universe cooled, the matter de-ionized and the photons could travel freely. The CMB observed today reveals the energy density at the time when the universe became transparent to photons (also known as the “surface of last scattering") [2]. Anisotropies in the CMB yield a map of the distribution of the energy density in the early universe. The anisotropies can be used to derive the energy density of different components such as baryonic matter, dark matter and dark energy in the early universe in accordance with the Λ-CDM model. To derive the ratios of each component in the Λ-CDM model, the CMB spectrum is expressed as a power spectrum of

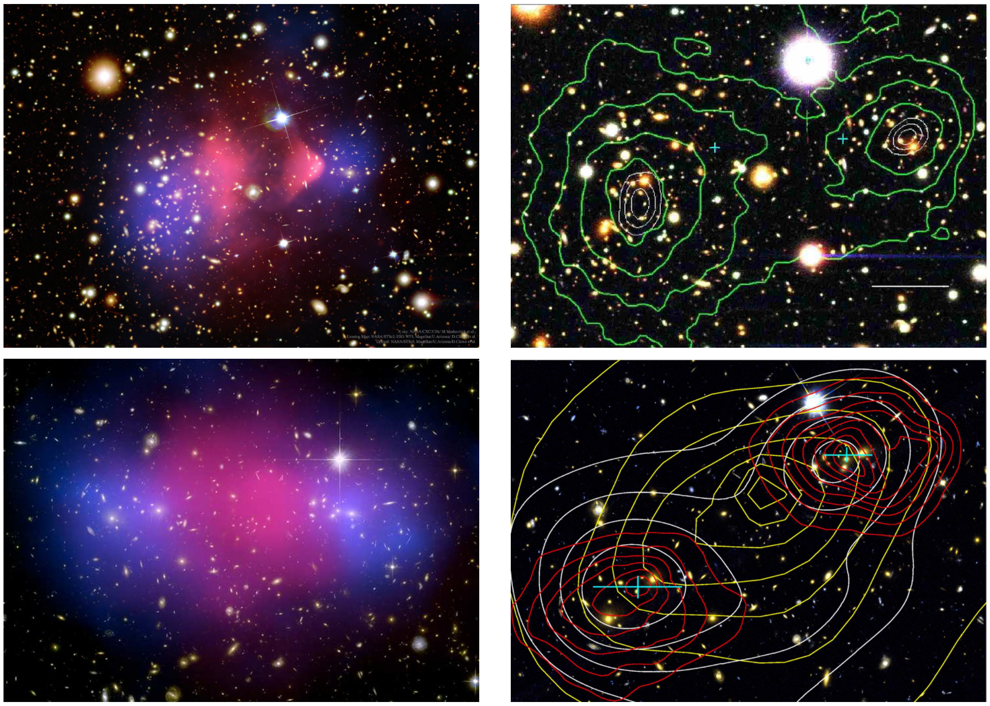

Figure 2.2: Composite image of mass distributions from weak gravitational lensing (blue) and x-rays (pink) on Hubble telescope images of 1E 0657-56 bullet cluster [9] [19] and MACS J0025.4-1222 [21]. A clear separation is observed between the distribution of baryons (hot interstellar gas) and the mass responsible for the lensing. Note that the image in the bottom right is rotated with respect to the one on the left of it.

spherical harmonics. This is shown in Figure 2.3. The amount of radiation can be inferred from the measured temperature of the CMB and the thermal history [2]. The series of third or higher acoustic peaks in the CMB power spectrum are sensitive to the energy density of dark matter. Fitting those peaks to the Λ-CDM model of the universe gives the dark matter density. This is important because this measurement is independent of all other astronomical observations and confirms the existence of dark matter in the early universe. The results from the CMB studies yield an energy density fraction from dark matter at Ω_{dm}=0.2589±0.0057 [1] of the total energy density, which is in agreement with the studies from Cepheid variable stars and type-Ia supernovae [25].

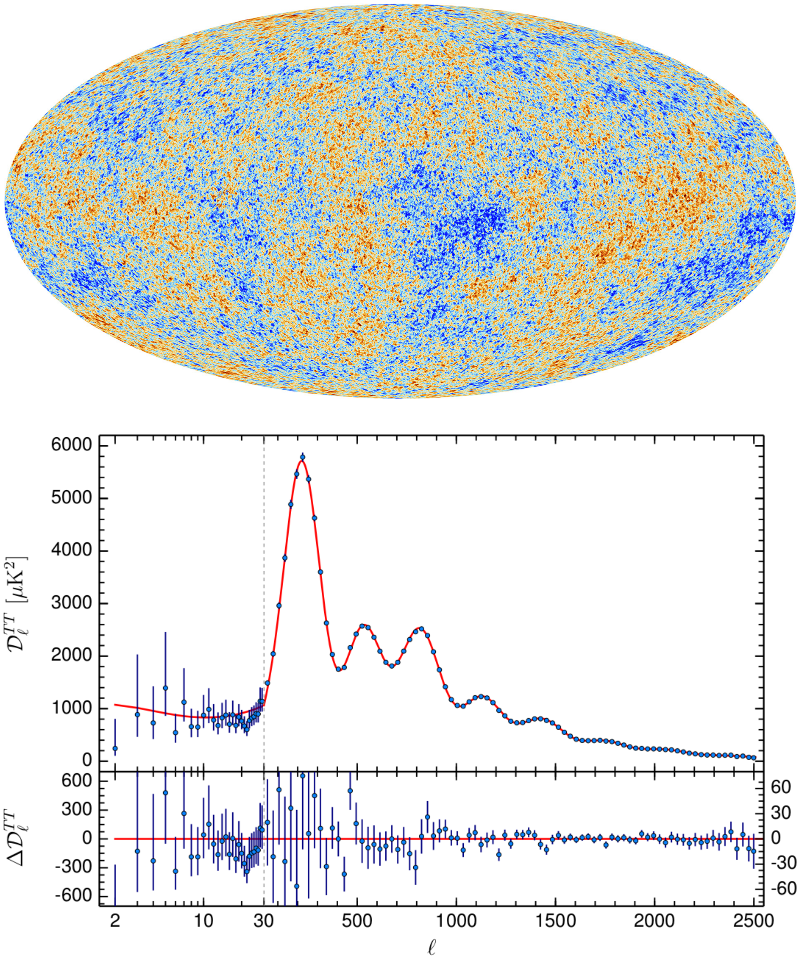

Figure 2.3: The Cosmic Microwave Background (CMB) anisotropy (top) and the power spectrum (bottom), as measured by PLANCK [25]

2.2 Nature of Dark Matter

There is an abundance of evidence for the existence of dark matter as described in the previous section. Yet the precise nature of dark matter remains to be understood. This is primarily because all of the indications arise from the gravitational effects of dark matter. A number of properties of dark matter particles can be informed from the observations, a summary of which is presented here.

- **Non-baryonic in nature**: The density parameter Ω is defined as the ratio of the observed density of a certain component of the universe to the critical energy density of the universe [26]. From the CMB data collected by COBE [27], WMAP [28] and then PLANCK [25], the density parameter of baryonic matter in the universe has been determined by PLANCK to be Ω_b=0.0486±0.0010. This density includes MACHOs (Massive Compact Halo Objects), like black holes and faint stars that cannot be accounted for in astronomical surveys. The dark matter in the universe is predominantly non-baryonic, meaning it cannot be non-exotic baryonic objects that are “too faint to be seen" [11].

- **Electromagnetically Neutral**: Dark matter should be “dark" by definition. Dark matter should not have coupled strongly with photons when the very first electrically neutral atoms formed in the universe (called the recombination epoch). This places limits on the interaction of dark matter with photons yielding a limit on the dipole moment of dark matter particles: [D, M] $< 3 \times 10^{-16} e$ cm for masses less than a few GeV and [D, M] $< 10^{-24} e$ cm for larger masses, where D is the electric dipole moment and M is the magnetic dipole moment [3].

- **“Cold” or Slow Moving**: For the measured CMB anistropies to agree with the baryon acoustic oscillation model [29], dark matter should be able to form gravitational wells in the early universe. In addition, dark matter should be able to form halos around galaxies and other large scale structures in the universe. A requirement for this behaviour is for dark matter to be slow moving i.e., it must possess a nonrelativistic velocity. Indeed, dark matter n-body simulations show that the radial velocity of dark matter particles in the Milky Way galaxy should follow a generalized gaussian with a mean velocity of 224 km/s [30].

- **Interacts “weakly”**: A requirement of dark matter particles is that they do not couple strongly with baryonic particles during the recombination epoch after the big bang. Otherwise, this would be inconsistent with the observed peaks in the CMB power spectrum. If the coupling were strong, the baryon-dark matter fluid would radiatively cool, affecting structure formation. Many theories beyond the Standard Model predict Weakly Interacting Massive Particles (WIMPs) as possible dark matter candidates that weakly interact with baryons [31]. If produced thermally in the early universe, WIMPs would have a relic abundance which is consistent with the dark matter abundance today, and hence they are the most studied class of dark matter candidates. In addition to weakly interacting with other baryons, dark matter particles should exhibit weak self-interactions. Constraints on the self-interaction of dark matter particles may be placed from astrophysical observations like the Bullet Cluster ($\frac{\sigma}{m} \leq 0.47\ \mathrm{cm}^2\mathrm{g}^{-1}$ [32]) and from gamma-ray and positron emissions observed by satellites like Fermi-LAT [33] and AMS-02 [34]. A more comprehensive review of the mechanism is presented in Section 2.3.1 on indirect dark matter searches.

- **Stability**: The dark matter, if produced in the early universe, must be stable on cosmological time scales otherwise it would have affected the CMB anisotropies during the recombination epoch and the large scale structures today. Theories predicting multiple dark matter particles decaying into the lightest dark matter particle are severely constrained by the requirement that such a decay may not disrupt the dark matter structure formation [35].

2.2.1 Dark matter candidates: Particle physics and the nature of dark matter

The most favoured model of dark matter that fits all the observations is that of a yet unseen particle. Many candidates that fit such a particle description of dark matter have been proposed to account for the astrophysical observations. A quick review of all known particles from the Standard Model rules out all but the neutrinos. However neutrinos cannot be the dark matter particles because of two main reasons. Firstly, the dark matter candidate should be able to form galactic halos [36], so the particles' mean free path should be of the galactic scale or smaller. Neutrinos do not satisfy this requirement since they rarely ever interact with any other particles and their mean free path is much larger than the size of a galaxy. Secondly, the CMB anisotropy measurements, combined with large-scale structure data, may be used to calculate the physical neutrino density of the universe. The density is constrained to $\Omega_\nu \leq 0.0062$ [25]. This is not enough to account for the dark matter contribution to the energy density of the universe.

Two of these well-motivated theories are more appealing and most favoured because they were introduced to solve some specific shortcomings of the Standard Model of particle physics, with the possibility of a solution to the dark matter problem arising naturally as well. The two candidates are Axions and WIMPs.

Axions are pseudoscalar particles proposed by Peccei-Quinn as a solution to the strong CP problem [37]. Axions are theorized to have been produced non-thermally in the early universe. The Axion Dark Matter Experiment (ADMX) searches for axions with a tunable microwave resonant cavity with a large axial magnetic field. Axions would be detected through the Primakoff effect i.e., through their conversion into microwave photons in the magnetic field of the cavity [38].

WIMPs, motivated by supersymmetry [39], on the other hand are massive GeV scale particles that couple weakly to gauge bosons. This theory gained credibility by the fact that a WIMP annihilating after the big bang creates a dark matter density that is identical to the one observed in the universe today. This is called “the WIMP miracle" [4] . The theory postulates that in the early universe, WIMPs and standard model particles were created in thermal equilibrium. The reaction can be represented by

$$\chi\chi \leftrightarrow \text{SM SM}. \tag{2.1}$$

As the temperature of the universe dropped the radiation pressure required to maintain the SM SM → $\chi\chi$ reaction was no longer energetically available. Dark matter could still annihilate, but not be created.

$$\begin{aligned} \chi\chi &\rightarrow \text{SM SM}, \\ \chi\chi &\not\leftarrow \text{SM SM}. \end{aligned} \tag{2.2}$$

This causes the dark matter density to fall with the expansion of the universe until the annihilation is no longer possible since the dark matter particles are far away from each other to interact with an appreciable rate. The remaining dark matter is then effectively “frozen". With the assumption that freezing happens when the timescale for annihilation is proportional to the Hubble time, one can show that

$$\langle \sigma v \rangle \propto \frac{\alpha^2}{m_\chi^2}. \tag{2.3}$$

Since the scale of the thermal cross section $\langle \sigma v \rangle$ of interaction is that of electroweak couplings the most favoured physics of dark matter interactions is electroweak. Additionally the density of dark matter that would be present during the freeze-out is strikingly similar to the one measured from astronomical observations. This mechanism and observations provide a strong motivation for dark matter being WIMPs and they are the most studied class of dark matter candidates. A graph showing the density of dark matter in the early universe and the “freeze-out" is shown in Figure 2.4.

The present model of the WIMP dark matter candidate assumes a local density of the dark matter halo on the order of 0.3 GeV/cm^3, and a velocity of the Earth through the dark matter halo of 230 km/s. The local WIMP flux is estimated to be 10^5 cm^{-2} s^{-1} [40].

2.3 Detection methods

Astrophysical observations permit estimating the properties of dark matter in bulk, including its density, but do not allow one to determine its particle properties. To determine these, experiments must be designed to measure the microphysical properties of dark matter particles; namely their interaction cross section with other dark matter particles and Standard Model particles, and their mass. Detection methods for particulate dark matter can be broadly

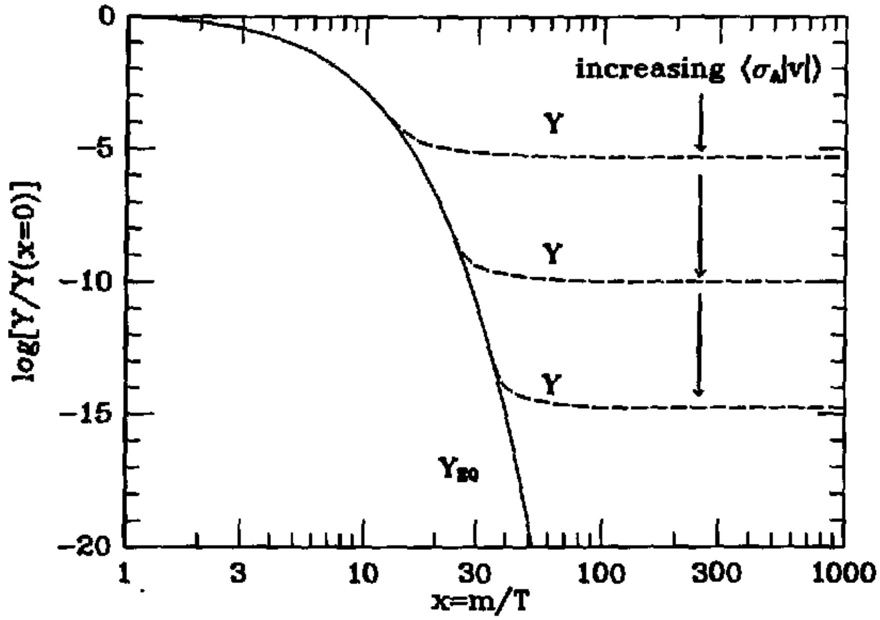

Figure 2.4: Relative density of dark matter shown as a function of the Hubble time since the Big Bang. The dark matter “freezes out" at a timescale of the Hubble time. The graph was taken from [4].

classified into three categories: direct detection, indirect detection and collider production.

2.3.1 Direct detection

Direct detection of dark matter is based on the possibility of detecting the resultant nuclear recoils produced by the rare interactions of the dark matter particles with the (target) material in detectors. Two kinds of nuclear interactions can be envisaged, a spin independent coupling and a spin dependent coupling [41].

The Feynman diagrams of such interactions are presented in Figure 2.5. The Z-exchange and the squark exchange diagrams contribute to the spin dependent interaction, whereas the Higgs exchange contributes to the spin independent interaction. The subject of this thesis is the direct search for coherent spin dependent interactions between dark matter particles and the nuclei of the target material.

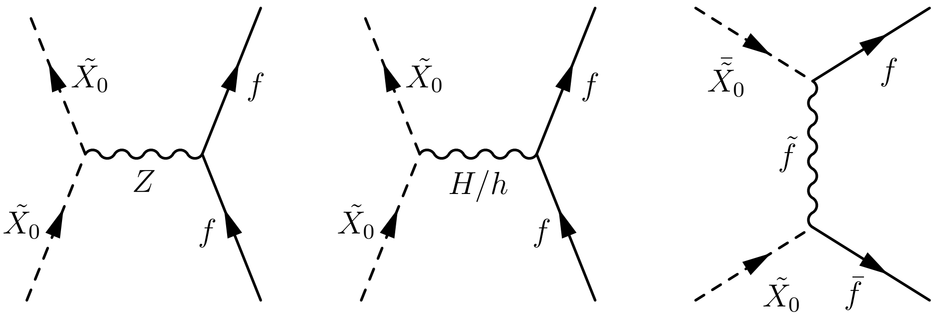

Z - exchange Higgs exchange Squark exchange

Figure 2.5: The Feynman diagrams for direct detection dark matter searches involving Z exchange, Higgs exchange and squark exchange.

2.3.2 Indirect detection

In the supersymmetry framework [39], the particles with the lowest energy are stable and known as neutralinos. They are one of the most favoured WIMP candidates for dark matter. They are Majorana particles that allow the possibility of annihilation in neutralino-neutralino interactions. If this model is correct, annihilation products can be expected from regions of the sky where the abundance of dark matter is presumably high (dwarf spheroidal galaxies and the centre of the Milky Way). The annihilation may produce several kinds of Standard Model particles [35].

Some associated Feynman diagrams of these interactions are presented Figure 2.6. In the first case, neutralinos can annihilate into two photons mediated by the Z-boson. The Fermi-LAT (Large Area Telescope) experiment and the VERITAS (Very Energetic Radiation Imaging Telescope Array System) gamma ray telescope [42] are used to look for gamma rays arising from such interactions.

A second mechanism is by production of electrons and positrons. No other known mechanism exists for the production of positrons in cosmic rays originating from galaxies that are mostly composed of dark matter (dwarf spheroidal galaxies). A detection of excess amounts of positrons can therefore

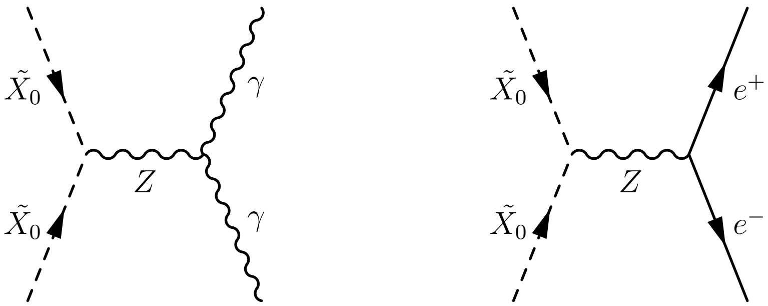

Figure 2.6: Two specific Feynman diagrams for indirect detection dark matter searches involving Z exchange.

be used to set limits on the interaction cross section of the neutralino [42].

Some experiments, such as the IceCube neutrino telescope [43] at the South Pole and the ANTARES [44] neutrino telescope have the capability to detect dark matter annihilation neutrino signals from the Sun and other regions of the sky with an expected high dark matter density. The neutralino interacts with a proton in the Sun and loses some kinetic energy. The remaining kinetic energy may not be enough to escape the Sun's gravitational well, and these particles gather at the centre of the Sun where they may undergo annihilation. Out of the particles produced from the annihilation, only neutrinos can escape from the centre of the Sun. The mechanism of production of neutrinos from such a scenario is shown by the Feynman diagrams in Figure 2.7. Such interactions are primarily sensitive to spin dependent interactions since the interaction of neutralinos with protons in the sun is spin dependent.

2.3.3 Collider production

The Large Hadron Collider is a particle accelerator which aims to create the conditions prevalent in the early universe. Under such conditions the SM SM $\rightarrow \chi\chi$ reactions become possible. Detectors look for missing energy from such collisions and infer the presence of dark matter [45].

No signals with conclusive dark matter signatures were observed with either of the three approaches outlined.

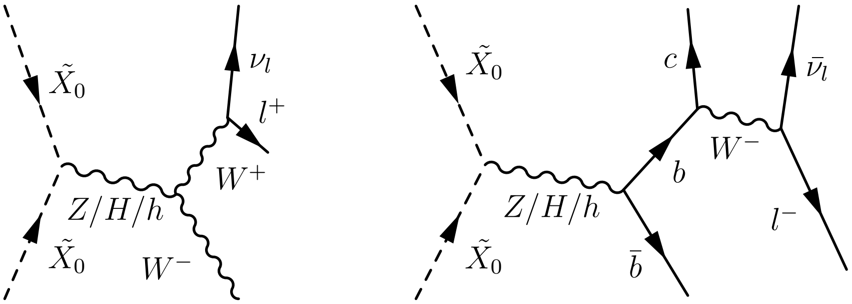

Figure 2.7: Predicted neutralino interactions at the center of the sun [43].

2.4 Principles and methodologies of direct dark matter detection

The preferred methodology of direct detection experiments for the search for a WIMP dark matter particle is coherent elastic scattering of a WIMP with a target nucleus [46]. In the range of momentum exchange of interest, the spin independent interaction has equal coupling to protons and neutrons (in the minimal supersymmetric model) and the rate scales as the square of the atomic mass of the target nucleus. The spin independent cross section of a neutralino interaction is given as a function of the event rate by [41] [47]

$$\frac{dR}{dQ} = \frac{\rho}{m_\chi} \times \frac{\sigma_0 A^2}{2\mu_p} \times F^2(Q) \times \int \frac{f(v)}{v} dv, \tag{2.4}$$

where $\frac{dR}{dQ}$ is the rate in events/kg/keV. The terms in the equation are:

- $\frac{\rho}{m_\chi}$ is the dark matter density term. It is derived from astrophysical observations;
- $\frac{\sigma_0 A^2}{2\mu_p}$ is the unknown particle physics part with cross section σ_0 and the reduced mass $\mu_p = \frac{m_p m_\chi}{m_p + m_\chi}$, where m_χ is the mass of the neutralino, m_p is the mass and A is the atomic mass of the target nuclei. The A^2 term is the enhancement factor for spin independent interactions; and
- $F^2(Q)$ is a form factor. When the momentum transfer Q in a WIMP-nucleon collision is such that the wavelength h/Q is no longer large

compared to the nuclear radius, the effective cross section begins to fall with increasing Q. F is given by $F^2(Q) \propto e^{-Q/Q_0}$ where Q_0 is given by $80/A^{5/3}$ MeV [41].

- The last term, $\int \frac{f(v)}{v} dv$ arises from the velocity distribution of WIMPs in the galaxy.

In spin dependent interactions the equation takes the form of [48]

$$\frac{dR}{dQ} = \frac{\rho}{m_\chi} \times \frac{\sigma_0 (c_n \langle S_n \rangle + c_p \langle S_p \rangle)^2 \frac{J+1}{J}}{2\mu_p} \times F^2(Q) \times \int \frac{f(v)}{v} dv. \tag{2.5}$$

The enhancement in this case is given by $(c_n \langle S_n \rangle + c_p \langle S_p \rangle)^2 \frac{J+1}{J}$, where c_p and c_n are the effective proton and neutron coupling strengths, J is the total nuclear spin, and $\langle S_p \rangle$ and $\langle S_n \rangle$ are the expectation values of the proton and neutron spins within the target atom. Only direct detection experiments can provide limits on neutron couplings, but the proton coupling can be probed by both direct detection experiments and the indirect searches for neutrinos arising from WIMP annihilations in the core of the sun.

In any direct dark matter search experiment, the energy of the WIMP is not directly measured but is reconstructed from the energy of a recoiling nucleus or electron. The nuclear recoil is a result of a coherent WIMP-nucleon elastic scattering. Standard model particles and cosmic rays can initiate nuclear or electron recoils as well, so dark matter experiments need to be located deep underground to keep them shielded from cosmic rays and spallation neutrons. Experiments must also be made of radio-pure materials and must be shielded from neutrons from the environment, e.g., the surrounding rock. Direct detection experiments can employ different methods for discrimination of background events against nuclear recoils and various technologies have evolved over time for this purpose. In the following section, a few selected technologies for direct dark matter searches are listed and the experiments were classified based on the technology that is employed for detection of nuclear recoils and discrimination of background events.

2.4.1 Superheated liquids

The PICO [5] (previously PICASSO [49] and COUPP [50]) and SIMPLE [51] experiments use bubble chambers to search for dark matter. The detectors use a superheated liquid as an active target. PICO uses C_3F_8 which gives the detector an excellent spin-dependent sensitivity due to the unpaired proton spin in Fluorine [48]. The superheated liquid is meta-stable and an energy deposition from a nuclear recoil can induce a bubble nucleation. The threshold energy required for nucleation is given by the Seitz model [52] and can be regulated by controlling the temperature and pressure of the superheated liquid. Nuclear recoils depositing an energy larger than the threshold within a critical amount of volume (given by a critical radius parameter) trigger nucleation. Both β and γ events do not deposit their energy in this critical volume because they lose their energy over a comparatively long range (Chapter 3). PICO is therefore insensitive to minimally ionizing radiation. This is described in more detail in Section 3.3.

Alpha particles are a dominant background in the PICO detector. Alpha particle events from the walls of the detector can be discriminated against by using a fiducial volume cut. However alpha particle emission from decay of radon originate in the fiducial volume. This type of background can be discriminated against by using the acoustic waveform of a nucleation event. The PICO detectors have piezo-electric sensors to collect the acoustic signal from nucleation events. When an event is caused by an alpha particle, some energy is deposited and proto-bubbles are created along the track while the recoiling daughter nucleus creates another proto-bubble. The proto-bubbles merge on expansion. This phenomenon has an acoustic signature that is several times more energetic (louder) than a single nuclear recoil event. PICO thus uses this acoustic signature to discriminate nuclear recoil events from alpha decays.

2.4.2 Noble liquids

Xenon and argon are noble liquids that are used for dark matter searches. Both liquids scintillate. Xenon is an excellent target for direct detection of WIMPs because its large atomic mass renders it with a large spin independent coherent WIMP scattering cross section ($\propto$ A^2). Xenon is also radio-pure and has a high density. Due to this density and a large atomic number xenon has a short interaction length for gamma rays making a large detector self-shielding and generating a clean inner volume for dark matter searches[46].

Liquid argon is similar to liquid xenon in most properties. A few notable differences are that in liquid argon the timing structure of the scintillation pulse depends upon the nature of the event and allows for pulse shape discrimination of nuclear versus electron recoils. Liquid argon, unlike xenon, has unstable isotopes ^{39}Ar and ^{42}Ar that are radioactive. Experiments thus use depleted argon from deep underground sources where the concentration of the radioactive argon is lower than in atmospheric argon[46] or be able to discriminate against scintillation events generated by the radioactive argon.

2.4.2.A Single phase scintillator

DEAP is a liquid argon based experiment at SNOLAB [53]. It is a vessel that is filled with $\sim$ 3300 kg of liquid argon. The detector is spherical to maximize light collection and has photo multiplier tubes all around the vessel. Liquid argon is a scintillator with emission in the hard ultraviolet. Although the total amount of light is proportional to the deposited energy the time structure of the scintillation light depends on the ratio of scintillation light from the long lived excited triplet state and the short lived singlet state. The nature of the particle interactions with Ar affect this ratio and the shape of the pulse can be used to discriminate between electron recoils and nuclear recoils [54]. This technique is known as pulse shape discrimination (PSD) and is used by DEAP. The expected background after discriminating the electron recoils are neutrons arising from photo-multiplier tubes (PMTs). To mitigate this the PMTs are mounted 50 cm away from the vessel wall and light guides made of acrylic transport the light from the vessel to the PMTs.

2.4.2.B Dual phase electroluminescent time projection chambers

Dual phase detectors have a liquid phase with a gas phase at the top. The detector is fitted with a drift cathode. High quantum efficiency photomultiplier tubes (PMTs) are placed at the top and bottom of the cylindrical detector vessel. Xenon and argon are transparent to the scintillation light they produce. The PMTs are coated with a wavelength shifter to convert the scintillation light from ultraviolet to visible [55].

When a charged particle interacts with the xenon in the time projection chamber (TPC) it ionizes xenon in its track. Xe ions recombine to yield scintillation light producing electroluminiscence signal S1. The remaining electrons in the TPC drift upward under the influence of a drift field. The electric field extracts the electrons into the gas phase producing scintillation signal S2. The S2 signal is detected as delayed coincidence compared to S1. Nuclear recoils have a higher energy density compared to minimally ionizing particles (MIPs) and thus they have a higher ion recombination. The ratio of the S2 to S1 signal is used to discriminate nuclear recoils against other types of events [56].

The limitations of a xenon time projection chamber are the recombination length of the drift electrons in the xenon that is dependent on the purity of the xenon. The purity is affected by oxygen and nitrogen contamination that becomes an additional challenge at large scales due to outgassing from the detector material. The most competitive dark matter search experiments using Xe TPCs are LUX, Xenon and PandaX [46].

Dual phase argon time projection chambers use the same basic design. DarkSide is one such experiment. Liquid argon experiments can use pulse shape discrimination in addition to the the ratio of the S1 and S2 signals to discriminate nuclear recoils from background events.

2.4.3 Cryogenic solid state

Cryogenic solid state detectors were developed to distinguish the dominant electron recoil backgrounds from nuclear recoils on an event-by-event basis.

The technology was pioneered by the CDMS (Cryogenic Dark Matter Search) collaboration, and the present detectors' greatest strength lies in detection of low mass WIMPs. Experiments such as SuperCDMS, EDELWEISS and CRESST use charge and phonons to analyze interactions in the detector's active mass [46].

In the CDMS experiment, the ionization electrons are drifted and collected by two concentric electrodes on one face while on the other face four channels of superconducting transition edge sensors collect phonons generated by the interaction. Combining the signals gives a powerful way to discriminate nuclear recoils from electron recoils. The dominant background in such detectors comes from β emission at the surface and gamma ray emission from the material used to build the detectors [57].

2.4.4 New technologies and directional dark matter searches

As the sensitivities of large dark matter experiments approach the coherent neutrino-nucleus scattering level, dark matter searches could be forced to use directionality to exclude the neutrino background from the sun [46]. Such technologies are in the research and development phase right now. In addition to directionality, several experiments are being designed to search for dark matter in parameter spaces set by well-motivated theories [44] such as sub-GeV dark matter which are dark matter particles with masses between the meV and the GeV scale. A few selected experiments are described here.

2.4.4.A DAMIC-1K

The DAMIC experiment uses Si-based charge-coupled devices (CCDs) as the target for dark matter searches. DAMIC-1K is a low background and a low threshold experiment [44]. The target mass is 1 kg. The DAMIC-1K experiment will use skipper CCD sensors developed by the SENSEI collaboration [58]. These are low noise CCDs where the charge in each pixel can be measured to sub electron noise levels. DAMIC-1K will search for dark matter with a mass range of 1eV to a few GeV and will be sensitive to DM-electron scattering and hidden sector dark matter [59]. DAMIC-1K also aims to show the rejection of cosmogenic ^{32}Si which is crucial in paving a path to probing low mass dark matter interactions down to the neutrino floor.

2.4.4.B NEWS-G

New Experiments With Spheres-Gas (NEWS-G) is a dark matter search experiment that uses light noble gases in spherical proportional counters for the search of dark matter [60]. The advantage of such an experiment is that the detectors are sensitive to low mass WIMPs since the target material is light. The collaboration aims to look for dark matter with masses of ∼0.1 to 1 GeV. The detectors are metallic hollow spheres and equipped with a ball sensor in its centre. These sensors are set to a high voltage and the detectors are operated in the proportional counter mode at up to 10 bar pressure. The NEWS-G experiment has operated a prototype detector at Laboratoire Souterrain de Modane, and is preparing for the next version of the experiment at SNOLAB.

2.4.5 PICO's position in the dark matter experiment landscape

Today a diverse program for direct dark matter detection exists but no evidence of dark matter as a particle has been observed. Most experiments are setting limits on the interaction cross section of dark matter particles. The PICO bubble chamber detectors are scalable and have demonstrated a low background and have produced a world leading sensitivity. PICO is competitive in the search for spin dependent dark matter that couples to protons. The chambers can work with diverse target nuclei. PICO's competition in the field of the spin-dependent dark matter search is LZ and indirect dark matter searches like IceCube.

The background for the coherent neutrino scattering from atmospheric and solar neutrinos is two orders of magnitude lower for PICO than other direct detection experiments like Xenon or LZ. This is due to the light target material that has a lower coherent cross section for MeV scale solar neutrinos than Xe based experiments [61]. Thus PICO is unique in this regard. In addition to this, PICO can switch target fluids and can exploit additional WIMP-standard model particle scattering mechanisms like the proton angular orbital momentum coupling to Iodine in CF_3I or using hydrofluorocarbons for the search of low mass WIMPs. The following chapter explains the technology of this experiment in more detail.

Chapter 3

Particle Detection with Bubble Chambers

Bubble chambers are a class of particle detectors that employ superheated liquids as target. Particle detection in superheated liquid detectors requires a threshold energy deposition as well as a minimum energy density. This dual threshold feature allows this class of detectors to be made naturally insensitive to electromagnetic interactions and thus statistical discrimination between electron recoils and nuclear recoils is not required. This feature makes these detectors competitive in the landscape of dark matter search experiments. When a particle deposits energy in the superheated liquid the liquid undergoes a phase transition. The gaseous phase of the liquid occupies a much bigger volume than that of the liquid. The expansion is very rapid and causes acoustic pressure waves, which are transmitted through the detector and are picked up by piezo-electric acoustic sensors. PICASSO, COUPP and the merged collaboration PICO have demonstrated the ability to discriminate alpha background from nuclear recoils based on this acoustic signature [62].

3.1 Why a Bubble Chamber?

The reasons for selecting a bubble chamber and the active liquid that was chosen, along with their justification, can be summarized in terms of a “wish list" as

- Large and scalable target mass: PICO-60 operated with a target mass of about 50 kg but the technology does not change much if a 500 kg PICO detector were to be built. The active liquid (whether it is C_3F_8 or CF_3I) is inexpensive compared to xenon or other target materials such as germanium.

- Low energy threshold: The detector had the ability to be stably operated at 1.8 keV Seitz energy threshold.

- Multiple target nuclei: As outlined by [63], it is important to use multiple target nuclei to maximize the chances of detection of dark matter. PICO has the ability to change target fluids and as long as the thermodynamic range for superheating the fluid is not too different from the current fluid. A dark matter search can readily be performed with a completely new target. This was demonstrated when PICO-60 changed the active liquid from CF_3I to C_3F_8. This unique ability can be used to probe for dark matter using different couplings in the effective field theory (EFT) model by switching between different target nuclei (See Section 3.2.3).

- Zero background: After a long campaign, described in Chapter 5, PICO-60 has demonstrated a background-free dark matter search run with a threshold of 3.3 keV and an exposure of 1167 kg·days [64].

3.1.1 Gamma Rejection

One of the prime motivations of building a bubble chamber for dark matter searches is the ability of the device to reject gamma interactions. From Figure 3.1 it is evident that both a threshold energy and a threshold energy density is necessary for bubble nucleation. Gamma interactions can provide the necessary energy but cannot provide the energy density to cause nucleation in the bubble chamber and thus PICO-60 is inherently insensitive to gamma interactions (and similarly to beta decays). The gamma flux of the chamber was measured at very low thresholds. The flux was fitted to an exponential decay and shown in Figure 3.2. Results for PICO-60 operated at 3.3 keV Seitz threshold showed that the gamma nucleation probability is extremely small; on the order of 10^{-9}. From Figure 3.2, it is estimated that at 2.4 keV Seitz threshold the gamma background is 0.34 ± 0.31 events in an exposure of 1404 kg days.

3.2 Selection of the Target Fluid

Bubble chambers are capable of operating with different target fluids, so a target fluid is selected that offers the best chance for the detector to interact with dark matter, while offering complementarity with other dark matter searches. PICO-60 uses C_3F_8 as active liquid to look for spin-dependent dark matter interactions. The material must: be superheated at, or near, room temperature; not react with quartz or with water which is used as a buffer fluid; be dense, yet have a low surface tension. C_3F_8 satisfies all these conditions, with a boiling point of -19.7 °C at 30 psi (the operating pressure in a vast majority of PICO-60 runs), low reactivity with most materials, and a density of 1367 kg/m^3. It is also economical at ∼\$200/kg compared to the target materials for many other dark matter search detectors. For these reasons, it is a very good choice of target material from an engineering standpoint.

3.2.1 Complementarity with Spin-Independent Dark Matter Searches

Dark matter searches in the spin-independent sector have an advantage in probing new parameter space of interest because of the A^2 enhancement [65], reflected in the success of noble gas detectors with large active mass. Xe and depleted Ar are radio-pure and can be obtained in large quantities. Detectors utilizing Xe and Ar are thus simple to scale and can conduct dark matter search in a significant section of the allowed parameter space. Fitzpatrick et al [66, 63] suggest that the mechanism of interaction may be complicated and provide a graph of spin dependent (SD) versus spin independent (SI) parameter space of several candidates of dark matter from various theories to 1,2 and 3 σ confidence intervals. This graph is shown in Figure 3.3. The figure

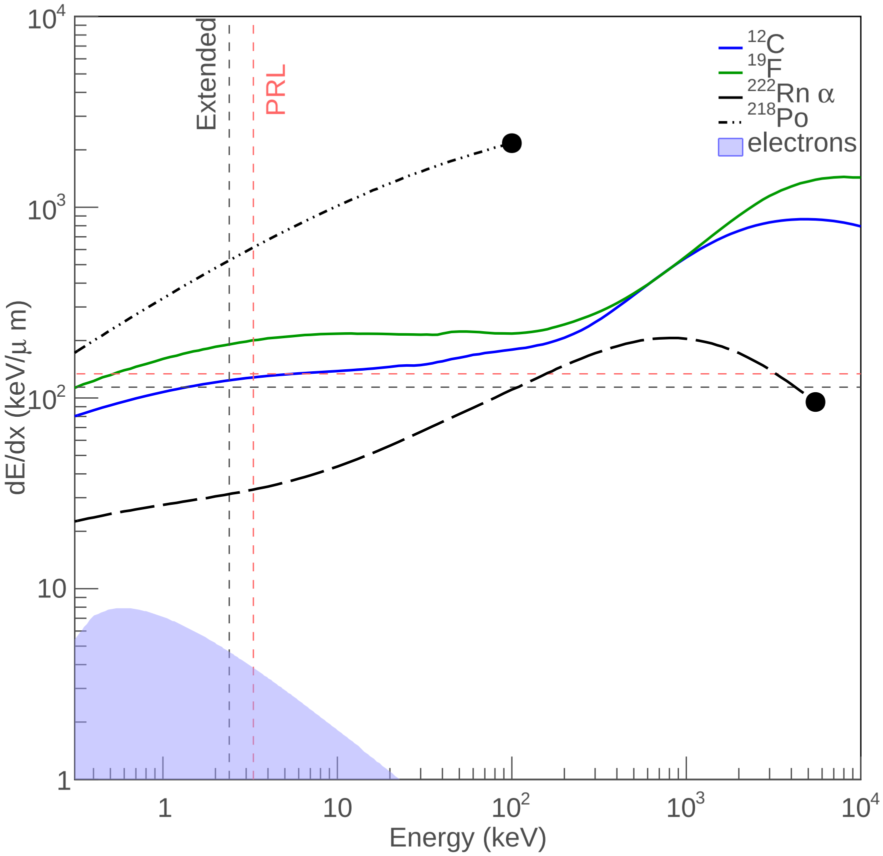

Figure 3.1: Energy loss of tracks of different particles in C_3F_8. The dashed lines show the run conditions of the experiment at 3.3 keV (14.05 °C, 30 psi - the analysis presented in [64] labelled as "PRL") and 2.4 keV (16 °C, 30 psi - the data presented in this thesis labelled as "extended"). Only recoils that cross both thresholds are able to nucleate bubbles in the detector. It can be seen that the chamber is insensitive to electron recoils.

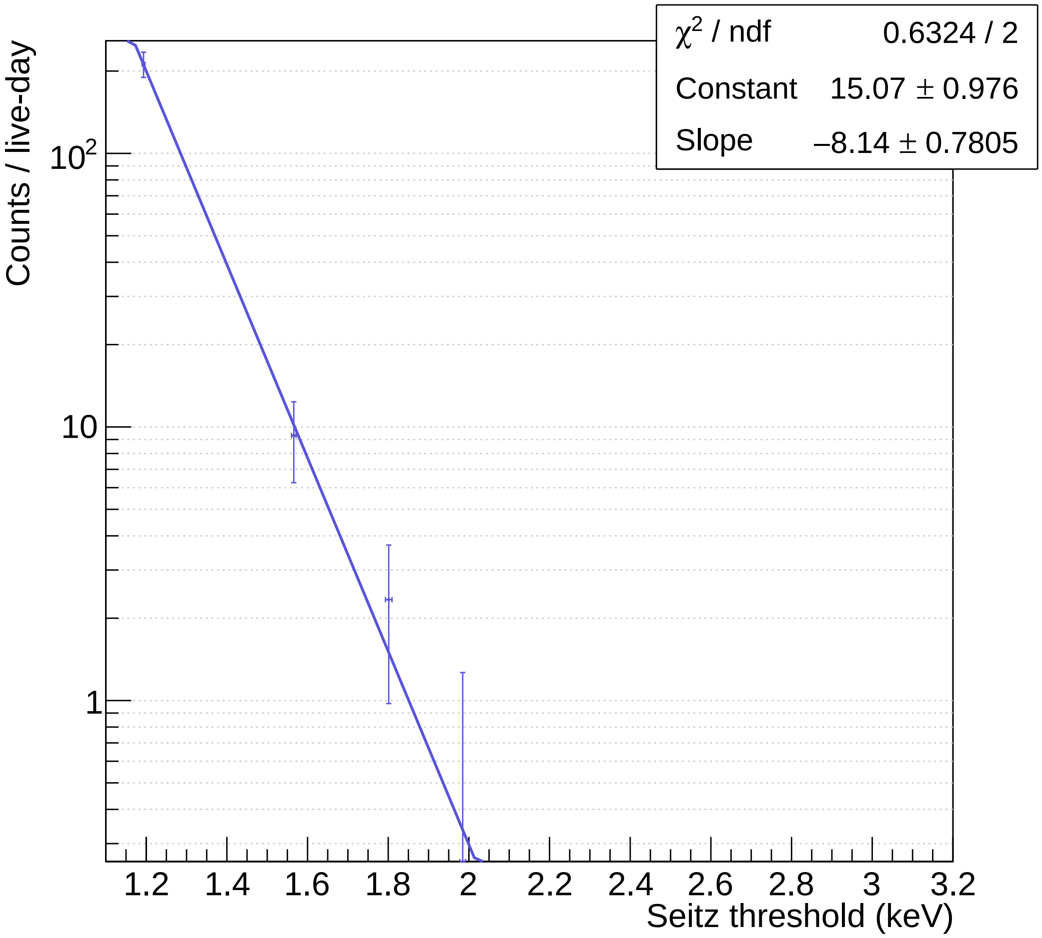

Figure 3.2: The environmental gamma event rate in PICO-60 at various thresholds. The rate has been fitted to an exponential decay function. Dividing the observed rate by the expected number of gamma interactions, obtained from simulation gives the gamma nucleation probability.

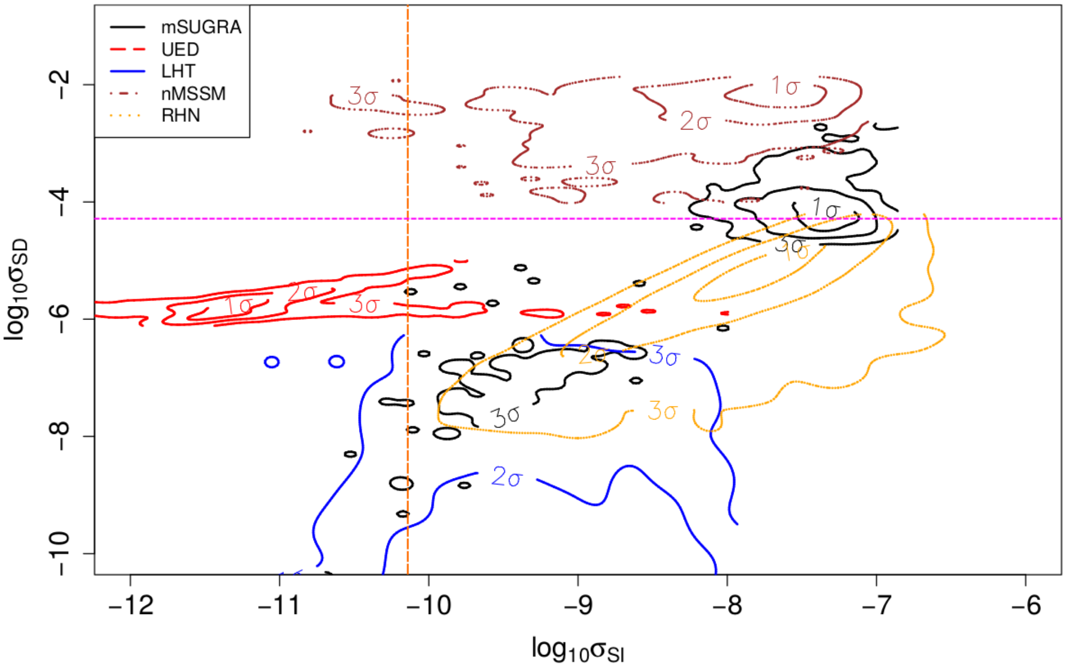

Figure 3.3: Spin independent (SI) vs Spin dependent (SD) cross section predictions according to different theories and models taken from [67]. The units are in log(picobarns) on both axes. The most stringent limit in the SI space is $\sigma_{SI} = 7.7 \times 10^{-11} pb$ for a WIMP mass of 35 GeV (XENON1T, 2017 [68]) has been marked with the orange dashed line. The best limit in the SD space is $\sigma_{SD} = 4.12 \times 10^{-5} pb$ for a WIMP mass of 31 GeV from this thesis has been marked with a pink dashed line.

demonstrates that, for the set of theories presented, every model predicts that dark matter interacts in both the spin-independent and the spin-dependent parameter space. Spin independent and spin dependent searches are thus complementary. PICO is currently the leading spin dependent direct dark matter search experiment [64].

3.2.2 Complementarity with Collider Searches

It is theorized that direct pair production of dark matter particles may be possible in TeV scale collisions at the LHC [69]. If such particles are produced then their presence would be inferred not from direct measurements but from missing energy or a large imbalance in the total transverse momentum of particles produced from an interaction. This kind of interaction is called a

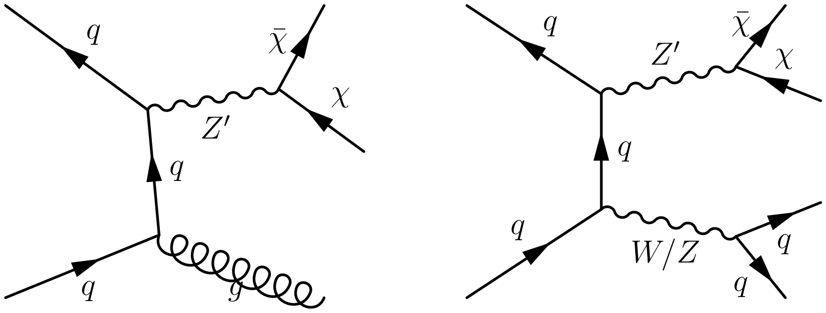

Figure 3.4: Tree level Feynman diagrams of monojet (left) and mono-V (right) production and decay of a spin-1 mediator particle that is used for dark matter searches in the LHC experiments [45].

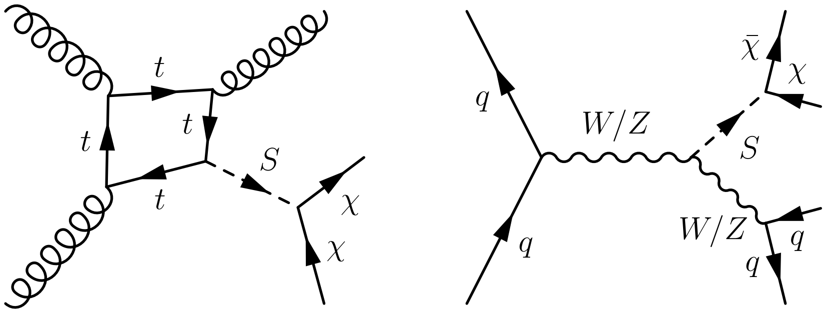

Figure 3.5: Tree level Feynman diagrams of monojet (left) and mono-V (right) production and decay of a spin-0 mediator particle that is used for dark matter searches in the LHC experiments [45]

“monojet" final state. The dark matter particles may also be produced in conjunction with an electroweak boson such as the W or Z particle. Such interactions are known as “mono-V" final state where V stands for “Vector boson". Observation of such final states of interaction may be used as evidence for dark matter particles, and conversely, the lack thereof can be used to set limits on the dark matter particle interaction cross section or the mediator particle masses [70]. The leading order Feynman diagrams of the models of monojet and mono-V interactions to search for dark matter in the LHC are shown in Figure 3.4 where the mediator particles carry a spin of 1. The corresponding graph for spin-0 mediators are shown in Figure 3.5.

In the Large Hadron Collider experiments the simplified models [45] considered for dark matter search analysis by LHC dark matter working group are identified by a set of four parameters: the dark matter mass m_{DM}; the mediator mass m_{med}, the coupling of the mediator particle to quarks g_q, and;

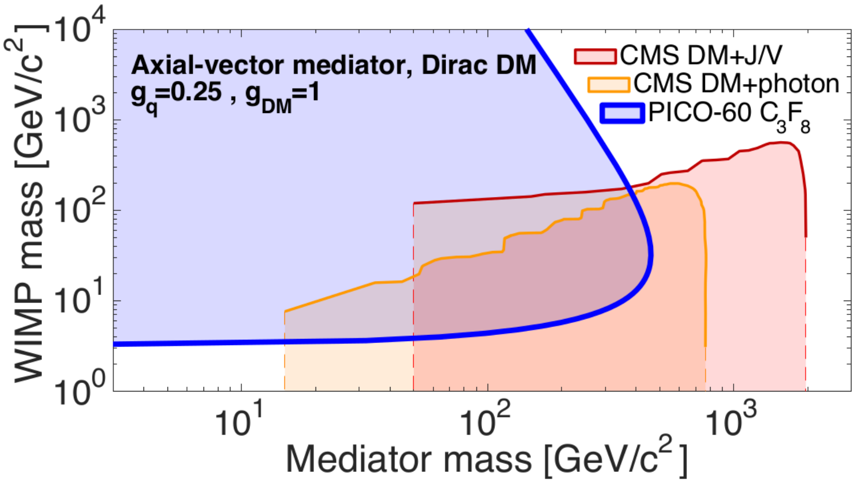

Figure 3.6: Exclusion limits with 95% C.L. in the mediator mass-wimp mass plane of PICO, along with CMS with an axial-vector mediator using a monojet (red), and monophoton (orange) channels taken from [64]

the coupling of the mediator particle to dark matter g_{DM}. Furthermore, in the simplified model of [71], used to compare the PICO-60 results, the values of g_q and g_{DM} were fixed at 0.25 and 1, respectively, according to the simplified model. Collider results are presented as a function of mediator mass and dark matter mass, and are complementary to direct dark matter searches. A graph of the limits set by Compact Muon Solenoid (CMS) experiment [45] at the Large Hadron Collider using the axial-vector monojet channel for dark matter search is shown in Figure 3.6 in comparison with the limit set by PICO-60 [64]. The complementarity of the two different techniques and their reaches on the parameter space for dark matter searches is demonstrated by this figure.

3.2.3 Capability to Probe Different EFT Couplings

PICO can use different target materials for dark matter searches. A chart of sensitivities of different target materials to the WIMP-proton operators is presented in Figure 3.7. In this chart, the coupling of the different target materials to dark matter is represented with respect to their nuclear properties. The parameters represented are the standard spin-independent response (M_p), spin angular momentum (transverse spin angular momentum Σ' and the longitudinal component Σ''), the transverse angular momentum Δ and the representations of $\langle S \cdot L \rangle$ which are Φ' and Φ''. In the WIMP-proton sector, iodine is a good target for Φ_p'' and Δ_p while Fluorine is good for the spin dependent couplings Σ' and Σ''. In the WIMP-neutron sector Xe is an excellent target material with broad coverage of almost all the couplings. Since PICO can switch targets (most easily between F and I in this chart), it can take advantage of the complementarity of the couplings of these two targets. Fluorine and Iodine offer the ability to probe different effective field theory (EFT) couplings.

3.3 Physics of Bubble Nucleation - the Seitz Hot Spike Model

The theory of the behaviour of superheated liquids was originally described by F. Seitz, M. S. Plesset, S. A. Zwick and P. Dergarabedian [52],[72],[73]. A superheated liquid can only exist below what is known as the thermodynamic limit of superheat T_{th}. The limit separates the metastable states from the thermodynamically unstable states, and a superheated fluid will cease to exist as a liquid above this phase boundary. This limit is important because it is the definition of reduced superheat, defined as $s = (T - T_b)/(xT_c - T_b)$, where T is the temperature of the liquid, T_b is the boiling point, $xT_c = T_{th}$ is the thermodynamic limit of the superheated liquid expressed as a fraction x of the critical temperature T_c. The reduced superheat is used in the definition of the energy threshold of PICO detectors. Using the Van-der Waal's equation of state, the limit is found to be $T_{th} = 0.844T_c$, where T_c is the critical temperature. It is practically impossible for a detector to reach the thermodynamic limit of superheat. This is because a second kinetic limit of superheat is defined by the bubble nucleation probability, where the mean time of creating a nucleation bubble becomes so short that it is not practically possible to superheat the liquid any further. This limit is lower in temperature than the thermodynamic limit.

In the Seitz model of bubble nucleation, a metastable superheated liquid

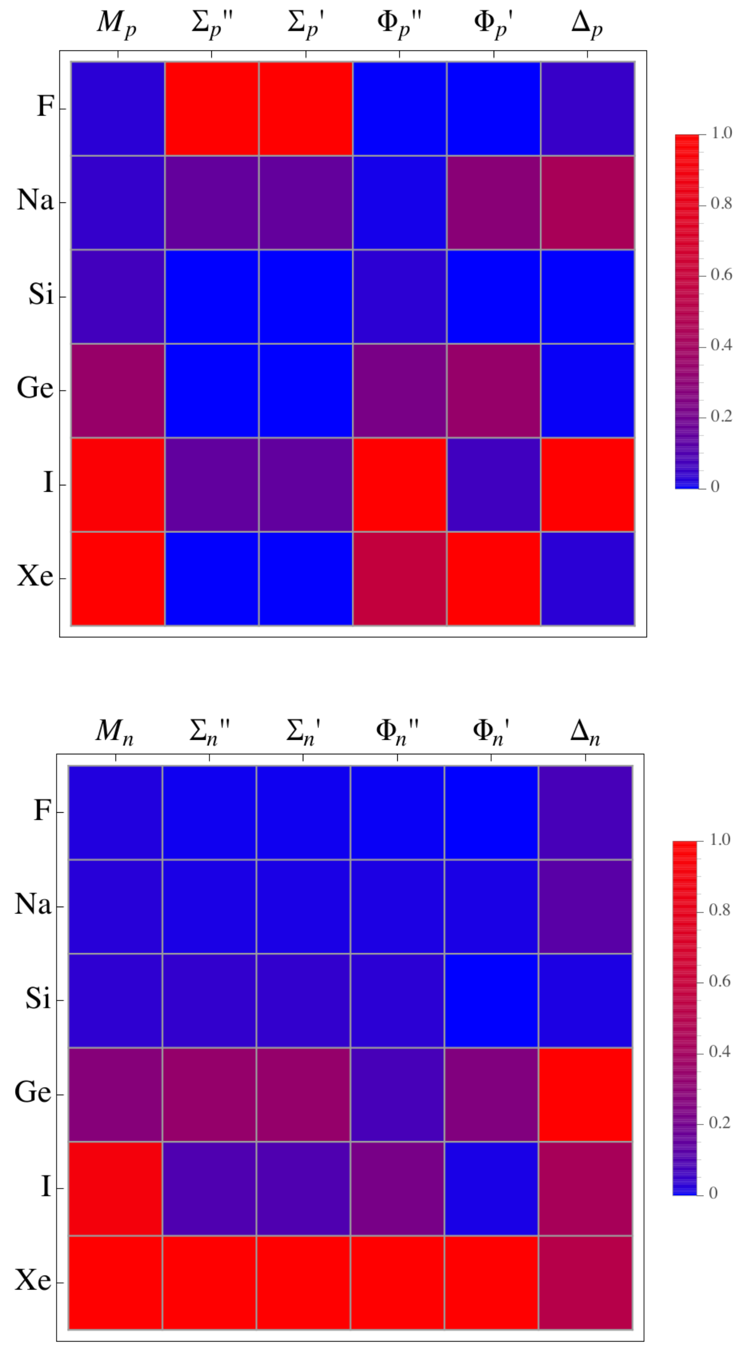

Figure 3.7: Detector target proton responses (top) and neutron responses (bottom) to different EFT WIMP-nucleon couplings taken from [66, 63]. The colour scheme is the normalized size of the integrated form factors for different nuclear responses weighted by the natural abundances of isotopes. The descriptions of the couplings are given in the text.

receives a concentrated amount of energy in the form of a particle interaction with the atoms of the liquid material (as in a “hot spike") and a vapour bubble is formed within it. This proto-bubble is in an unstable equilibrium and is surrounded by the superheated liquid. To create the proto-bubble, an energy of σA is required where σ is the surface tension of the liquid and A is the surface area of the bubble. The energy needed to form a nucleation bubble can be calculated in two steps. The work done by liquid molecules in entering the proto-bubble and then expanding to volume V is given by W= PΔV. If a constant number of molecules are vaporized at a constant pressure P_V into a bubble of constant area where the pressure of the surrounding liquid is P_L then the work done by the bubble is given by

$$W_1 = (P_V - P_L)V_G', \tag{3.1}$$

where V_G' is the volume of the bubble at pressure P_V. To model the work due to expansion, the number of molecules is kept constant while the volume is expanded from V_G' to V_G. Here P_G is the pressure of the gas in the bubble when it expands to the volume V_G.

$$W_2 = \int_{V_G'}^{V_G} (P - P_L)dV = P_G V_G - P_V V_G' - P_L(V_G - V_G') - \int_{P_V}^{P_G} V dP, \tag{3.2}$$

$$W_2 = P_G V_G - P_V V_G' - P_L(V_G - V_G') - x(\mu_G - \mu_L), \tag{3.3}$$

where μ is the chemical potential, and x is the number of molecules in the bubble. The total energy requirement to create a nucleation bubble is then given by W=σA-W_1-W_2 or

$$W = \sigma A - (P_G - P_L)V_G + x(\mu_G - \mu_L). \tag{3.4}$$

Equation 3.4 is the fundamental equation of bubble nucleation. Figure 3.8 shows the total energy balance as a function of the bubble volume. From this figure it can be inferred that a minimum amount of energy is required to form

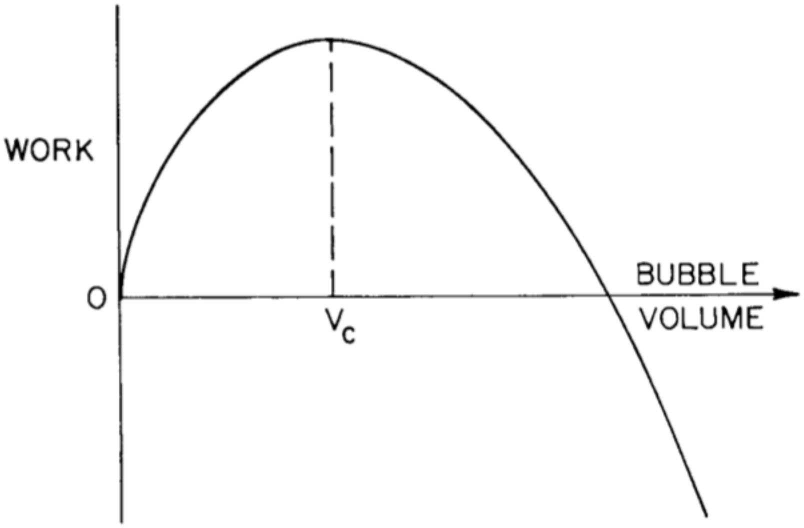

Figure 3.8: Work with respect to bubble volume. V_C represents the critical volume. Figure taken from [74].

a bubble. If the amount of energy deposited is less than this minimum, the proto-bubble collapses.

The critical radius of the bubble can be found by taking the derivative of the fundamental equation of bubble nucleation with respect to r, setting it to zero, and then substituting P_G=P_V.

$$P_V - P_L = \frac{2\sigma}{r_c} \tag{3.5}$$

In this equation r_c is the critical bubble radius. The minimum energy needed to form a nucleation bubble can then be derived as [52]

$$E = 4\pi\sigma R^2 + \frac{4\pi}{3}R^3 nH, \tag{3.6}$$

where n is the number of moles of gas produced in the proto-bubble and H is the latent heat of sublimation, and R is the gas constant. The quantities in this equation are not measurable practically. So from an experimental standpoint, the equation can be further simplified in terms of measurable quantities to give

$$E = 16\pi\frac{\sigma^3}{P^2}(1 + \frac{2H}{3ZRT}), \tag{3.7}$$

where Z is the compressibility factor of the liquid. This is the amount of energy that needs to come from an external source for a superheated liquid to undergo nucleation. This serves as a threshold energy for bubble nucleation and is called the “Seitz threshold". In the case of PICO, this energy is supplied by particle interactions with the active liquid. The implication is that, if a particle interaction deposits less energy than this amount, a bubble nucleation does not happen. The vertical lines in Figure 3.1 highlight the Seitz thresholds. It can be seen that minimally ionizing particles usually do not deposit enough energy to cause a bubble nucleation. In addition to the Seitz threshold, another condition must be met to nucleate bubbles a minimum energy density in a nuclear recoil track. Section 3.3.1 describes the energy density requirement in detail.

3.3.1 Stopping Power Threshold

The Seitz threshold is the thermodynamic threshold of nucleation in a liquid. However the particle depositing the energy in the liquid needs to be able to do so within the critical radius of the bubble r_c. The typical scale of r_c in the operating range of PICO-60 is ∼20 nm. The simplest model of such a criteria is a step function defined by

$$\frac{dE}{dx} \geqslant \frac{E}{ar_c}, \tag{3.8}$$

where a is an unitless scaling parameter, first modeled by Harper and Rich and thus known as the Harper factor [75]. Various values of a have been suggested by different authors[76] [77]. The dE/dx versus energy of a particle as it slows down has been plotted in Figure 3.1 assuming the Harper factor to be unity. This figure illustrates the stopping power threshold of the bubble detector and the sensitivity to alphas, electrons and nuclear recoils. Regions that show the run conditions for [64], and the extended physics run of PICO-60, are marked in the figure. The figure also shows the dual nature of the nucleation threshold of the bubble chamber. Only those tracks inside the square formed at the top right of Figure 3.1 by the dashed lines (operating conditions as determined by the pressure and temperature) produce nucleations. Particles such as electrons do not provide enough energy density to trigger a nucleation in the detector.

By varying pressure or temperature, the threshold for stopping power and energy can be varied in the bubble chamber and is used to eliminate electron recoil background.

3.4 Stages of Growth of the Bubble

Once formed, the nucleation bubble grows through several stages. The following list outlines the information obtained at different time scales in the growth of the bubble. This list highlights the regime at which the acoustic signals that PICO uses are emitted. It also shows the additional stages of growth that PICO has the ability to observe and the types of information that can be gained by studying the bubble growth in these regimes.

1. Particle interaction ($\sim$10^{-16}s): Interaction of a charged particle or a nuclear recoil with the target nuclei. The length scale is of the order of 10^{-15}m. [78]

2. Transfer of kinetic energy ($\sim$10^{-13}s): At this scale the kinetic energy from a recoiling nucleus or an electron is transferred to its surrounding medium.

3. Emergence of proto-bubble ($\sim$10^{-10}s to $\sim$10^{-9}s): At this time scale the target nuclei around the nucleation region have sufficient energy to form a gas phase and proto-bubbles emerge. The length scale is <10 nm. An acoustic emission happens as well.

4. Kinetic growth ($\sim$10^{-9}s to 10^{-4}s): In this phase of growth, the proto-bubble grows because of the difference in the vapour pressure inside the bubble and the pressure of the liquid outside the bubble. The growth rate is given by [74]

$$\frac{dR}{dt}\bigg|_{kin} = \bigg[\frac{2p_v(T) - p}{2\rho}\bigg]^{1/2}, \tag{3.9}$$

where R is the bubble radius, t is the time, ρ is the liquid density, $p_v(T)$ is the vapour pressure of the liquid as a function of temperature, and p is the pressure inside the chamber. The expansion is adiabatic and the vapour cools as it expands. The growth rate drops over time until it is dominated by thermal expansion. The length scale is between 50nm and 200 μm.

The acoustic signal used by PICO is emitted in this phase. An alpha particle track is several microns long, nucleating multiple proto bubbles whereas a nuclear recoil track is ~50 nm in length and nucleates only a single proto-bubble. Bubbles in this phase produce acoustic emissions with an intensity given by the formula [79]

$$I = \frac{\rho \ddot{V}^2}{4\pi c}, \tag{3.10}$$

where V is the volume of the bubble, and c is the speed of sound. If a spherical bubble is assumed (with volume as $\frac{4}{3}\pi \mathrm{R}^3$) then the expression for the intensity of sound evaluates to

$$I = \frac{16\pi \rho \phi_k^6}{c} t^2, \tag{3.11}$$

where ϕ_k is dR/dt given in Equation 3.9. It can be seen that the intensity of the sound increases with time in this regime.

5. Thermal growth ($> 10^{-4}$s): After the adiabatic growth of the bubble in the previous stage, the gas is cooler than the surroundings. Heat transfer from the liquid into the bubble will continue its expansion. This regime is known as thermal growth. Mathematically the rate of expansion is given by [74]

$$\left.\frac{dR}{dt}\right|_{th} = \left[\frac{3}{\pi}\right] \frac{k}{L\rho_v} \frac{T - T_b}{(Dt)^{\frac{1}{2}}}, \tag{3.12}$$

where T_b is the boiling point, L is the liquid thermal conductivity, ρ_v is the gas density inside the bubble and D is the thermal diffusivity. This equation can be shortened to

$$\frac{dR}{dt} = \phi_t \frac{1}{2\sqrt{t}}. \tag{3.13}$$

Assuming a spherical bubble yields the intensity of sound emitted as

$$I = \frac{16\pi\rho\phi_t^6}{4c}\frac{1}{t}. \tag{3.14}$$

The intensity of the sound emission decreases with time in this regime. This is the phase of growth that can be optically observed. Studying the bubble growth in this regime may be used to get direct measurements of temperature T of the liquid since all the other quantities are either known or can be calculated or are functions of T.

Equations 3.11 and 3.14 indicate that the intensity of the sound emitted by the bubble as it grows first increases and then decreases. Assuming that the acoustic signal is continuous, it is possible to estimate the time-scale at which the thermal growth starts to dominate. This is given by $\tau = (\phi_t/\phi_k)^2 \sim 100\mu$s with the data from [80, 81].

3.5 Alpha versus Neutron Discrimination - Theory

Recoiling nuclei and alpha particles have very different mechanisms of depositing energy in the target material. From Figure 3.9, an alpha track is able to meet both conditions for nucleation in multiple places along its track, whereas a nuclear recoil will be able to generate a single proto-bubble. The acoustic emission from a protobubble is a function of the rate of change of volume displaced by the gas in the proto-bubble (Equation 3.11 and 3.9). It is thus expected that an alpha track with multiple proto-bubbles would have a larger acoustic emission than a nuclear recoil track with a single proto-bubble. As the proto-bubbles of the alpha track grow, they start to merge. The acoustic energy emitted at this stage by the merged bubble of the alpha track is still higher than the spherical bubble of the nuclear recoil tracks since the rate of volume displacement is higher. Surface tension eventually forces the merged growing bubble of the alpha track to become spherical and, at this point, any further discrimination between this bubble and that of a nuclear recoil is lost. An illustration of the physics of this discrimination between alpha decays and nuclear recoils is shown in Figure 3.9. The time-scale where the acoustic signal is different between an alpha particle and a nuclear recoil lies within the kinetic growth phase. The mechanism of the discrimination is not fully understood, so a quantitative prediction of the magnitude of the difference of acoustic signal amplitudes is not available.

Section 3.4 describes that a signal from the kinetic growth regime originates in the first 100 µs after the bubble genesis, which corresponds to frequencies above 1 kHz. Thus the optical data is not expected to be able to resolve alpha decays from nuclear recoils. Piezoelectric sensors are used to measure the acoustic energy released in each event and this data is used to discriminate between alpha decays and nuclear recoils. The details of the technical implementation and analysis of the data are presented in Chapter 6.

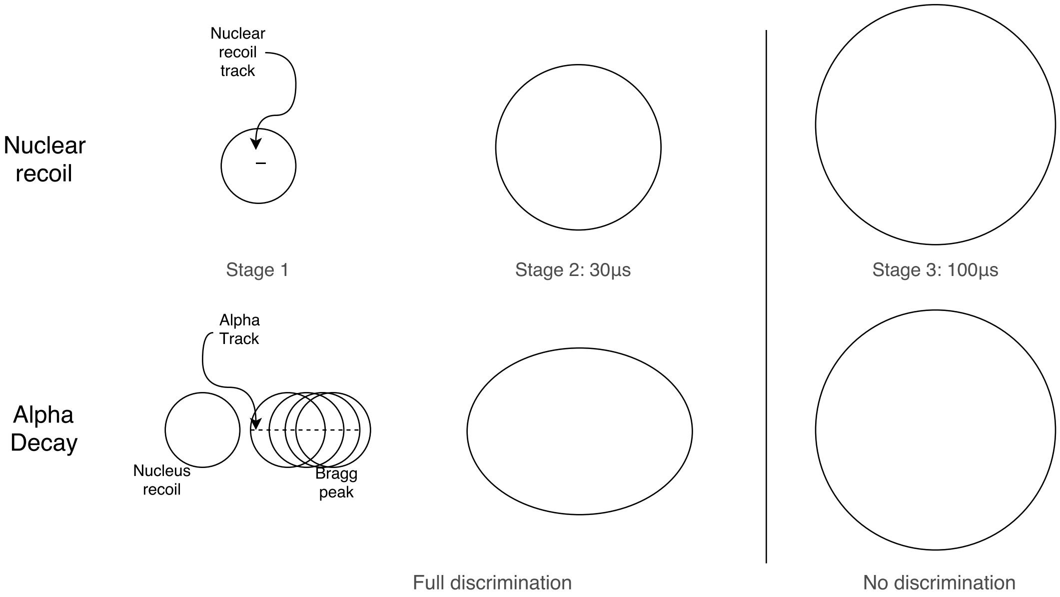

Figure 3.9: Time evolution of the growth of proto-bubbles created by an alpha particle interaction in comparison to one created by nuclear recoil. In an alpha event the track is longer yielding multiple proto-bubbles which merge on expansion. In a nuclear recoil event only a single proto-bubble is created. The absolute value of the acoustic energy yield in these two processes are not known.

3.6 Neutron Backgrounds

Background neutron events in a WIMP search detector resemble expected WIMP dark matter interactions and cannot be discriminated against acoustically. The strategy therefore is to reduce the number of neutrons present using shielding (as necessary) and to screen materials used in the construction of the detector to lower or eliminate the possibility of (α,n) reactions. Chapter 4 describes the shielding of PICO-60 from neutrons in the environment by placing it inside a water tank. The dominant neutron backgrounds are expected to arise from the detector construction materials via (α,n) and (γ,n) reactions where the primary source of the α particles are decays of naturally occurring ^{238}U and ^{232}Th. Careful consideration to select detector materials to reduce neutron flux is an ongoing effort. Simulations constructed from the known composition and geometry of detector materials give a model of the expected neutron flux in the detector. The background from neutrons in PICO-60 is predicted to be 0.32±0.12 singles and 1.19±0.41 multiples for the 3.3 keV Seitz threshold 30 live-day dark matter search run. The observed values were 0 single events and 3 multiple events. The prediction for the complete exposure is 3.64±1.27 multiple bubble events compared to the observed 5 multiple events. The experiment at this point is thus limited by neutron backgrounds [82].

3.7 Summary of this Section

PICO-60 delivers on a majority of the requirements for a dark matter search in an economical manner and is the leading spin-dependent direct detection experiment. PICO-60 is no longer in operation and has been decommissioned. The experiment was limited by neutron backgrounds primarily from (α,n) reactions in the materials around the detector and the expectation is that the experiment will incur 1 neutron for every 30 live days of running. The experiment has thus reached its sensitivity limit. Additionally the buffer liquid and C_3F_8 mixing are causing water droplets to be transported to, and deposited on, the wall of the inner vessel in the region where the active liquid resides. This kind of condensation is limiting the ability of the optics reconstruction algorithm and the ability to spatially resolve bubbles. PICO-40L will be the next experiment in the PICO family, addressing all these concerns. The pressure vessel in PICO-40L is wider, allowing for a larger separation between the inner vessel and the components responsible for the neutron background. PICO-40L is also a 'clean-sheet design' that uses a single active liquid in the detector.

Chapter 4

The PICO-60 Experiment

The first bubble chamber in the PICO family to use C_3F_8 as active liquid was PICO-2L [50]. The first run of PICO-2L had an unknown background that was thought to originate from particulate contamination. This background was also observed in the first PICO-60 run with CF_3I as an active liquid. An extensive campaign was undertaken to characterize and eliminate this contamination. PICO-2L was a test case for the removal of the particulate contamination. After the particulates were controlled, and the unknown background from PICO-2L was eliminated, the experiment produced a world-leading spin-dependent WIMP-proton limit. PICO-2L reached its sensitivity limit after 127 kg-days of WIMP exposure due to neutron backgrounds. Particulate contamination control was implemented in PICO-60 and is described in Chapter 5 of this thesis. The unknown background from PICO-60 was eliminated and this PICO-60 C_3F_8 Run 1 produced a world-leading spin-dependent WIMP-proton limit, improving on the result from PICO-2L.

4.1 Location

Reduction of background events is important for any dark matter search experiment. Alpha particles in the detector can be discriminated against using the acoustic signal from each event, but neutron backgrounds must be reduced as much as possible. There are several different sources of neutron backgrounds, such as cosmogenic spallation neutrons from the surroundings, (α,n) reactions in the detector material, and neutrons from the surroundings, such as the rock around the experiment.

The cosmogenic neutron flux originates from muon induced spallation in the surrounding material. Atmospheric muons are generated by the interaction of cosmic rays with the atmosphere. The neutrons generated in this manner can have a wide range of energies and are a significant background for WIMP searches. To shield the experiment from neutrons the rate of muons reaching the experiment must be reduced. This is done by placing the experiment deep underground where the overhead material absorbs a large fraction of muons. A graph of the muon flux as a function of depth is shown in Figure 4.1. The figure also shows the depths of different underground facilities around the world [83]. The PICO-60 experiment is located in the "Ladder Labs" area of SNOLAB, which is located 6800 feet below the ground at Vale's Creighton mine in Lively, Ontario, Canada. SNOLAB's overburden is 6010 meters water equivalent of rocks and the muon flux is 0.27 $\mu/\mathrm{m}^2/\mathrm{day}$. The thermal neutron flux is 4144.9 ± 49.8 ± 105.3 $\mathrm{n}/\mathrm{m}^2/\mathrm{day}$ and the fast neutron flux is approximately 4000 $\mathrm{n}/\mathrm{m}^2/\mathrm{day}$ [84]. The location and environment of SNOLAB is shown in Figure 4.2.

4.2 PICO-60 Hardware Overview

The PICO-60 detector is made up of a synthetic quartz inner vessel (IV), an outer stainless steel pressure vessel (OV) and a hydraulic system, along with a fluid fill system and DAQ electronics. A 3D expanded view of the CAD model of the inner vessel assembled in the outer vessel along with the detector components and the camera viewports is shown in Figure 4.3.

4.2.1 Inner Vessel

The IV is constructed from Heraeus HSQ-910 synthetic quartz glass. This is where the superheated active liquid, C_3F_8, resides. Bubble nucleations can be caused by nuclear recoil interactions, alpha decays, from nucleation sites along the wall of the jar, and very occasionally from electron recoils. These nucleation sites could be imperfections on the surface where gas microbubbles

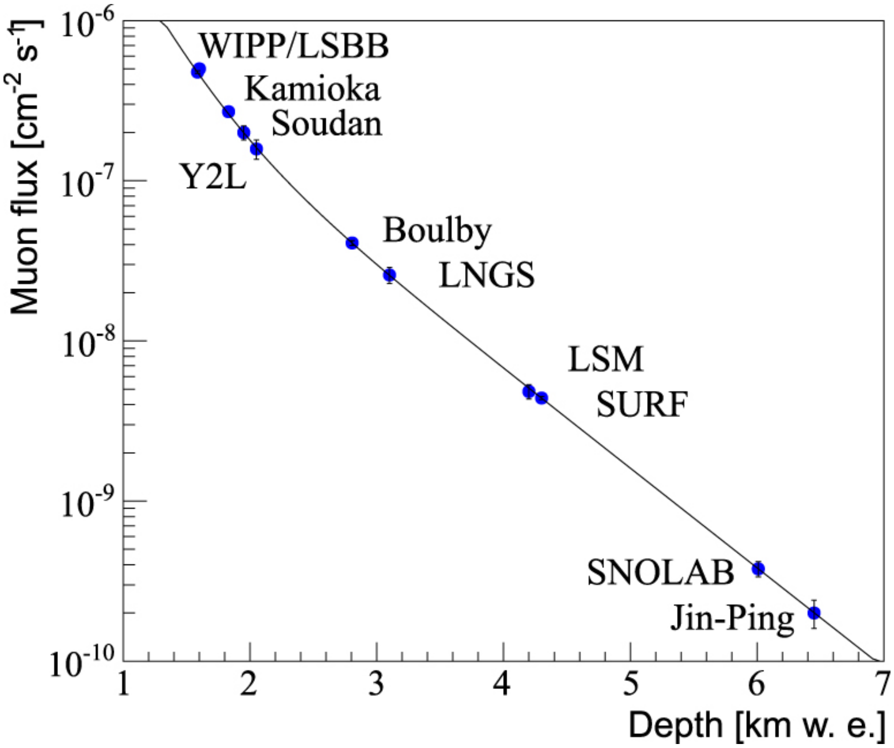

Figure 4.1: Muon flux as a function of depth for underground laboratories around the world. The theoretical prediction is the solid line. [83]

may be trapped, or they could be areas where an alpha particle is emitted. The quartz used to make the inner vessel had the lowest concentration of U and Th impurities out of all the materials in the synthetic quartz catalog of the three manufacturers (Heraeus, Momentive and Tosoh) that are able to produce such a vessel. There is no way to reduce the number of alpha decays arising from the detector vessel walls, so a fiducial cut was imposed to eliminate such events. Ideally, the number of alpha decays arising from the wall should be low so that the fiducial volume can be maximized and the time that the detector is not in an operational state (dead time) is reduced.

The IV, located inside a pressure vessel, is sealed with a gasket and a stainless steel-304 bellows assembly. There is a single inlet port attached to the bellows assembly through which a quartz stinger is inserted. This was designed to be used to sample the buffer liquid for particulate impurities.

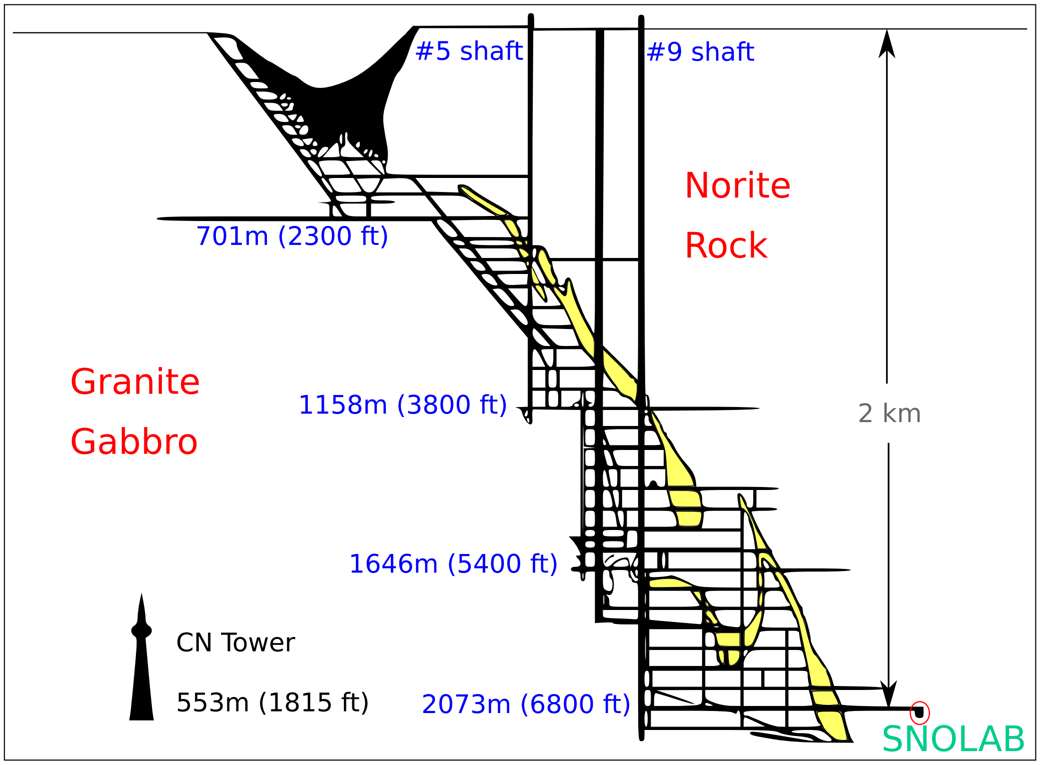

Figure 4.2: Location of SNOLAB in Creighton mine where the PICO-60 experiment is located [85]. Access to the lab is through shaft 9.

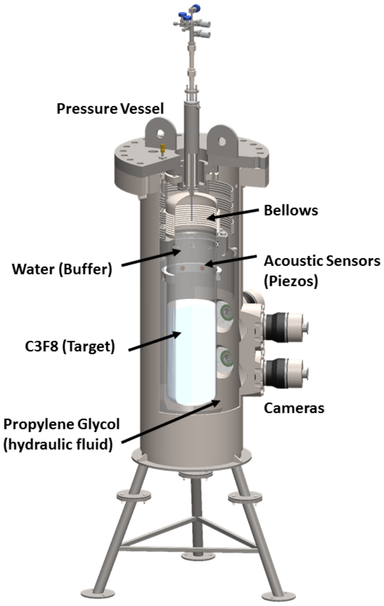

Figure 4.3: 3D CAD model of the PICO-60 detector mounted in the pressure vessel and configured for the C_3F_8 runs. Credit: M. Crisler

4.2.2 Outer Vessel

The outer vessel is filled with propylene glycol (Methyl Ethyl Glycol or MEG, with CAS number 57-55-6). Its primary purpose is to maintain the desired pressure for the operation of the detector and it is used as an optically transparent hydraulic fluid. A schematic of the compression system is shown in Figure 4.4. The operating pressure is between 21 and 30 psia when expanded, and 190 psia when compressed. The operating temperature is between 14 °C and 20 °C. The hydraulic control system manages the pressure of the hydraulic fluid in the pressure vessel. It consists of a piston that controls the pressure of the hydraulic fluid. This in turn allows for the pressure to be set inside the inner vessel, and sets the conditions of the superheat. A fast solenoid valve manages the expansion and compression of the chamber. In the event of a trigger the solenoid valve opens, allowing the piston to pressurize the detector into the safe compressed state.

The pressure vessel contains four glass window viewports for cameras and has a feed-through channel at the top for the connections to the piezo-electric sensors. The cameras are mounted at a stereo angle of 60 °. In order to minimize the amount of light needed to illuminate the chamber, and hence minimize the heat delivered by the LEDs, a retroreflector is mounted in the pressure vessel opposite the viewport windows. Four cameras were used to get a stereo view of the entire C_3F_8 target.

4.2.3 The Water Tank

In order to shield the experiment from environmental neutrons, mainly from radioactive decays in the rock and spallation neutrons from the material in the mine and the drift, the experiment is mounted inside a water tank. Water is mostly made of hydrogen atoms and is a low-Z moderating material for neutrons. The experiment's outer vessel sits on three legs inside the tank so that it is surrounded by at least a few feet of water on all sides. The water tank is lined with an HDPE liner and has a capacity of 20,000L. The tank is connected to a water purifier and a chiller system that controls the temperature

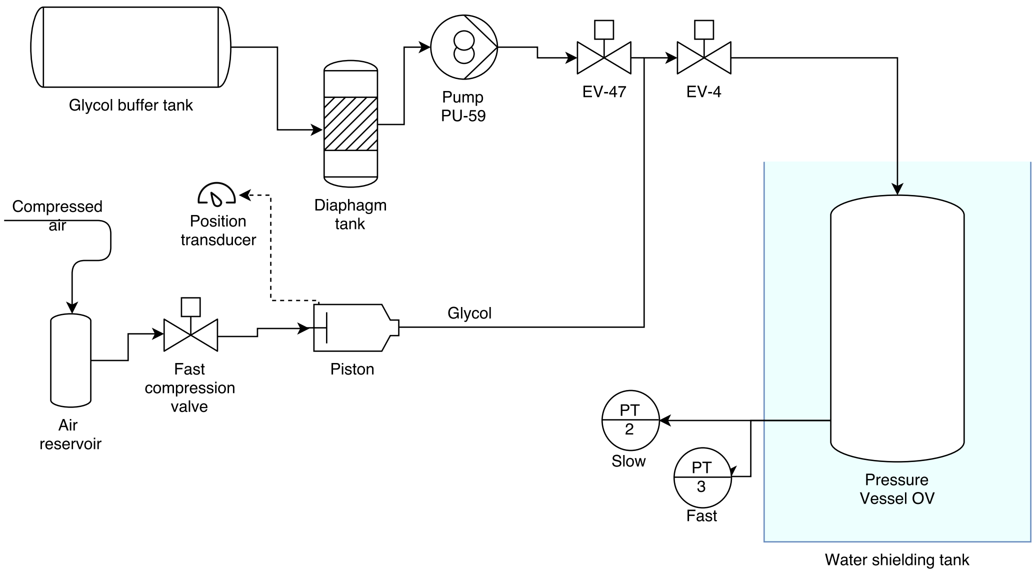

Figure 4.4: Schematics of the PICO-60 pressure handling system.

of the water in the tank. This is the only way to control the temperature of the bubble chamber. The temperature of the water is controlled with a LYTRON S-series RC-095 chiller system. There is also a water purification system to prevent bacterial growth in the tank. Figure 4.5 is an illustration of the chiller system that attaches to the water tank.

4.3 DAQ Hardware

PICO-60 data contains acoustic, video, pressure and temperature information. In addition to this information the ambient temperature in the lab is recorded at all times. The DAQ hardware is described in the next several sections and a diagram of the DAQ structure is shown in Figure 4.6.

4.3.1 Video

The four viewports on the pressure vessel are equipped with camera enclosures. The enclosures contain the cameras and the mounting hardware, as well as auxiliary components needed to operate them. The cameras are Basler ace acA2000-340km which can capture monochromatic images with a 2048×1088 pixel resolution at 340 frames per second. The cameras are connected to two

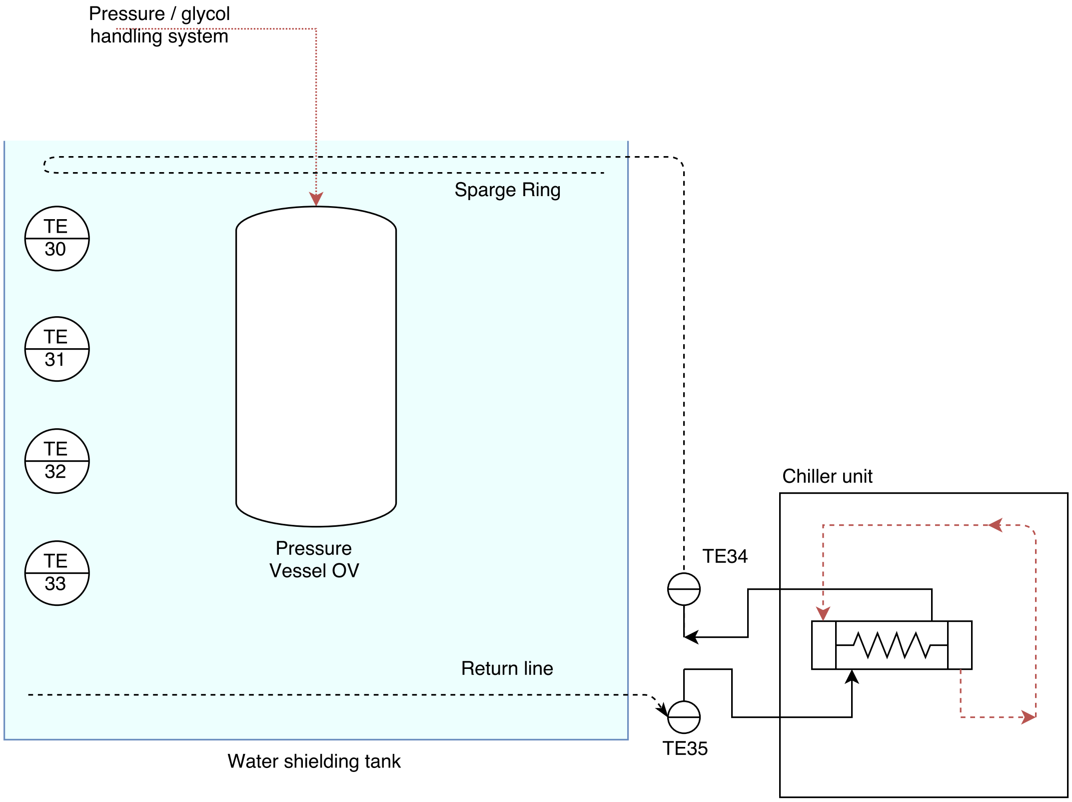

Figure 4.5: The water tank instrumentation and temperature control system

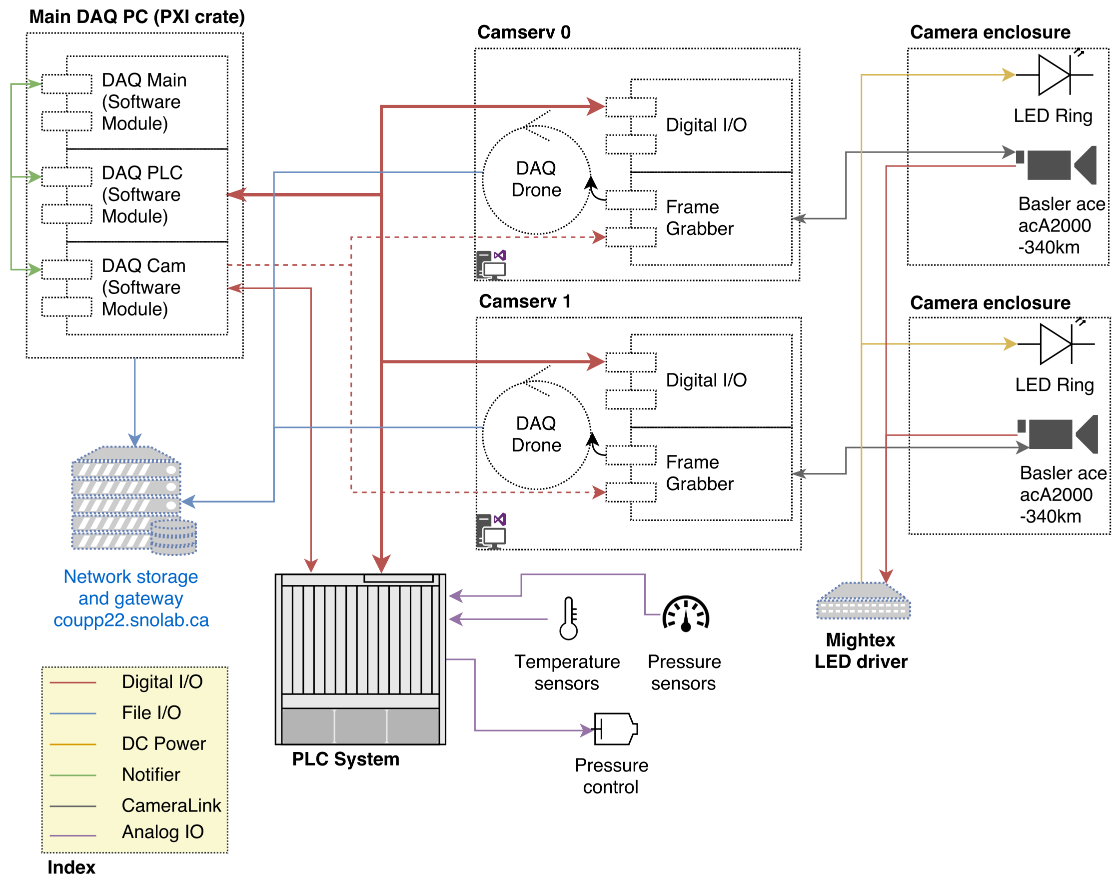

Figure 4.6: Schematic overview of the PICO-60 DAQ system. The main DAQ PC on the PXI crate runs the Main, PLC and Cam LabVIEW modules. The Cam module interacts with the dedicated servers that control the camera hardware and triggering. The PLC module interfaces with the Beckhoff PLC system.

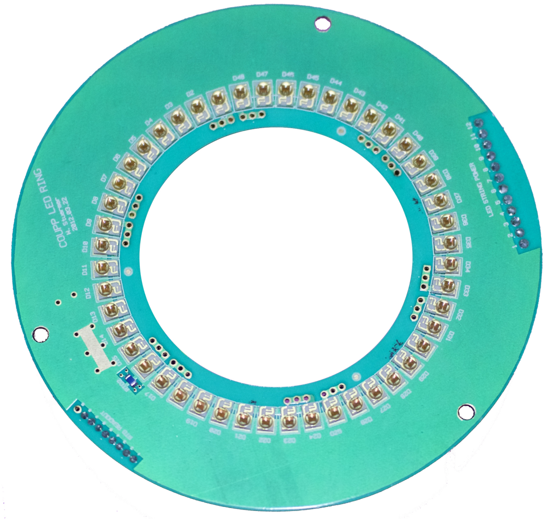

Figure 4.7: The LED ring.

Windows 8 servers via two dual link Camera Link cables. Each camera was placed on a hexapod: a mounting system that allows adjustments in the three spatial directions and three rotational axes. Each camera is surrounded by a ring with forty eight Luxeon LXM3-PD01 655nm red LEDs mounted on a PCB. The frame clocks of the cameras are connected to a Mightex LED control driver SLC-SA04-US. The LEDs light up only when the shutter of the cameras are open. This lowers the amount of heat transferred into the liquid to keep the temperature in the OV stable. The PCBs with the LEDs are mounted on a copper heatsink and forced air flow is used for cooling the LED rings.

4.3.2 Pressure

There are eight pressure transducers connected to the PICO-60. Their functions are summarized in Table 4.1.

PT-83 is used for monitoring the pressure inside the bubble chamber and for control purposes. PT-5 is the AC-coupled Dytran 2005V fast pressure transducer. It is connected to a Dytran 4112B current source. This sensor is sampled at 10 kHz to characterize pressure excursions during nucleation events, the data from which is used to determine the bubble multiplicity. This information is used for the WIMP search analysis, as described in Chapter 6.

Sensor Number	Contact fluid	Make and model	Function
PT-2	PG	Setra GCT-225	Slow response OV pressure
PT-3	PG	Noshock 100-500	Fast response OV pressure
PT-5	PG	Dytran 2005V	Very fast OV transient pressure measurement
PIT-7	A	Ashcroft 20X-1005HD-02L	Fast recompression air side pressure measurement
PT-14	A	Noshok 100-30A-2-1-2-1	Ambient pressure measurement
PT-41	PG	Noshok 100-500-2-1-2-1	Hydraulic pump pressure
PT-43	PG	Noshok 100-500-2-1-2-1	Hydraulic pump pressure
PT-83	WB	Noshok 612-300-2-1-T-20	Slow response IV pressure

Table 4.1: A list of the pressure transducers in PICO-60 that can be directly read by the PLC system. PG stands for propylene glycol / MEG and A stands for air and WB the water buffer liquid in direct contact with the C_3F_8.

4.3.3 Temperature

PICO-60 uses resistance temperature devices or RTDs (Omega HSRTD-3-100-A-240-E) to measure the temperature in the water shielding tank and inside the pressure vessel. Temperature sensors TE30-33 (Minco S101733PD3S80 connected to Minco TT176-PD1N RTD transmitters) measure the temperature of the water tank. TE91-98 measure the temperature of the MEG inside the pressure vessel. The temperature of the detector is controlled by the water in the tank as described in Section 4.2.3. Since the pressure vessel is made of steel, which is thermally conductive, the OV should be in equilibrium with the temperature of the water in the tank. Every temperature change is performed slowly over 24 hours for every 1 °C change. This allows time for the contents of the inner vessel to come to equilibrium with the MEG in the outer vessel, which in turn is in equilibrium with the water in the tank. There is no way to directly measure the temperature of the active liquid inside the IV.

4.3.4 Position Measurements

There are two position measurement devices in PICO-60. ZT-4 (Unimeasure JX-PA-3.8-N11-21S-N31) measures the position of the bellows and their expansion. ZT-6 (Balluf BTL5-E10-M0203-Z-S3L) measures the piston position (Figure 4.4) in the compression system.

4.3.5 Piezo-electric Acoustic Sensors

The expansion of a nucleation bubble in the superheated liquid generates acoustic signals, as described in Section 3.4. The signals are used to gain information about the nature of the particle interaction that caused the nucleation, the analysis of which is described in detail in Section 6.4. To record the acoustic information, eight lead zirconate titanate (PZT) piezo-electric transducers were constructed by PICO collaborators at Indiana University South Bend. These eight sensors were fitted to a ring mounted near the top of the IV. The idea was that the tension provided by the ring will be sufficient for a good coupling between the IV and the sensors, however in practise the tension was not enough to provide a good coupling leading to a low quality of signal from the piezo-electric sensors. Each sensor housing contains the piezoelectric crystal along with a pre-amplifier. Five of the sensors failed before the first dark matter search run (October 2016 to January 2017), and only the remaining three were used for the analysis presented here. One more sensor failed after the first dark matter search run was over. The second set of dark matter search data, taken after January 2017, therefore relied on only the two remaining piezo-electric crystals.

4.4 DAQ Rack and the PLC Crate

All of the control hardware components connect to a Beckhoff bus terminal attached to a Beckhoff BX9000 PLC controller. The controller is connected and operated by the MODBUS over ethernet program GE/Proficy iFix. A dedicated computer is used for this system. The PLC controller also connects to the National Instruments PXIe crate machine (NI PXI-1044 chassis with a computing unit NI-PXI-8104) where the master LabVIEW control module records data from the PLC instrumentation and can issue commands to pressurize the detector when an event is reported by the imaging subsystem or the PLC triggers. The piezo-electric sensors were connected to two NI PXI-6133 fast digitizer cards on the PXI crate, which are read by the FastDAQ module running on this computer.

4.5 PICO-60 Video Trigger

When expanded, the bubble chamber is continuously monitored by the cameras. The triggering algorithm is run on two computers that each host two cameras. The camera resolution necessitates a data transfer rate of 5 Gbps from each camera at 340fps. Checks for the presence of a bubble are performed on every alternate frame before January 2016 and every fourth frame from February 2016, requiring a minimum data processing speed of 2 Gbps × 2. A trigger decision is based on the image entropy S_I [86] of the absolute difference of the current frame and the preceding frame, where

$$S_I = -\sum_{i=1}^{16} P_i \log_2 P_i. \tag{4.1}$$

An image histogram is constructed from this difference of frames, with 16 intensity bins over the full 8-bit dynamic range of each pixel from 0 to 255. The values P_i are the probabilities for the intensity of any pixel in the difference image to fall into the i^{th} intensity bin, so the histogram is normalized by the number of entries. The quantity S_I for this difference of images is then calculated by the sum over the 16 normalized bins of the image histogram. The entropy is sensitive to changes in information content of an image and is expected to change if new information is present in an image but is relatively insensitive to minor motion of objects in the frame and pixel noise.

Each camera has a threshold in S_I determined using test images of bubbles. The values of the entropy threshold were originally chosen to be ten standard deviations away from the mean of S_I. The final values of the trigger were

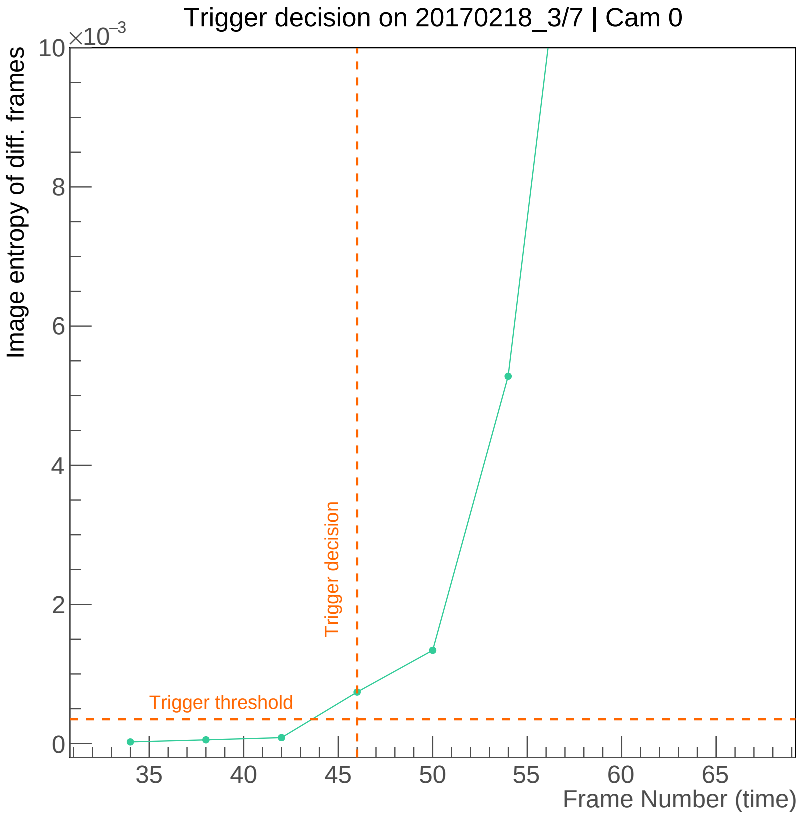

Figure 4.8: Image Entropy of the frames during a single bubble event. The trigger threshold and the frame in which the algorithm issued a trigger decision are also shown. The vertices represent frames in which the trigger condition is evaluated.

empirically chosen by lowering them as much as possible while keeping the threshold just high enough to avoid triggering on pixel noise. The time evolution of entropy for a single bubble event is shown in Figure 4.8. The frame where the algorithm issued the trigger is marked in the figure. The values of the entropy thresholds on all four cameras are given in Table 4.2.

The camera servers compute the image entropy and issue a trigger signal as soon as the entropy threshold is exceeded on any of the cameras. The master DAQ system then receives this trigger and broadcasts a master trigger across the system that fires the piston to compress the bubble chamber and records the data associated with the event.

The detector takes ∼5 seconds to expand and reach the set pressure. Dur-

Camera	Threshold	σ from noise
0	0.00035	3.3
1	0.0003	2.3
2	0.0003	2.5
3	0.0003	3.0

Table 4.2: Image entropy threshold of all four cameras.

ing a part of this time the active liquid is superheated, albeit at a lower threshold, so there is a possibility of a bubble nucleation during expansion. Data generated during the first ≈ 5.25 seconds of an expansion were typically ignored by the main DAQ controller to allow the pressure to stabilize, but the video triggering mechanism must be active during this time to capture any nucleation bubble so that the detector is not left in a superheated state without a fast triggering mechanism at any time. The inner vessel assembly can move significantly during expansion and cause video triggers without any nucleation. To keep the video trigger active during expansion, sections of the image with moving parts are masked off and excluded from the image entropy calculation. These masks are used at all times since the software running the video triggering algorithm (DAQDrone) does not receive pressure information and therefore does not "know" when to expect movements in the detector.

The above poses the dilemma that bubbles created in the "masked" regions of the image that are during normal operation might be missed or captured late. Using test data (imaging data from bubble nucleation stored for the purposes of testing video related algorithms) two histograms of the frame of trigger were made - one using no mask and the other with the mask applied, to quantify the amount of delay incurred by the mask. These histograms are shown in Figure 4.9. It can be seen that the average delay in the video trigger caused by the mask is about half a frame ($\sim$1.5ms). This is an acceptable solution, since the delay is less than the time between trigger checks, and it was implemented after the movement of the vessel was first observed during commissioning. There were 9 triggers out of $\sim$900 tested that were issued late by 20 frames. This is not a problem since the image analysis algorithm AutoBub (Chapter 6) separately calculates the frame where the bubble can be first seen without a mask applied. Additionally, the delay described is for one camera only, and when the signal from all four cameras are taken into account, the number of late triggers is <0.05%, as shown in the next section under "missed triggers".

During the first dark matter search run and the pre-physics run, the cameras acquired images at 200 frames/second, and checks for the presence of a bubble (video trigger) were performed on every alternate frame. Between January 23-25, 2017 upgrades were performed to the DAQ system and the speed of the image acquisition was increased to 340 frames/second with a check for the presence of a bubble performed on every fourth frame. The maximum delay introduced by the interleaved trigger checking is 10 ms for the 200 fps data and 11.6 ms for the 340 fps data.

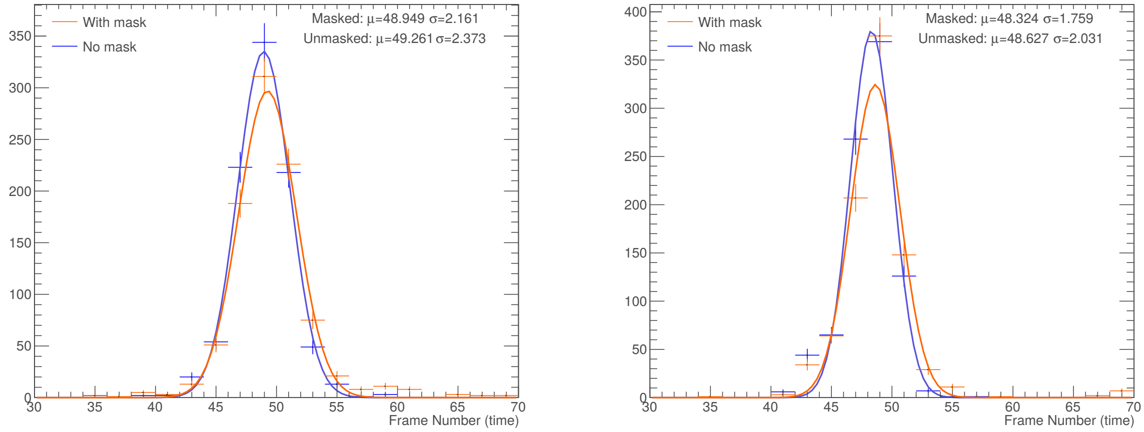

Figure 4.9: Detection frame for bulk (right) and wall (left) events, demonstrating the consistency of the trigger before and after application of image masks.

4.5.1 Trigger Performance Metrics

The trigger was benchmarked for performance after development. The key metrics and their results are:

- **Missed triggers:** The number of missed triggers can be studied by selecting events in the PICO-60 dataset with a pressure trigger (a trigger issued by a rapid rise in pressure with no bubble registered by the imaging subsystem). There were 17 such triggers out of around 30,854 total. The new trigger logic was designed to be tolerant to faults and the efficiency of the algorithm is 100%.

- **False triggers:** This is the number of video triggers issued without the presence of a bubble. These events can be selected by correlating the lack of a fast pressure (dytran) excursion with the video trigger. There were 3 such triggers out of around 30,854 total. Again the robustness of the algorithm is demonstrated in this case.
- **Frame skips:** The trigger algorithm and its implementation were engineered to avoid frame skips completely. Nevertheless frameskips do happen, but as demonstrated by the rate of missed triggers the frameskips have minimal impact.

4.6 Bubble Chamber Operations

The PICO detector works on the principle of a bubble chamber that stays expanded until a nucleation is detected. The expanded pressure set point was kept at 30 psi during the first phase of the dark matter search run and 21 psi in the second phase. The temperature was adjusted to set the desired threshold. When an expansion of the chamber begins, the hydraulic system lowers the pressure until the target pressure (30 psi or 21 psi) is reached. The active liquid becomes superheated in the process. The chamber stays in this state until a trigger condition is detected or a timeout occurs after 2000 s triggering a compression. When an event is triggered, the hydraulic system compresses by increasing the pressure to 190 psi. The chamber then stays compressed for 180 seconds until the next expansion. After 10 expansions the chamber is compressed for 600 seconds. Additionally, if a trigger was missed by the cameras and a compression was triggered by rising pressures (a pressure trigger), the chamber stays compressed for 600 seconds. These long compressions were found to increase detector stability. A graph of pressure

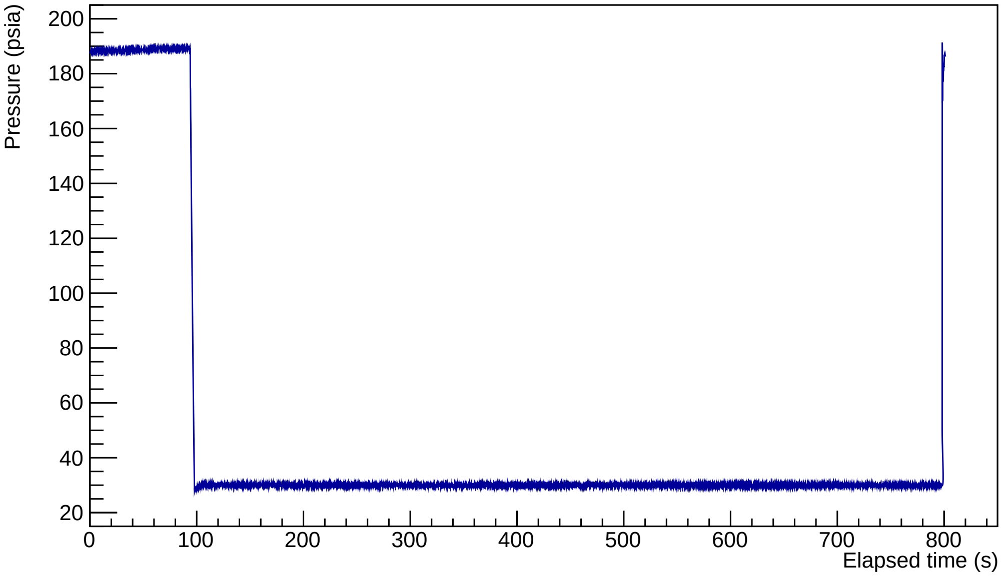

Figure 4.10: Pressure cycle during an expansion of the chamber taken from run 20170420_0 event 1. The pressurized state is at 190 psi. On expansion the pressure drops to the operating condition at 30 psi. An event is triggered at around 800 seconds and the chamber compresses back to 190 psi.

versus time for a typical expansion is shown in Figure 4.10, outlining each phase of the expansion cycle.

4.6.1 Dark Matter Search: Blind Operations

In order to eliminate bias in the analysis it is necessary that the dark matter search data be “blind” which means that the collaboration decided to not process this data until all aspects of the analysis were finalized and formally approved. All cuts should ideally be set on calibration and background runs. In PICO-60, the bubble chamber needs to be monitored for stability, so the part of the dark matter dataset that is required for operations and maintenance is open for analysis. This includes the pressure, temperature and video data. The acoustic data that allows for the discrimination between alpha events and nuclear recoils is collected but not processed and so is unavailable for analysis until all the cuts are finalized. A “blind” dark matter search in the context of

PICO thus means that the acoustic information is not available. After cuts are finalized and the analysis is frozen, a re-processing of the data is performed and the results from the analysis of the dataset are announced to the collaboration.

4.7 The Data Set

The second PICO-60 run was filled with 51.96±0.14 kg of C_3F_8 in June 28-30, 2016. Between September and November, numerous "engineering runs" were performed to understand the behaviour of the detector and perform necessary upgrades and changes for stable operation. During these runs, and before the blinded physics run, 20 live days of data were collected. These data consisted of background and calibration runs with gamma and neutron sources. The first blinded physics run was conducted from November 28, 2016 to January 13, 2017. The camera frame rate was increased on January 23rd. After the first blind background run at 3.3 keV, the pressure was lowered and the water tank temperature was increased in order to raise the C_3F_8 temperature from 14 °C to 16 °C. At these run conditions the Seitz threshold was (1.81 ± 0.05) keV and the behaviour of the detector was probed at this threshold. An increased bulk event rate was observed with similar acoustic response as nuclear recoils, indicating gamma nucleation. Extended neutron and gamma calibrations with ^{252}Cf and ^{60}Co sources were performed. In order to conduct a second blind run the pressure set point was raised to 30 psi for a Seitz threshold of (2.45 ± 0.05) keV. A set of calibration runs and a blinded WIMP search were then performed. The Seitz threshold was set to (3.29 ± 0.05) keV for the first blinded run, (2.45 ± 0.05) keV for the second blinded run and (1.81 ± 0.05) keV for the period in between where the background data set was not blinded. A summary of all the data collected between WIMP search runs and background runs is shown in Table 4.3.

Run name	T (°C)	P (psia)	Seitz E_T (keV)	Livetime (d)	WIMP exposure (kg-d)	Candidates
BGU18	15.9	21.7	1.81	7.04	310.81	13
BGB24	15.9	30.5	2.45	29.95	1404.22	3
BGB33	13.9	30.2	3.29	29.96	1322.37 [re-analysis]	0
oBGB33	13.9	30.2	3.29	29.96	1167 [published]	0

Table 4.3: The sets of operating conditions and their associated exposures for WIMP search data collected with PICO-60. The experimental uncertainty on the threshold is 0.05 keV and comes from uncertainties on the temperature (0.1 °C) and pressure (0.3 psi). The run type BGU stands for unblind background and BGB for blind background (dark matter search).

Chapter 5

Particulate contamination and cleaning

5.1 Introduction

An anomalous source of nucleations was observed in the PICO-60 CF_3I, COUPP4 and run 1 of PICO-2L [50]. These anomalous events are not from WIMP interactions (details are presented in Section 5.2) but they closely mimic nuclear recoils in their acoustic properties and thus resemble a WIMP signal. The anomalous background limited the dark matter sensitivity as a large fraction of the exposure was contaminated by the background and had to be removed.

To operate PICO-60 with C_3F_8 and free from anomalous backgrounds, it was essential to study and understand the source and then eliminate it. Based on observations of the location, the timing, and the relationship between the rate and the time that the detector stays in an expanded state (expansion time) of these events, the hypothesis that this background was caused by residual particulates in the active liquid was developed. These particulates are theorized to be small enough in size to remain suspended in the liquid or are attached to the water droplets to form neutrally buoyent objects. A procedure for the collection of samples from PICO chambers was developed, and the samples were analysed with a scanning electron microscope, ToF-SIMS (Time of flight secondary ion mass spectrometry [87]), Optical microscopes, and ICP-MS (Inductively coupled plasma mass spectrometry [88]). The conclusions from the study were then used to design and implement a cleaning procedure that was used for run 2 of PICO-60.

5.2 Evidence guiding the hypothesis

Since the anomalous source of nucleation produces events that are acoustically similar to nuclear recoils, it needed to be determined that this is not a dark matter signal. It was observed that the rate of anomalous events exhibited very strong expansion time correlations and the anomalous events preferentially occurred right after an expansion. A WIMP signal is expected to be flat in time since it would have no causal connection to the elapsed time since expansion. In addition to the time correlations, the event rate was higher near the walls of the detector and near the active liquid-buffer liquid interface (called the “surface”). Thus these events could not come from dark matter interactions and are dubbed “anomalous".

To answer the question of the origin of the anomalous events, their observed properties were studied. The observations may be summarized as:

- The events are located closer to the wall of the jar and the active liquid-buffer liquid interface.
- The anomalous events are at a higher position in the jar during episodes of falling temperature and at a lower position in the jar during episodes of rising temperature in the detector.
- The surface activity was higher at lower expansion times and was higher near the walls than the centre.
- There were some periods of time where a lot of nucleations were observed at the bottom of the jar and the apparent nucleation source moved up the hemisphere wall. Most of the events are concentrated near the surface and the bottom with a thin region near the walls.
- The anomalous rate was enhanced at lower thresholds.

5.3 Sampling the inner vessel of PICO-60 and PICO-2L for particulates

To sample the vessel the CF_3I was first evaporated into storage containers. The assumption was that the contaminants are less volatile than CF_3I and remain in the detector after the evaporation. Then, the residual water associated with the buffer liquid was sampled through a long stinger tube and passed through a 200 nm teflon filter (Advantec H020A025A PTFE Hydrophilic Membranes - 25 mm diameter and 0.20 µm pore size [89]). The liquid was collected in a liquid trap which was attached to a pump for vacuum suction. Blank filters were taken and were handled in the same way to serve as “process blanks" that capture the contaminants introduced while handling the filters.

A recirculation system was created to clean and sample PICO-60. It was used to spray a high pressure jet of water on the inner walls of the detector vessel and sample the liquid by passing the return water flow through a set of filters. A soap, CitroJet, was applied at 2% concentration by volume. The filters were then analysed at the University of Alberta and at the Pacific Northwest National Laboratory. For PICO-2L, a liquid trap was made to collect the residual water after Run-1 and Run-2. The particulates were studied under various microscopes while the liquid was analysed using ICP-MS. A small sample of particulates were also analysed using ICP-MS in hydrofluoric and nitric acid (DocDB 1464).

The first sample of particulates from a wash cycle of PICO-60 was lost because of a misunderstanding between personnel working underground on that day. In the first attempt to sample particulates from the PICO-60 IV an in-line filter was attached to the recirculation system, thus trapping PICO-60 particulates without them being sampled correctly. The best estimates of the particulate load in the PICO-60 CF_3I run was reconstructed by making a figure of the amount of material recovered in each subsequent sampling and then using an exponential fit to extrapolate the original quantity of material. The graph is shown in Figure 5.1. The extrapolated quantity of material contained was 235 pg of thorium (0.47 α/day) and 92 pg of uranium (0.74

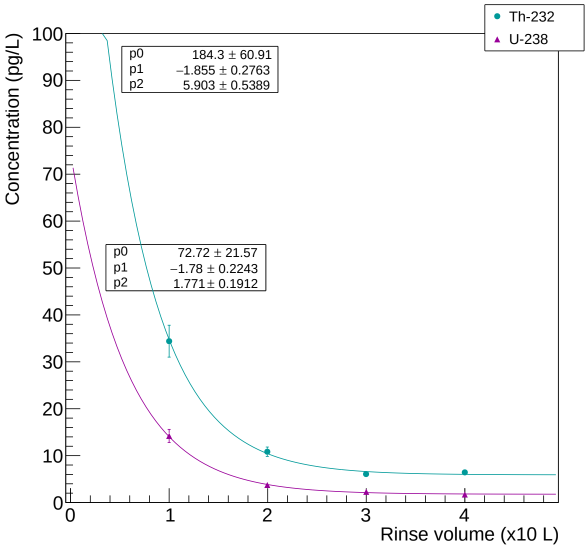

Figure 5.1: Concentrations of U and Th recovered in the sampling of PICO-60. For each rinse, ten litres of water was used. One litre water was sampled through an Advantec H020A025A PTFE filter. The ICP-MS results of the U-238 and Th-232 in this sample is presented. An exponential fit was used to estimate the original quantity of material.

α/day). Since 1 L water was sampled out of 10 L, the expected rate of α particles would be 4.7 α/day from ^{232}Th and 7.4 α/day from ^{238}U. This is the same order of magnitude of background events observed, including the anomalous events. The errors on these measurements are large since samples were lost and the mechanism of transport of radon is unknown, so the estimate of the contribution of particulates and radon to the anomalous background has a large uncertainty.

5.4 Optical microscopy

An optical image of a filter recovered from the PICO-60 CF_3I IV sampling is shown in Figure 5.2. The filters were imaged under a Keyance VHX 2000 scope at a magnification of x200. The image shows the presence of particulates that are brown in colour that were demonstrated to be consistent with rust (next section). In addition, there are hazy patches, that are too small to resolve with an optical microscope. While distinct particulates could be seen in many

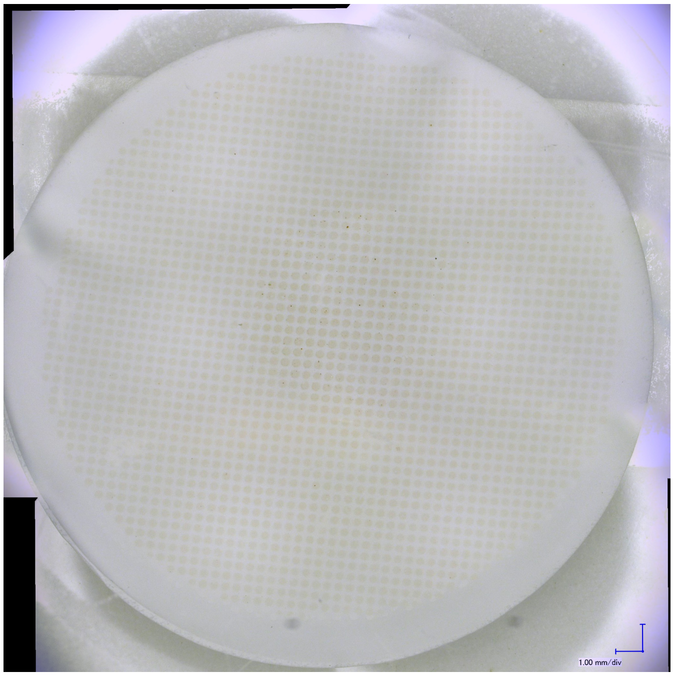

Figure 5.2: Optical image of the 3.5mm filter sample after collection of particulates from PICO-60. The pattern of dots is created because the liquid being sampled flows through a screen with that pattern before entering the filter.

places a large fraction of the filter had a brownish appearance indicating that the particulate material was small and diffuse. Optical microscopy was not able to resolve the contaminants and electron microscopy was used instead to characterize the particulates.

5.5 Electron microscopy

Scanning Electron Microscopy (SEM) along with Energy Dissipative X-Ray Spectroscopy (EDS) were performed on the filter samples collected from PICO-60 using a JEOL JSM7600F (at PNNL) and a Tescan Vega3 SBU, a Zeiss EVO and a Zeiss Sigma FESEM (at the University of Alberta). All four instruments were equipped with Oxford Instruments INCA silicon drift detectors for EDS. The samples were studied at various accelerating voltages from 5 kV to 20 kV to reveal their morphology and composition.

SEM pictures of a few typical and atypical particulates observed are presented in Figure 5.3. Amongst the list of particulates found were flakes of gold,

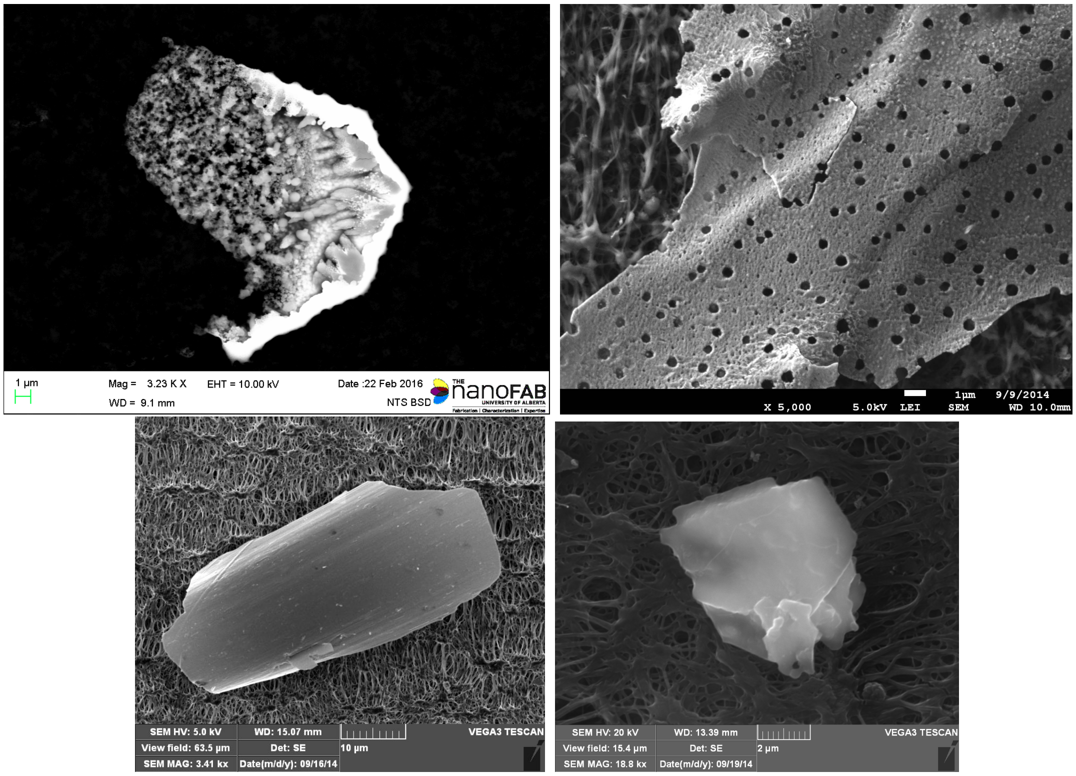

Figure 5.3: Electron images of the particulates found in the PICO detectors. Top: oxides of iron (possibly steel) and bottom: of gold (left) and quartz (right).

silica (glass or quartz) and steel. EDS was used to produce spectra of many particulates that were observed on the filters. One such spectrum is shown in Figure 5.4.

To infer if there are different types of steel, an analysis of the ratios of different components of the steel by mass was performed (see Figure 5.5, showing the analysis of a PICO-2L sample). In this figure, the ratio of Fe to Cr is shown on the x-axis and the ratio of Fe to Ni is shown in the y-axis. Different grades of steel will form different “clusters" in this figure due to their compositions. Alloys such as Inconel/Hastelloy (used in the C-ring seal between the glass inner vessel and bellows of PICO-2L vessels) appear separated from stainless steel based compounds. Stainless Steel (SS) - 316 and SS-304 lie in the same cluster in this figure, but SS-316 contains Mo whereas SS-304 does not. Therefore, this information can be used to separate the SS-316 components and they have been coloured red.

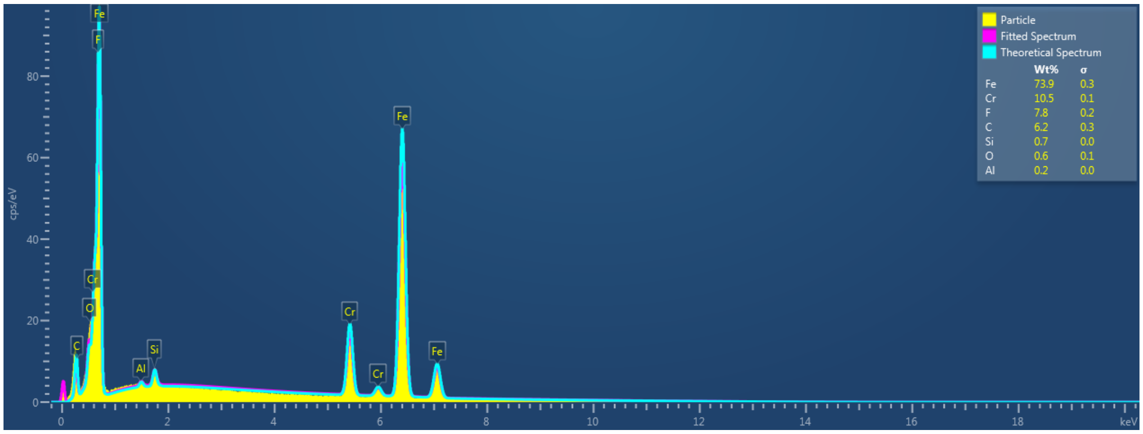

Figure 5.4: EDS spectrum and mass ratio estimates of a steel particulate. The X axis shows the energy of the X-rays and the Y-axis shows the counts.

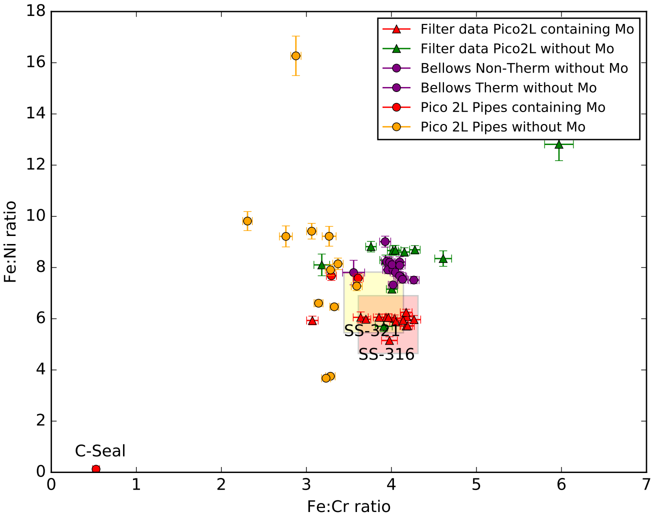

Figure 5.5: The ratio of the constituent elements by mass in each steel sample measured.

The EDS spectrometer can be used to make maps of the different kinds of elements present in the particulates under study. One such map is shown in Figure 5.6. Image analysis was performed on the maps and the particulates were fitted to contours. The magnification value of every image can then be used to construct a distribution of the sizes of the particulates. A particulate size distribution of Fe in the filter collected by sampling the buffer liquid after the PICO-60 CF_3I run is shown in Figure 5.7. This figure can be repeated for specific kinds of particulates such as steel (using iron, manganese and chromium) or for quartz (using silicon and oxygen). Since an SEM image is two dimensional, information about the height of a particulate cannot be obtained. A rough estimate of the amount of materials in the detector was made by approximating that each piece of particulate is an ellipsoid. This approximation can be used to aid in the estimation of backgrounds and in finding the origins of the particulates.

From Figure 5.6 and from the presence of Molybdenum it was evident that SS-304 and SS-316 were both present. The source of SS-304 was identified to be the bellows system since it is the only component made out of this alloy. SS-316 was used in all the plumbing and tubing providing multiple possible sources. The gold observed under the electron microscope would originate from the gold ring seal between the IV and the bellows.

5.6 Particulate mass and radioactivity

It was estimated that the extracted silica content in PICO-2L was $(8.8 \pm 3.6)\,\mu\mathrm{g}$ and the total steel content was $(0.15 \pm 0.01)\,\mathrm{mg}$. For PICO-60, the estimate was $(7.12 \pm 2.90)\,\mu\mathrm{g}$ of silica and $(0.24 \pm 0.02)\,\mathrm{mg}$ steel, based on the extrapolation from the steel content on a single filter.

Another estimate of the quartz content in PICO-60 is available using a profilometer at the Pacific Northwest National Laboratory (PNNL). The source of the quartz in PICO-60 was identified to be the gold o-ring seal of the vessel applying too much compressive force on the quartz and thus forming a ridge. An image of this analysis is included in Figure 5.8. The results from this

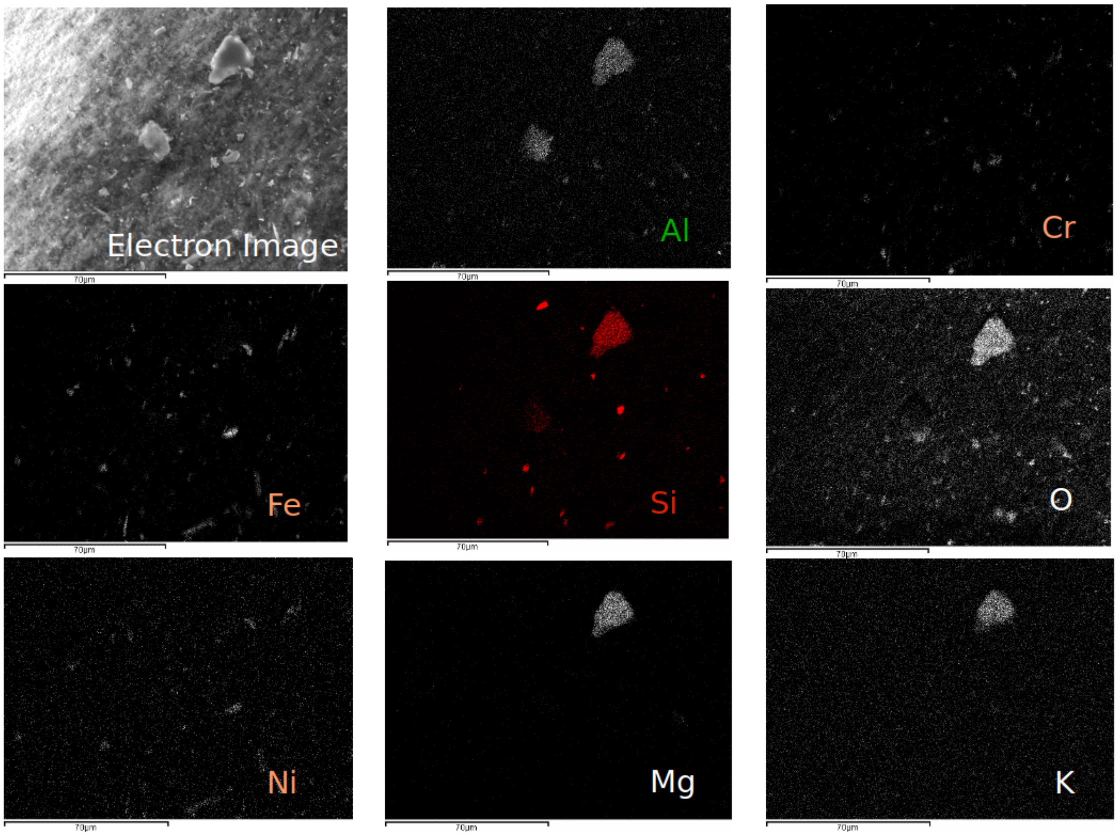

Figure 5.6: EDS maps of different elements in the particulates collected in one small area of one filter.

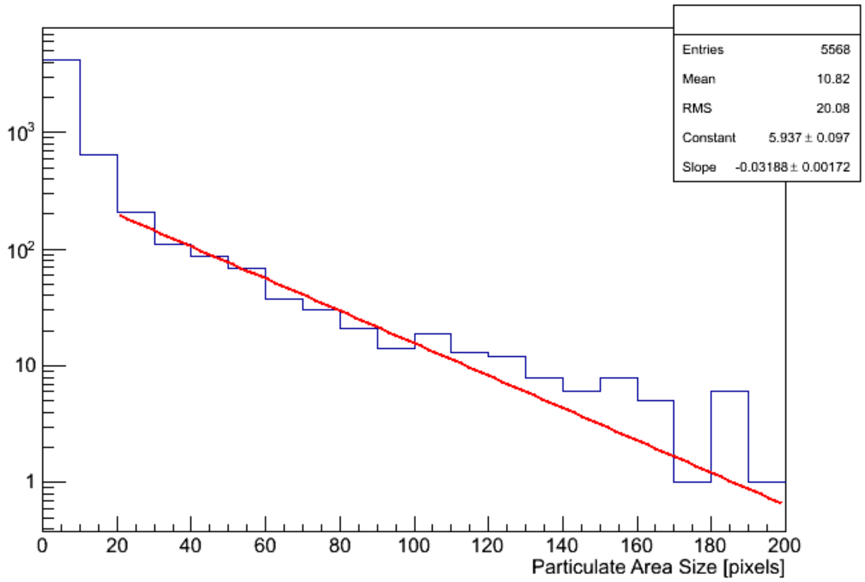

Figure 5.7: Distribution of all steel particulate sizes as seen under the SEM in the filter collected by sampling the buffer liquid after the PICO-60 CF_3I run. Five randomly chosen sites were sampled to create this histogram. Note that the scale on the SEM was 3.428 pixel/μm

experiment put an upper limit of quartz content at 270 µg.

5.7 ICP-MS Measurements

The IV buffer fluid from PICO-2L and PICO-60 CF3I runs was analyzed at an ICP-MS facility to determine the amount of U and Th chain impurities. In addition, some particulate samples were dissolved in hydrofluoric and nitric acid and then processed. The results are summarized in Table 5.1 and 5.2.

An anomalous rate of 25 events/day was observed in PICO-60. The alpha particle rate was 15 events/day, the surface rate was 12/day and the wall+collar (the interface between the CF_3I and the liquid that touches the wall of the vessel, forming a meniscus) rate was 31 counts/day. The volume fraction of water volume-to-CF_3I in the detector was 85%:15%. Assuming that the particulates were evenly distributed in the water and CF_3I, the amount of radioactivity in the buffer fluid and the particulates is not sufficient to explain the anomalous background. Therefore its origin is unlikely to be radioactive

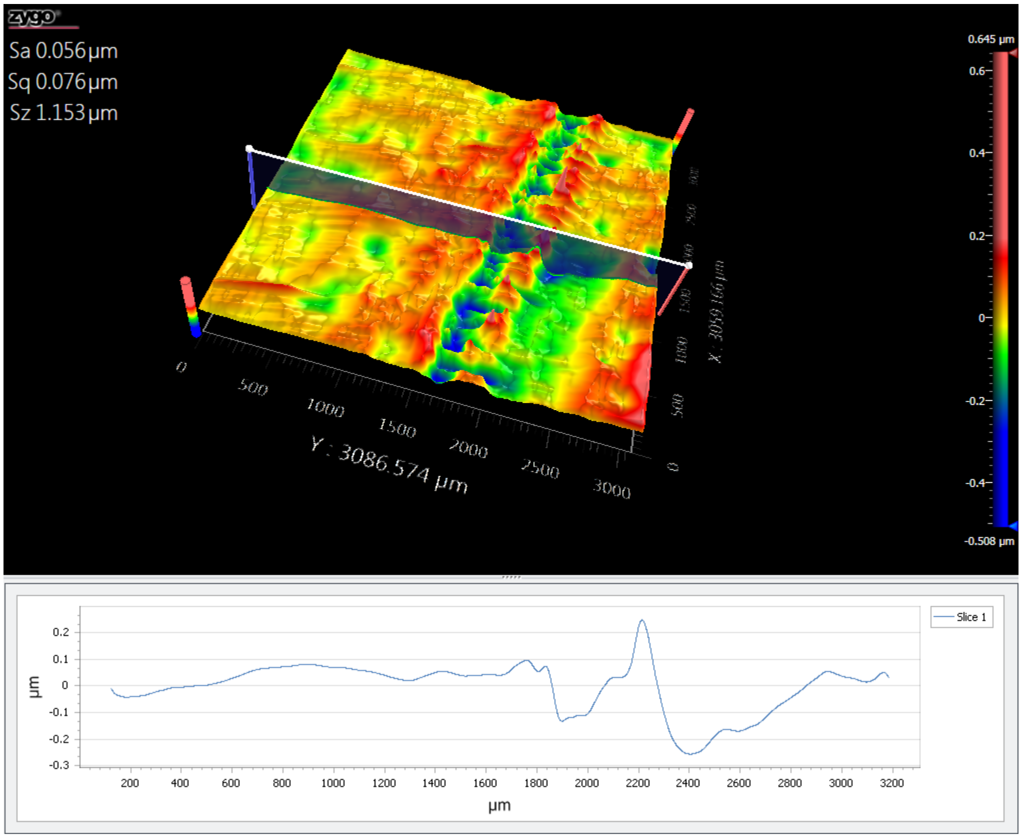

Figure 5.8: The quartz flange of the first PICO-60 vessel was examined with a Zygo NewView 8300 optical surface profilometer. A ridge was discovered in the location of the gold o-ring seal, indicating that stress on the quartz surface due to the o-ring caused the glass to erode in the region of contact. The profile of the ridge on the quartz flange is shown in this image. It is believed that some of the material from this ridge was the source of the silica/quartz particulates in PICO-60. Credit: I. Arnquist.

Sample	U mass [pg]	U equ. rate [cpd]	Th mass [pg]	Th equ. rate [cpd]	Comments
Sample 2014-1 (elog 4742), 2 L sample, 30 minutes with radiacwash. Sample was collected on 0.5 µm PTFE filter	0.62 ± 0.03	0.005	0.48 ± 0.03	0.001	← this is where the water samples were taken
Sample 2014-2 (elog 4743), 20 L sample, radiacwash overnight. Sample was collected on 0.5 µm PTFE filter	1.05 ± 0.05	0.009	7.54 ± 0.07	0.015	

Table 5.1: ICPMS results: PICO-60 CF_3I run: particulates.

Sample	U mass [fg/g]	U equ. rate [cpd]	Th mass [fg/g]	Th equ. rate [cpd]	Comments
Sample 2014-3: Water through 500 nm PTFE, collected in 2 L flask. Label 3 of 4 and elog 4741	47.69	32.82	762.66	27.97	← in 80 L of water
Sample 2014-4: Water through 500 nm PTFE, collected on day 2 with radiacwash overnight Label 4 of 4 and elog 4741	304.51	209.58	1010	169.48	← in 80 L of water

Table 5.2: ICPMS results: PICO-60 CF_3I run: buffer water

in nature but rather physical or thermodynamical.

5.8 PICO 2L Run-2

To test the hypothesis that particulates were one reason for the anomalous nucleations, PICO-2L run-2 was prepared with several changes. The quartz vessel was changed and a strict cleanliness protocol was implemented for the

	Exposure (kg-days)	Alphas	Candidates	Multiples
Run-1	74.8	179	9	0
Run-2	127.0	347	1	3

Table 5.3: Comparison of background rates before and after particulate elimination in PICO-2L

assembly of the device. The bubble chamber was assembled and cleaned at Fermilab and shipped filled with water to SNOLAB. The buffer liquid was sampled and analyzed with ICP-MS. The results yielded 2.47±0.79 fg/g of Th-232 (10.05±3.24 nano Bq/kg) and 19.84±2.04 fg/g of U-238 (246.07±25.35 nano Bq/kg). This detector was then run for an exposure of 127 kg-days. The improvement can readily be noted by comparing run-1 with run-2 in Table 5.3 specifically noting that the anomalous nuclear recoil event numbers (listed as "candidates" since they are acoustically indistinguishable from a dark matter interaction) show a significant improvement. The rate of α particles was 2.39 /(kg·day) in run 1 and 2.73 / (kg·day) in run 2. The rate of α particles did not decrease from run-1 to run-2, but anomalous events did. The chamber was limited from further running by the neutron background.

5.9 Towards a PICO-60 with a lower particulate content

The strategy to limit the particulate concentration in PICO-60 was twofold. The cleaning of PICO-60 before the run started used the pump-heater system with the spray nozzle jet and the IV was cleaned until US MIL-Std 1246C Level50 [90] was reached. A picture of the vessel being cleaned for the final time before installation is shown in Figure 5.9. The second prong of the strategy was to use an internal circulation system with a quartz stinger attached to an in-line filtration system. The system monitored the particulate load in the detector vessel by sampling and filtering the buffer liquid after the installation. The system was designed to filter out particulates suspended in the buffer liquid.

To assess cleanliness of the IV, a procedure was developed for collecting

Figure 5.9: Cleaning of the IV with the Revojet spray nozzle.

particulate samples on a filter. Every filter sample filter was then imaged with a Keyance microscope with a 250X zoom. An automated program then generated figures showing the MIL-1246C limits and the status of the sample being tested.

5.10 Final cleaning of PICO-60

The PICO-60 inner vessel was cleaned using the spray jet before it was assembled in the pressure vessel. After the installation, it was expected that some amount of particulates would have been generated by the mechanical assembly procedure. To ensure a clean system before the experiment commenced, the jar was filled with ultra-pure water and a circulation line was set up. Water was circulated through the in-line filtration system many times over and the filters were analysed under the optical microscope and the SEM. The water in the IV was rinsed until the cleanliness specifications were met (Figure 5.10). The vessel was then certified as ready and the fill of C_3F_8 commenced via distillation. After the filling of the C_3F_8, one last sample was

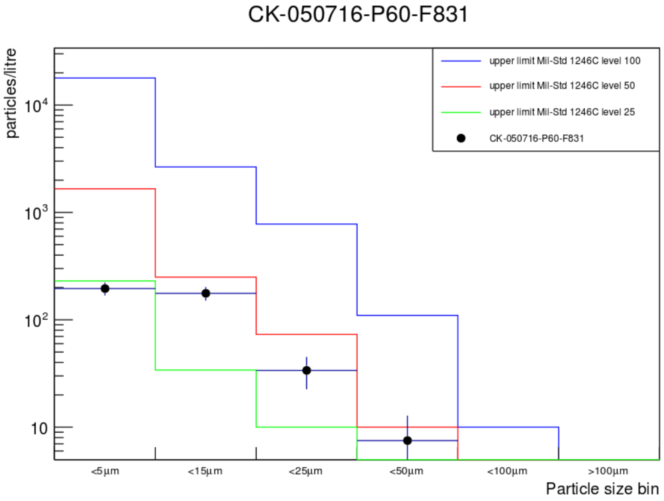

Figure 5.10: The particulate concentration in the the last filter taken before the C_3F_8 fill showing that the water in the IV, to be used as a buffer liquid, maintained the cleanliness specification.

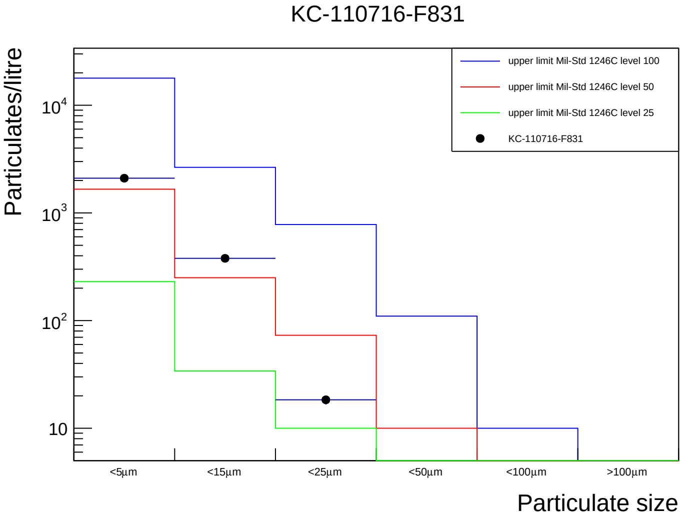

Figure 5.11: The particulate concentration in the last sample before the commencement of operations showing that the PICO-60 IV started with a vessel that was clean to the MIL-Std-1246C-100. In case a source of anomalous events were seen then the rate of those events could be compared to the state of the particulate contamination of the vessel. This sample serves as a base for such comparisons. PICO-60 operated without any such backgrounds and this comparison was ultimately not needed.

taken to establish a baseline cleanliness of the vessel before operations. The results are shown in Figure 5.11. This last sample documents the cleanliness that PICO-60 achieved after the particulate reduction efforts and before data taking started. The IV liquid was not sampled again until the decommissioning of the experiment because it was determined that the pump of the in-line filtration system created more particulates than the filters could remove. The system was therefore not used during the running of PICO-60.

5.11 Interaction of water and C_3F_8

Towards the end of the PICO-60 runs, it was noticed that the view of the IV was becoming blurred. On further inspection, droplets of water were seen accumulating on the inner wall of the vessel. Inspection of many events revealed that some of the bubbles were created by droplets, and some droplets merged during the run and traveled up along the glass vessel while still attached to the wall, leaving a water trail. The mechanism for the transport of water droplets in the detector is unknown. However since these droplets were observed to cause nucleation, lead to a need to eliminate the buffer liquid from the future PICO detectors. This observation led to the design and construction PICO-40L (the next generation of the PICO bubble chamber).

5.12 Summary

Previous PICO detectors had an anomalous source of events that were not expected and yet were acoustically indistinguishable from dark matter interactions. These events limited the sensitivity of the detector. Particulate contamination was identified as the most likely source of these events. A campaign was undertaken to characterize and understand the sources of particulates and their impact. In the course of this study, radioactivity of detector components and particulates was ruled out as the only source of the anomalous events. Efforts were made to remove particulate contamination from run 2 of PICO-2L and PICO-60. The particle counting of the buffer liquid met the MIL-Std-1246C-Level100 standard to ensure the cleanliness of PICO-60. One of the upgrades to PICO-60 was an active in-line filtration system connected to the vessel allowing samples of the liquid to be taken between runs. This was ensured that PICO-60 met the required cleanliness standard. PICO-60 was able to eliminate the source of anomalous background and conducted a 30 live day run at the 3.3 keV Seitz threshold without any nuclear recoil like background events, the details of which are shown in Chapter 6.

Chapter 6

The PICO-60 Analysis

6.1 Introduction

The PICO-60 experiment conducted two blinded dark matter search runs. The first of those was been published in [64]. This chapter presents the analysis of the data collected by PICO-60 in the second blinded run, an unblinded run and a re-analysis of the first blinded run using an updated optical reconstruction.

The PICO-60 data undergoes a series of quality cuts to ensure that only events that are well characterized are accepted for analysis. This chapter describes the data sets and the event selection cuts applied to the data.

The bubbles seen in PICO-60 can be classified into several different event classifications:

- **Wall** events are bubbles that originate at the wall. They are caused by alpha particles arising from the wall, by dissolved gases in the crevices on the surface of the wall, or by interactions involving the water adhering to the surface of the inner vessel.

- **Bulk** events are bubbles that arise inside the detector far from the walls (called the "bulk" of the active liquid). They are caused by decay of dissolved radon, or by nuclear recoil and electron recoil interactions. Those arising from the decay of dissolved radon or its daughter nuclei (by the emission of an α particle) are α **backgrounds**.

- **Surface** events are bubbles that arise from the C_3F_8-water buffer interface.

- **Multi-bubble** events are those with bubbles appearing simultaneously. These are mostly caused by neutrons.

A WIMP-nuclear recoil candidate is identified as a single bubble event that nucleates in the bulk of the active liquid. Such an event is indistinguishable from a nuclear recoil caused by a neutron. Information from cameras, piezo-electric sensors and pressure sensors is used to classify nuclear recoil, alpha and multiple scattering events so that only WIMP-nucleon recoil-like events remain for the dark matter search analysis.

The PICO-60 analysis starts with the video data used to determine the positions of the bubbles in the detector. Once the position of each bubble is reconstructed it is used to correct the response of the pressure and acoustic sensors. Information from the video analysis and from the pressure excursion as measured by the "Dytran" fast pressure transducer is used to identify events with a single bubble.

In the analyses performed before present one, the collaboration relied on "hand-scans", where every event is examined and classified as a bulk or a wall event based on features that each type of bubble presented by a human. For PICO-60 it was shown that, due to the nature of the optics and the geometry of the jar and the wide variety of experiences of hand-scanners, the results from hand-scans were inconsistent. A large part of the efforts in this analysis have been put towards eliminating the need for hand-scanning and to apply the automated image analysis algorithm locate the bubbles and the fiducial cut to classify them as wall or bulk. The details of this automated analysis are discussed in this chapter.

As described in Chapter 4, the PICO-60 imaging system uses four cameras to capture and store a series of 40 images of each event from each camera. The image resolution is 1700×1088 pixels and the dynamic range is a grey scale between 0-255. PICO-60 stores frame 30-70 in each event, where the trigger occurs at frame 50. This choice arises for historical reasons. For the commissioning of the trigger algorithm, a hundred frames were stored for every event from every camera. Where the trigger condition was first met was stored as frame 50. There were 50 pre-trigger frames and 49 post trigger frames stored along with the trigger frame. This storage scheme required 150 MB for each camera per trigger or 600 MB per trigger. The data storage infrastructure did not allow for such large amounts of data to be stored for the whole run. It was therefore decided to only store 19 post trigger frames since the compression of the vessel can be seen at around the 15^{th} frame after the trigger. To maintain symmetry the decision was made to store 20 pre-trigger frames instead of 50. Thus frames 30-70 are stored for all events with frame 50 remaining the trigger frame. This reduced the storage requirements to 240 MB per event without any significant loss of information.

6.2 Imaging and Video

The primary goal of the image analysis is to accurately reconstruct the location of each bubble in the detector. This is important because the quartz walls of the IV contain very low but nonzero amounts of radioactive material that produces nucleation near the walls. In addition, the walls themselves are uneven when examined under a microscope and can harbour crevices with air bubbles trapped in them. These sites can be starting points for nucleation and thus a thin layer of C_3F_8 covering the wall is excluded from WIMP search analysis. The position reconstruction is split into several sequential steps (summarized in Figure 6.1 and) itemized below:

AutoBub:

- For each camera, detect the frame in which the bubble(s) can first be identified (the “genesis frame") by calculating the image entropy and monitoring for a rise above a pre-determined threshold.
- Determine the bubble positions in raw pixel coordinates for each camera in which they are seen, both for the genesis frame and for up to nine subsequent frames.
- Determine the size of each bubble in each of these frames.

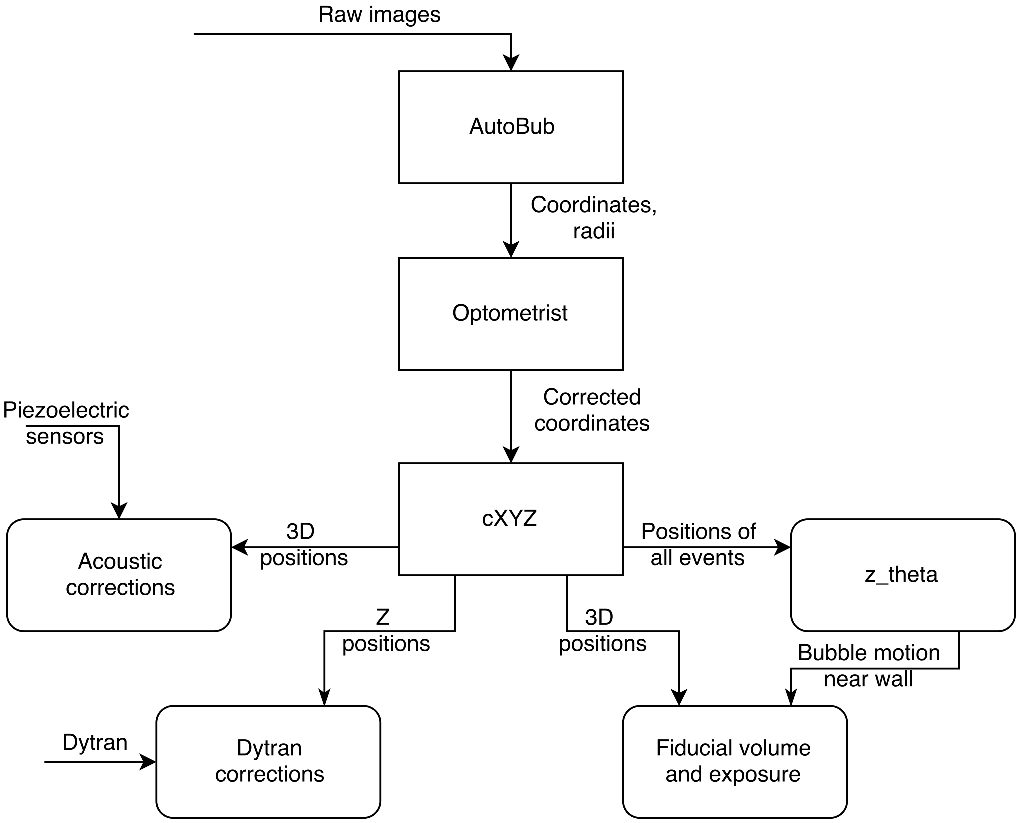

Figure 6.1: Overview of the image analysis showing that the image processing begins with AutoBub, proceeds to Optometrist and finally cXYZ. The bubble positions (output of cXYZ) is used to apply position dependent corrections to the acoustic and the fast pressure excursion (dytranCZT) data.

- Output the coordinates, size, rate of growth and movement in pixel coordinates.

Optometrist:

- Determine the positions of fiducial markers on the IV in each of the four cameras using a templated search algorithm.
- Calculate matrices to transform the known positions of the fiducial markers in the reference images to their determined positions in the images of the event being analyzed.
- The inverse of these matrices are calculated. These are called "perspective transforms" and are used to correct for the camera movement (in the next step). They are stored along with the positions of the fiducial markers.

cXYZ:

- Using the perspective transform matrices, the raw pixel coordinates of bubbles identified by AutoBub are converted into corrected pixel coordinates.
- The corrected pixel coordinates are converted to calibrated positions using a lookup table.
- The pair of cameras that have been shown to perform the best for the pixel coordinates of the bubble are then picked and the position of the bubble determined using this set of cameras are stored.

6.2.1 AutoBub algorithm

AutoBub uses image analysis algorithms from the OpenCV [91] computer vision package to detect and track nucleation bubbles in the images from the PICO-60 experiment. A right handed coordinate system is used here with the X-Y plane at the intersection between the cylinder and the bottom spheroid of the inner vessel (see Figure 6.16). The origin lies on the central axis of the cylinder that makes up the inner vessel. The y-axis is defined to be pointing away from the cameras. The flowchart in Figure 6.2 outlines the overall program.

6.2.1.A Noise and background image from the pre-trigger frames of events

AutoBub first makes a list of all events in a single run and then trains on selected frames. For each camera the background and noise in every pixel of the camera is determined. The training data set is chosen to be frame 30 and 31 from each event as these are the first two frames in an event. The training consists of finding the average of all queued frames (μ_T) and the standard deviation from the average of all pixels (σ_T). This is called a “sigma map". It is used to determine if a change in a pixel of an image is significant to the bubble finding. An example of two such maps from run 20160821_1 is shown in Figure 6.3.

6.2.1.B Finding the trigger frame

The next task performed by AutoBub is finding the first frame where the bubble is detected. This is different from the video trigger frame since the analysis is not time-critical like the trigger. The algorithm remains the same as that used for the original hardware trigger described in Section 4.5, the same image entropy S_I of the absolute difference of a frame and the preceding frame is used. Triggers that were picked up late (the bubble is seen in frame 30-31 instead of frames 45-55) are rejected using the criteria that the image entropy of the first frame satisfies the condition $S_I > 0.0005$. The threshold is empirical and was determined in trial runs. Events with a late trigger are stored with an error code in the output. These are then discarded by the rest of the image processing chain. AutoBub looks for a trigger in frame 33 through 60. It does not look any further since the compression of the IV sets in around frames 63-65 and looking for a bubble after this point generates a lot of false hits from the movement of the jar induced by the compression.

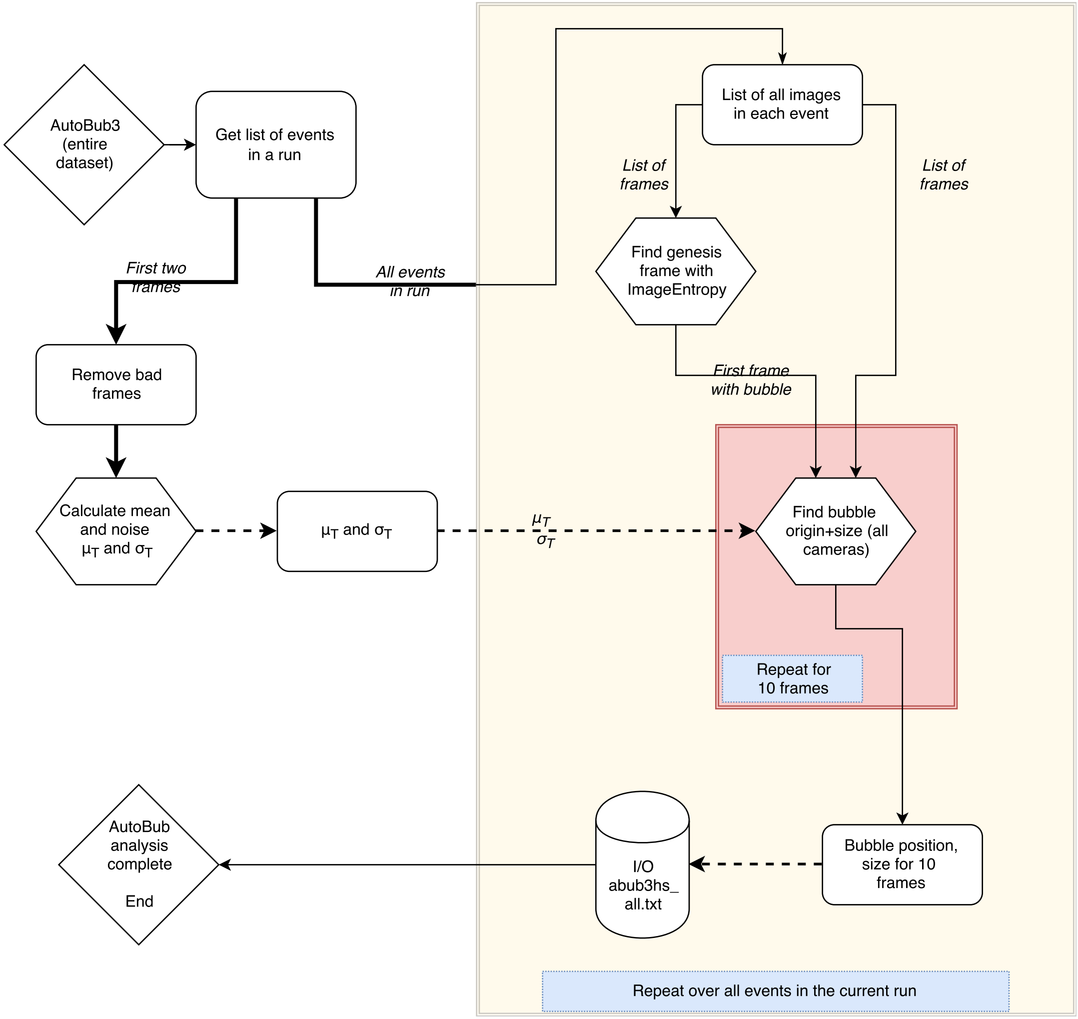

Figure 6.2: Control flow showing the overview of the AutoBub algorithm. The thick lines represent arrays of raw images (thick) and processed images/data (dashed). The hexagonal boxes represent parts of the AutoBub algorithm and the rectangular one represent auxiliary functions and temporary data storage. The italicized text represents the variable passed along from one box to another.

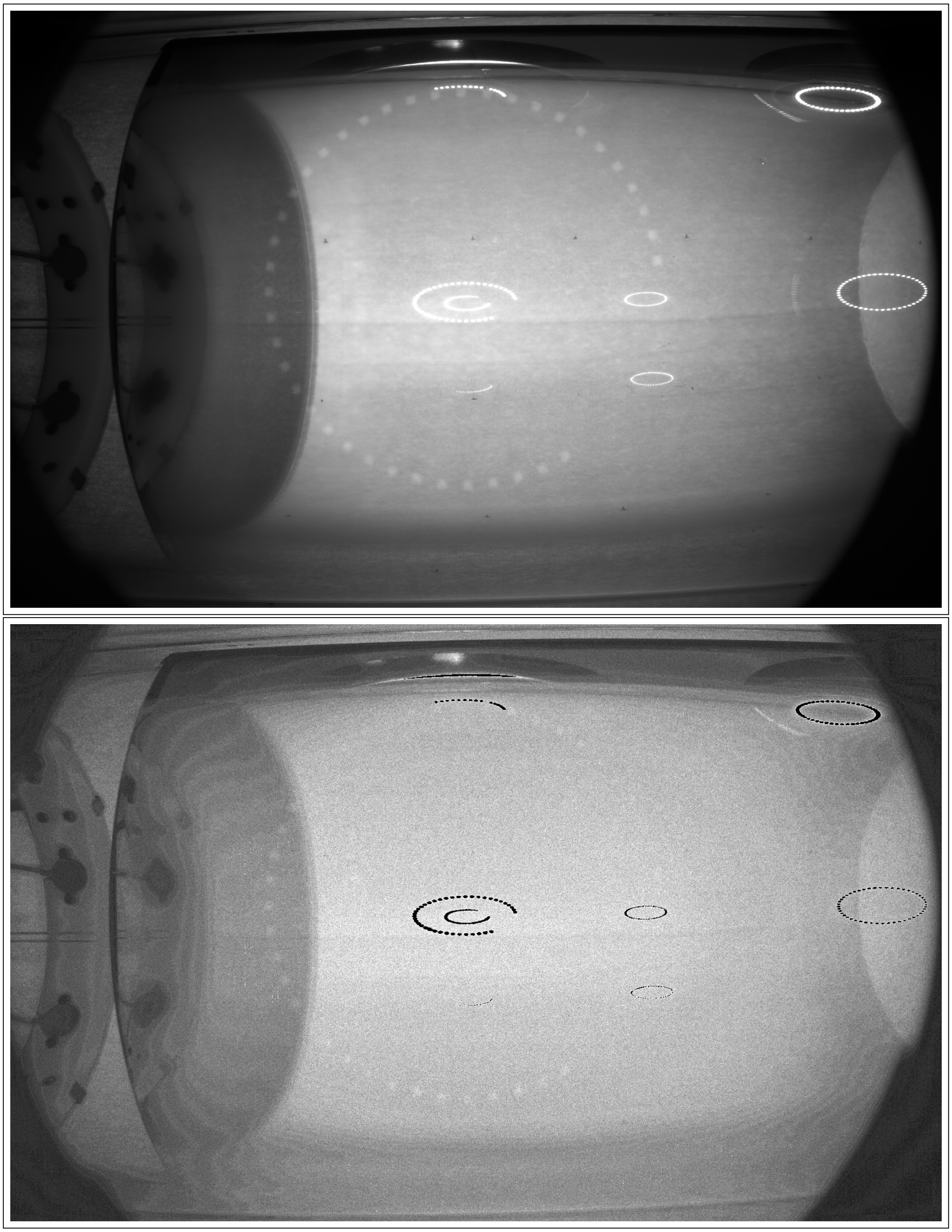

Figure 6.3: Mean μ_T (above) and sigma σ_T (below) of each pixel from the first two frames of all 16 events in 20160821_1, cam0. The dynamic range was scaled so that it can be shown in an image.

6.2.1.C Finding the centres of bubbles

The next step is the actual finding of the bubble. There are two different algorithms - one for camera 2 and the other for cameras 0, 1 and 3. When the cameras were installed, camera 2 was not focused as well as the others so the images are blurry. Since this causes problems in detecting and analyzing a smaller sized bubble the trigger frame for this camera is moved by $+1$, so that the bubbles being analyzed are larger and therefore easier to analyze.

The bubble detection algorithm and the algorithm to calculate the size of the bubble are described below. Note that in the corresponding section all variable names denote matrices. The images are represented by matrices with each element being a pixel and the value of the element being the pixel value. The images are monochrome. The operations described are matrix operations and the operands are the matrices representing images.

6.2.1.D Cameras 0,1 and 3

1. The absolute difference of $\delta F_\mu = F - \mu_T$ is taken where F is the frame with the bubble (trigger frame). A sample image of δF_μ is shown at the top in Figure 6.4.

2. Then the value of $F_{6\sigma} = \delta F_\mu - 6\sigma_T$ is calculated. This variable represents pixels at least 6σ above the noise. A sample image of $F_{6\sigma}$ is shown at the bottom in Figure 6.4.

3. A median blur is then used. The kernel of the blur operation is a 3×3 square (called a "kernel").

4. A threshold at pixel intensity of 3 is applied. Any pixel that does not pass the threshold is set to zero. The ones that pass are stored with their original value.

5. Thresholding is applied again but this time with Otsu's binarization [92]. The assumption at this point is that the image is bimodal. Otsu's binarization is used to find the threshold that separates the two modes in the image histogram. Images at this point are binarized, with one

class of pixels representing bubbles and the other noise. A sample image is shown at the top in Figure 6.5.

6. To find the bubble contours an edge detection is performed using OpenCV's `cv::findContours`. It uses the Suzuki algorithm [93] with polygonal simplification of the contours (the option used is `CV_CHAIN_APPROX_TC89_L1`. This uses the Teh-Chin chain algorithm [94]). The outputs are the contours of the bubbles. A sample image of this final state is shown at the bottom in Figure 6.5.

6.2.1.E Camera 2

Camera 2 requires a separate processing chain because the camera is not focused properly. The unfocused image can be thought of as a blur that has been applied to the image. This makes edge finding more difficult. The algorithm used for camera 2 is presented below:

1. The trigger is moved forward by a frame. This allows the bubble to grow in size and makes detection simpler.

2. The absolute difference of $\delta F_\mu = F - \mu_T$ is taken where F is the frame with the bubble (trigger frame). A sample image of δF_μ is shown at the top in Figure 6.6.

3. A blur is applied on $\sigma_{BT} = \sigma_T$ with a 3×3 box kernel. A sample image of σ_{BT} is shown at the bottom in Figure 6.6.

4. Then the value of $F_{6\sigma} = \delta F_\mu - 6\sigma_{BT}$ is calculated.

5. A blur is applied on $F_{6\sigma}$ with a 3×3 box kernel.

6. At this point the bubbles are darker than the shadows on the retroreflector. To remove the shadows, thresholding is applied on $F_{6\sigma}$ using Otsu's binarization. The pixels that pass the threshold are set to zero and if they are below the threshold then their original value is retained.

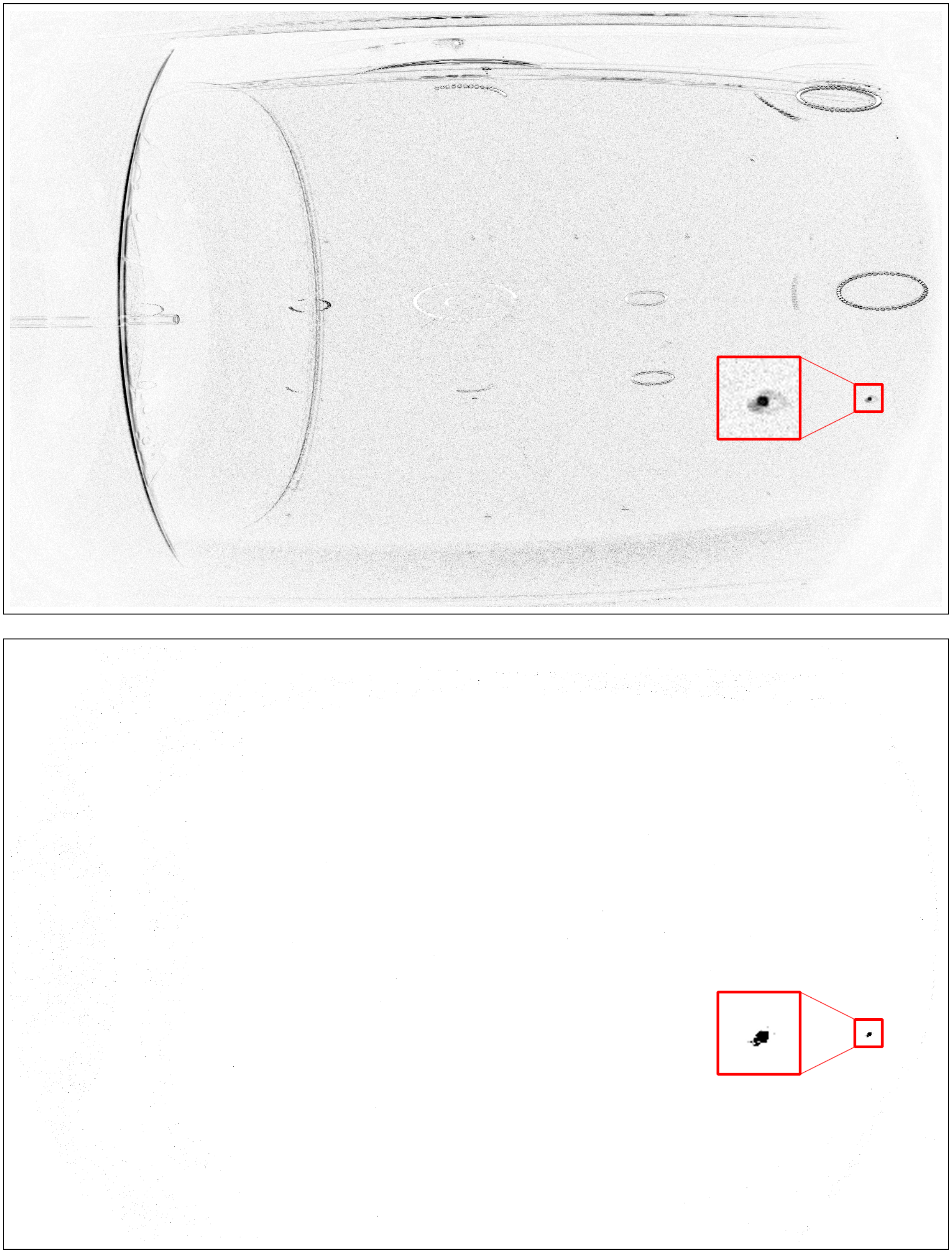

Figure 6.4: Images from the processing of an event in one camera with the AutoBub algorithm, step 1 and 2. The figure at the top shows δF_{μ}. In the figure at the bottom $F_{6\sigma}$ highlights the residual bubble visible at the bottom right. Note: The intensity of the pixels of the images have been scaled to aid visualization.

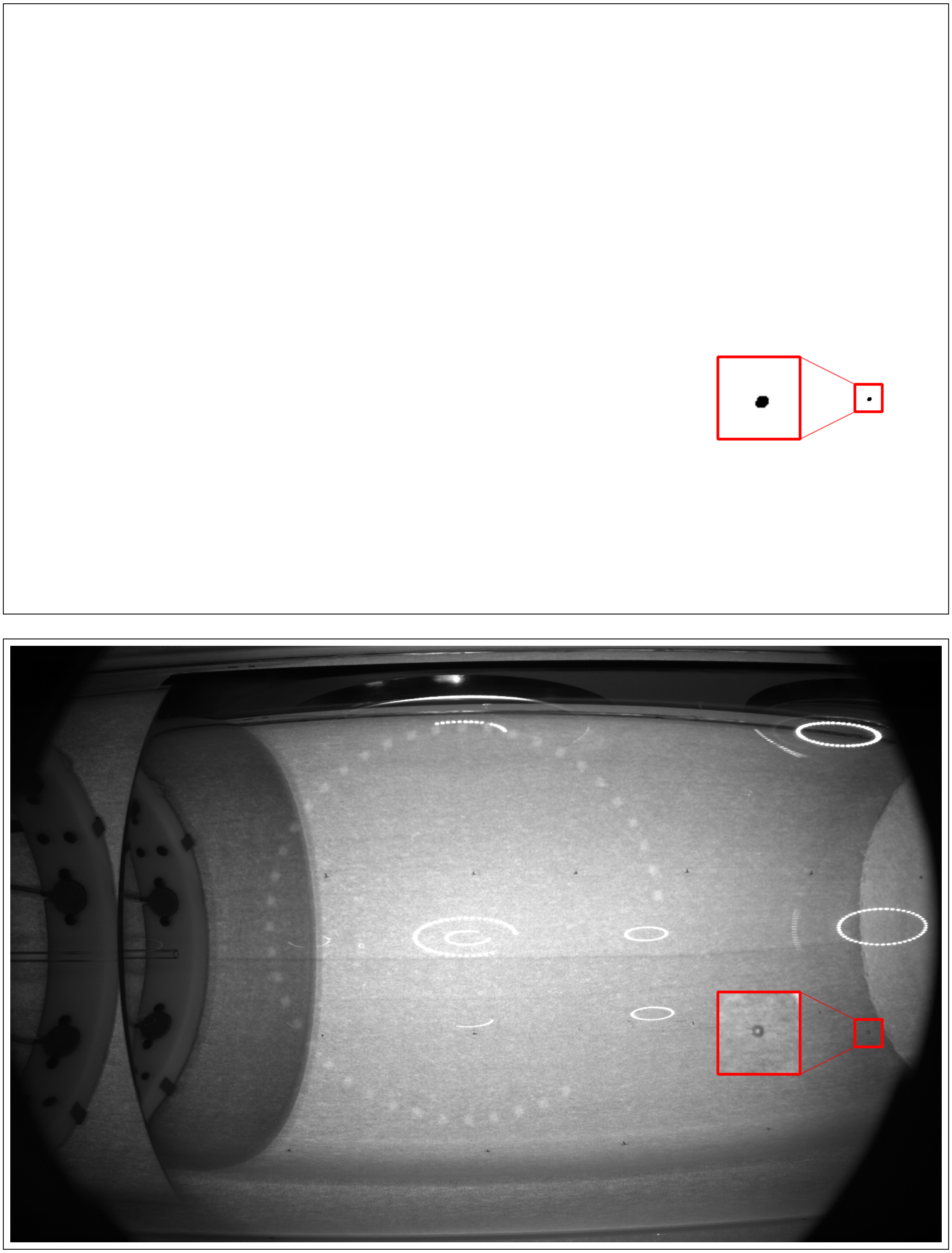

Figure 6.5: Images from the processing of an event in one camera with the AutoBub algorithm, step 5 and 6. The figure at the top shows the noise removed and the bubble clearly visible as the only entity in the right side of the image near the bottom. The figure at the bottom shows the final result with the position of the detected bubble superimposed on the original frame.

7. A threshold is applied again suppressing pixels with values less than 10 to remove noise. A sample image is shown at the top in Figure 6.7.

8. At this point, both bubbles and ripples will pass all the cuts and transforms. However if `cv::findContours` is used on ripples, then it segfaults due to a bug in OpenCV. It is thus important to perform a check of whether the image is of a bubble or a ripple before proceeding to the next step. This is done by checking if the image histogram has any entries above a pixel value of 60. If it does, it is likely to be a bubble. If it doesn't, it is likely to be a ripple. This was empirically discovered and is prone to failures in cases where the bubble is in a region where the dynamic range of bubbles is suppressed. An unfortunate consequence of this operation is that bubbles on the surface are missed once in a while. The alternative is to accept the crashes and re-start the program from the next event onward or manually exclude the events with known ripples. This choice was not available due to the setup of the data processing grid.

9. The bubble is between 4-6 pixels in size at this stage. An edge detection is performed using Opencv's `cv::findContours`. It uses the Suzuki algorithm with polygonal simplification of the contours just like the other cameras. The outputs are the contours of the bubbles. A sample image of this final state is shown at the bottom in Figure 6.7.

6.2.1.F Calculation of the centre of the bubble and tracking

The calculation of the centre of the bubble is done in two steps. In the first step the contour of the bubble is located using OpenCV's built in method `cv::findContours` which uses the Suzuki algorithm to locate the contour of blobs that pass a threshold cut. This was described in the previous section.

Then `cv::moments(contours[i]);` is used to calculate all of the moments up to the third order of the contour. The spatial moments of the image

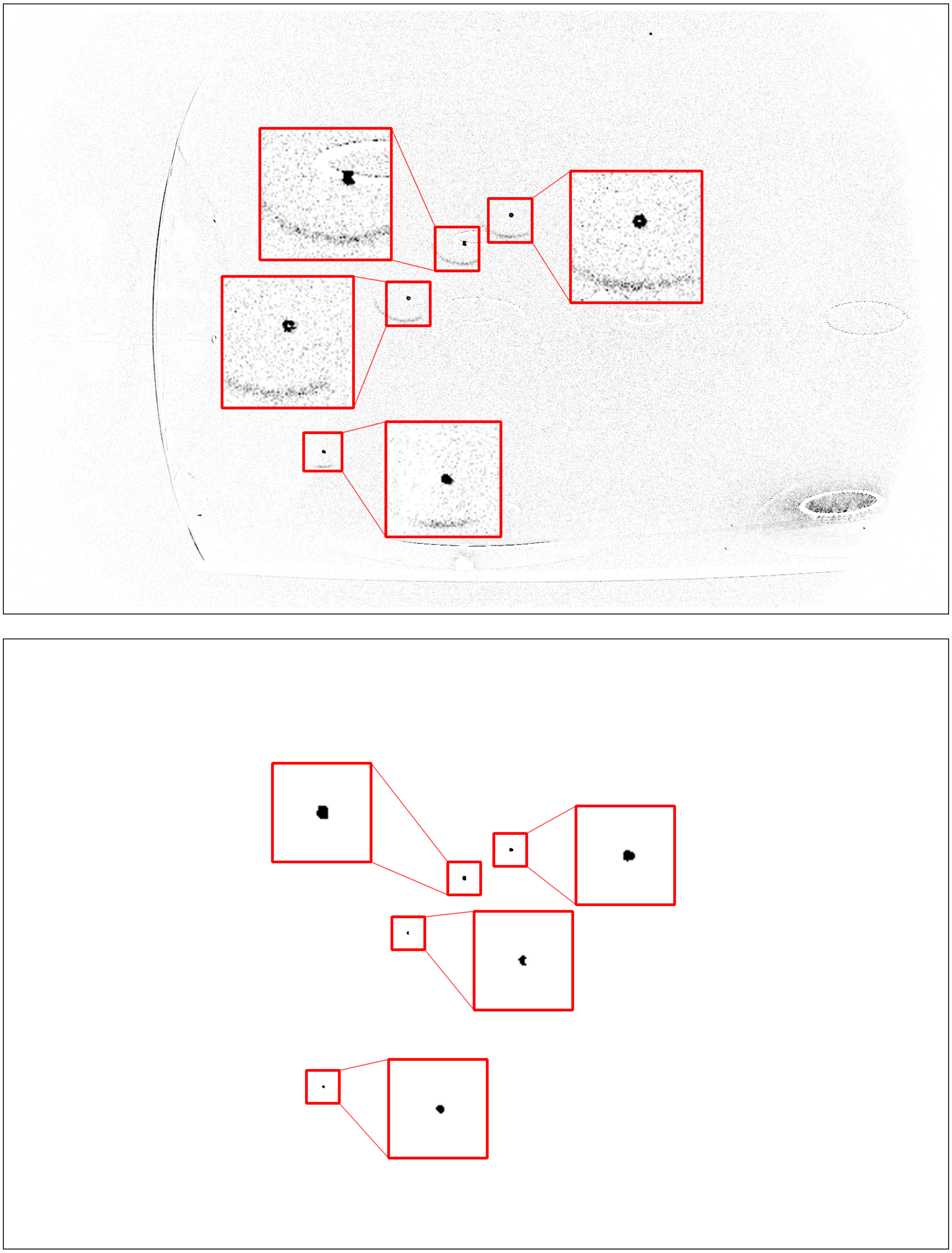

Figure 6.6: An image as it goes through the AutoBub algorithm for camera 2. Top: δF_{μ}. Bottom: Applied blur, noise map subtracted and threshold applied (steps 3-7).

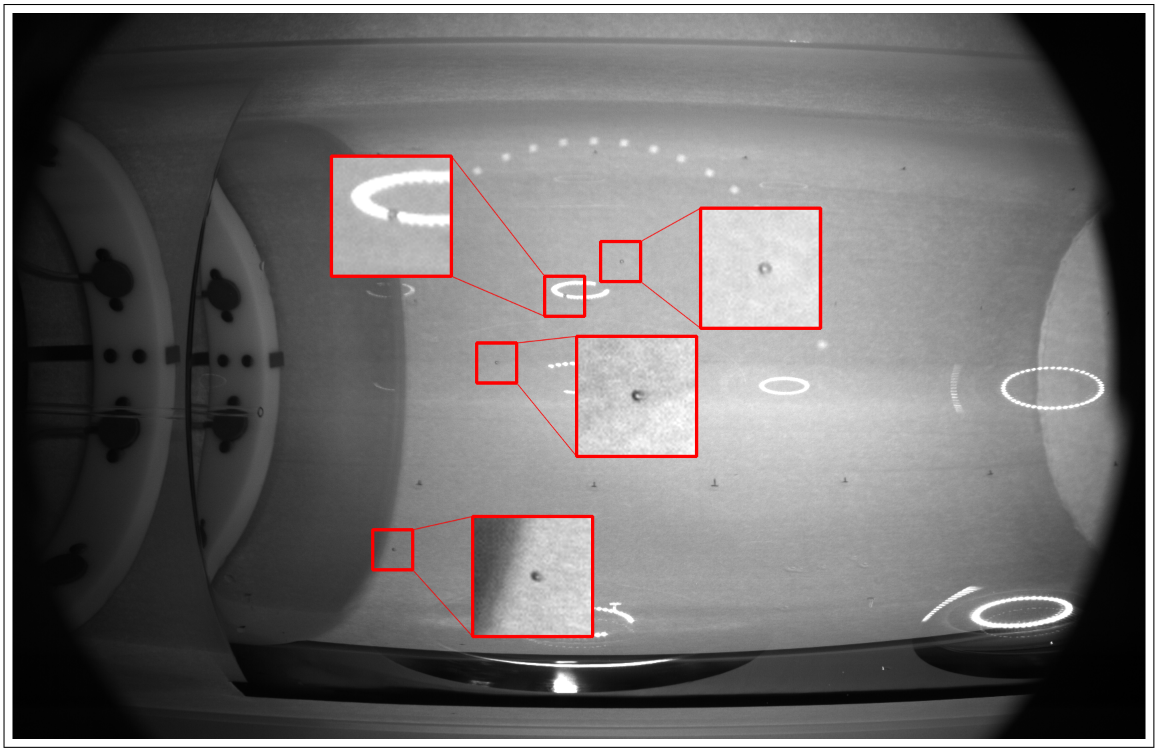

Figure 6.7: Final results of the bubble detection as the image goes through the AutoBub algorithm for camera 2. This image is a continuation of Figure 6.6.

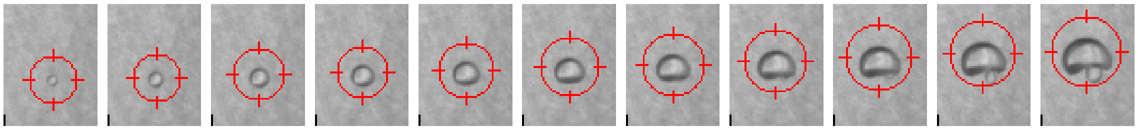

Figure 6.8: Autobub tracking of an example event over 11 frames. The resolution of the image is 50×65 pixels. This bubble is a wall event.

are calculated as

$$m_{ji} = \sum_{x,y} (C(x,y) \cdot x^j \cdot y^i) \tag{6.1}$$

where C is the contour of the bubble. These spatial moments are called mass centres. The centre of mass of the contour (which is defined to be the centre of the bubble) then is defined as

$$(\bar{x}, \bar{y}) = \left(\frac{m_{10}}{m_{00}}, \frac{m_{01}}{m_{00}} \right) \tag{6.2}$$

The “centre of mass" approach offers a sub-pixel resolution. Mass centres also offer the ability to accurately locate the centre of the bubble regardless of how the bubble oscillates in its growth and can thus be used to track the bubble as it grows.

AutoBub repeats the same analysis on the ten frames following the trigger frame to track the motion of the bubble and its evolution in size. The individual positions of the bubbles are then stored in a list in memory. To construct a track of the motion of the bubble, AutoBub needs to match a bubble from one frame to another. This is done with the following criteria: the next bubble must have moved <5 pixels vertically and <4 pixels horizontally to exclude mis-reconstructed events. The individual positions are then stored. The bubble radius in pixel space is calculated by taking the median distance of the contour from its mass centre. This is added to the list of stored positions as the bubble radius along with the frame number to which the position and the radius belongs. A sequence showing a bubble as it was tracked by this algorithm is shown in Figure 6.8. The cross hair indicates the reconstructed position of the bubble.

Camera	Fiducial marks
0	10
1	11
2	14
3	11

Table 6.1: Number of fiducial marks per camera tracked by ‘Optometrist’

6.2.2 Optometrist - Camera motion correction

It was observed during the run that Camera-1 (cam1 for short) moves in position several times during the run, most notably around the 06th of October 2016 and thereafter. Although the motion results in shifts less than 10 pixels, not correcting for this motion results in an inaccurate event position in 3D space by as much as 10mm. Thus, a motion tracker tracks the fiducial marks on the vessel and then calculates a correction matrix. This is then used to remove the effect of the camera movements by shifting and rotating the images so that all the marks are in the same position as in run 20160912_4 event 0 which the optics lookup table was built with reference to.

The camera motion tracker tracks fiducial markers on the wall of the jar. The number of fiducial markers tracked in each camera is summarized in table 6.1. The routine `cv::matchTemplate` is used to calculate a probability map for the templates of the marks that are matched to 50×50 areas around each fiducial marker. Then `cv:minMaxLoc` is used to locate the most probable point. Then a box of 3×3 pixels is taken around the most probable point and a weighted mean of pixel position is found to calculate the location of the key point with subpixel accuracy.

The impact of not correcting the motion of the cameras is captured in the image in Figure 6.9.

After all the fiducial marks are found, the function `cv::findHomography` is used to find a 1-to-1 map: a perspective transform between all pixels in the reference data set and the data being analyzed. This Homography matrix is then stored in the output. This is used to correct the positions from AutoBub before they are used in the 3D reconstruction algorithm.

The events reconstructed at r = 145mm arise from the wall of the IV.

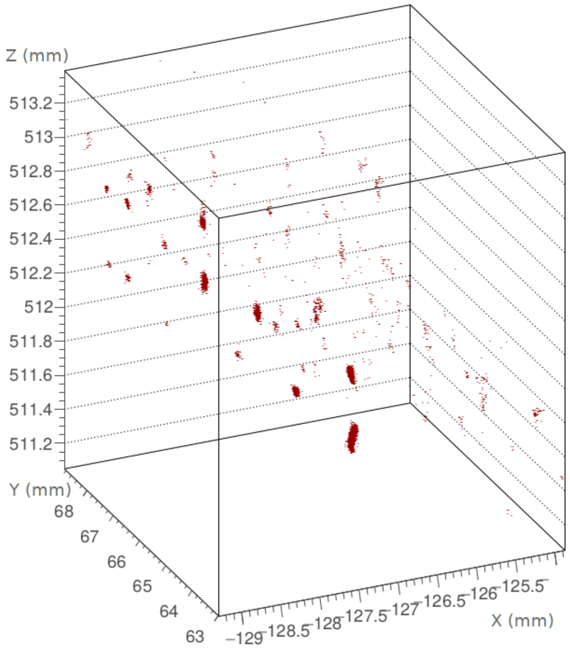

Figure 6.9: One fiducial mark reconstructed before jar correction, zoomed in. Each point represents an expansion. It can be seen that the fiducial mark moves by upto 5 mm in each direction.

These wall events can be used to locate the reconstructed position of the wall (Figure 6.10). It can be seen that the reconstructed mean position of the wall was different in the portion of the detector close to the cameras compared to the portion far away. The reconstructed geometry of the vessel does not resemble the shape of the vessel especially near the top. After application of the corrections the vessel geometry was fixed. Figure 6.11 shows the position of the events arising from the wall after application of the camera motion correction algorithm in the top part of the jar. The camera motion correction was not applied in the publication of the PICO-60 data from Run BGB33 [64]. The camera motion correction is for the first time used for the analysis of the complete exposure of PICO-60.

6.2.3 From pixel coordinates to 3D position in the detector

The uncertainty in the position of the wall can be inferred from the width of the histogram of positions of wall bubbles. This can also be taken as the

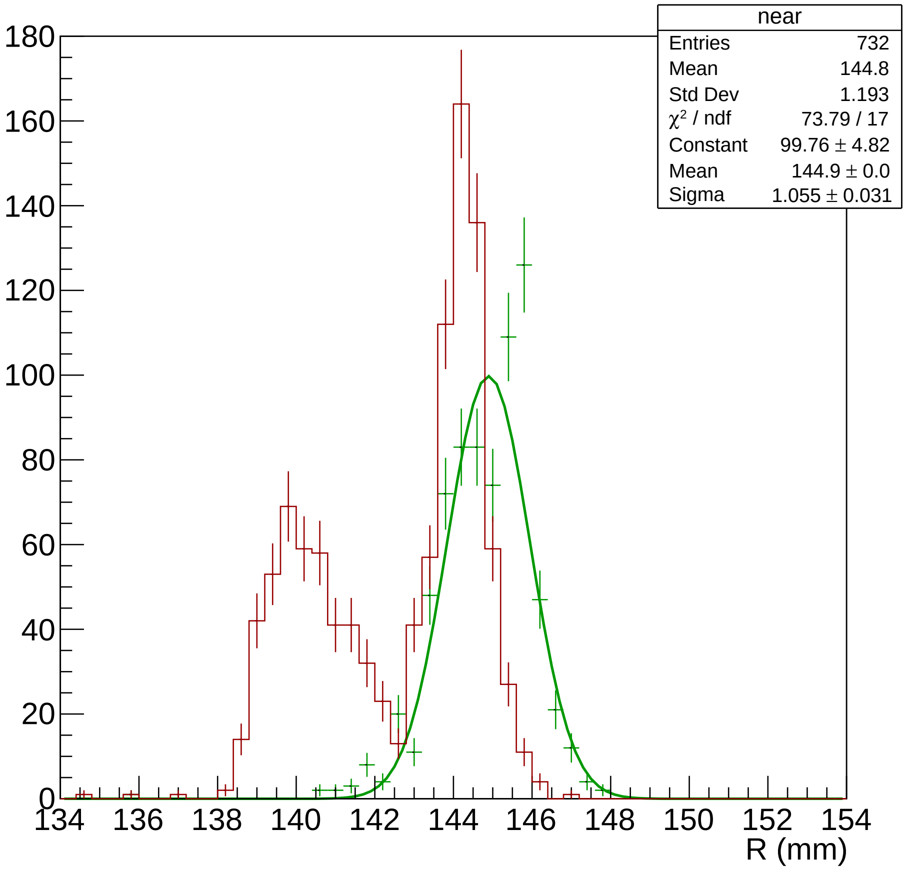

Figure 6.10: A histogram of the radial position of wall events from the top part of the detector. The side close to the cameras is marked in green and the one further away in red. Without the camera movement correction the shape of the far side side of the vessel does not resemble its physical geometry. The skew is severe enough that the distribution of wall events in this region is not Gaussian.

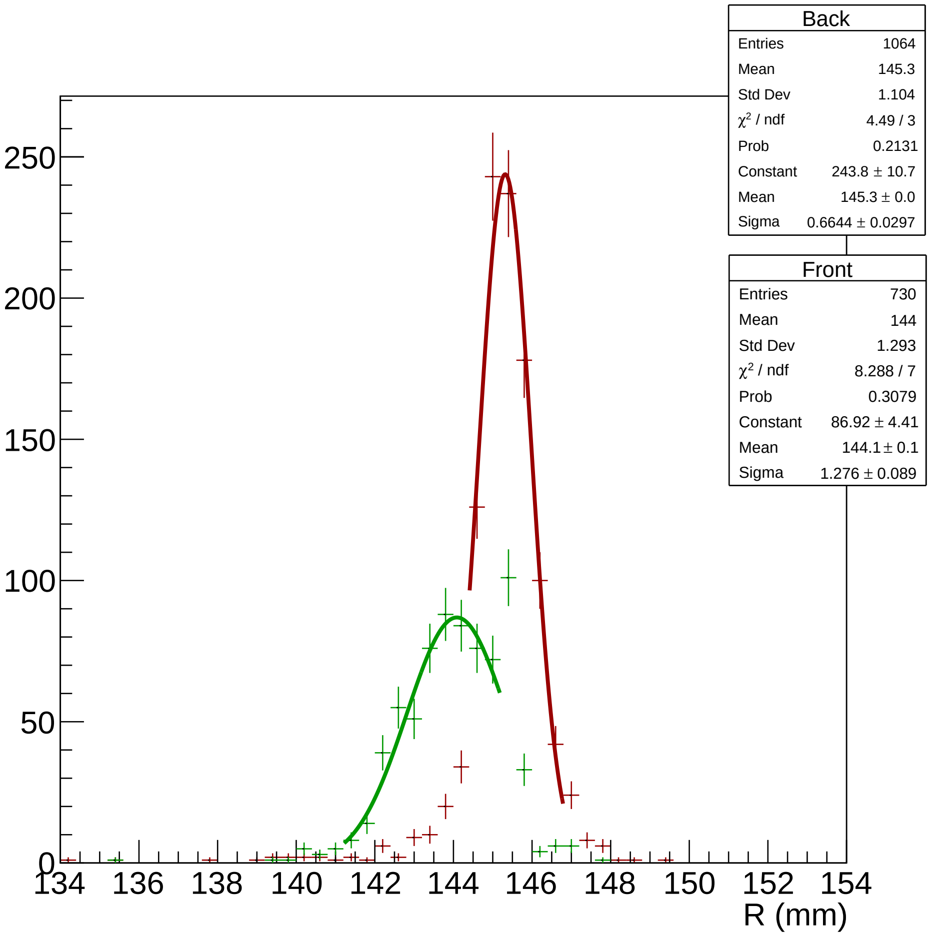

Figure 6.11: Continued from Figure 6.10 . The figure shows a histogram of the radial position of wall events on the top part of the detector after the camera movement correction has been applied. The side close to the cameras is marked in green and the one further away in red. The correction fixed the severe skew shown in Figure 6.10.

uncertainty of the position of a bubble as determined by the 3D reconstruction algorithm. This uncertainty varies with height in the vessel.

The XYZ algorithm converts the pixel coordinates that AutoBub generates to 3D positions. It converts a set of pixel coordinates reconstructed from one image into a "ray of light" in 3D that is generated based on a lookup table that stores two points in 3D space defining the line. The stereo vision gives up to four such rays which are skewed at an angle with respect to one another. In the first publication of the PICO-60 data from Run BGB33 [64] the algorithm selected the two rays with the closest approach to locate the position of the bubble. The centre between the two points of closest approach was picked as the position of the bubble.

This process had several shortcomings, namely

- The two rays with the closest approach may not be the most accurate. For example, near the bottom, the camera combination of Camera 2 (the camera that is slightly out of focus) and Camera 3 reconstruct the bubble outside the dimensions of the jar.
- The accuracy of determining the bubble multiplicity fell sharply as the number of bubbles increased.
- The code was slow and used a large amount of memory. While this is acceptable for production code that is automated, it presents a significant hindrance for a newer algorithm during testing.
- The uncertainity in the position of the bubble was large such that the fiducial volume started 6 mm from the wall in the best possible case and 13mm from the wall in the worst possible case.

To address these problems a new 3D reconstruction algorithm "cXYZ" was developed. All of the highlighted problems except for the accuracy of the bubble multiplicity has been addressed by cXYZ. cXYZ generates the rays of light from the camera pixel coordinates reconstructed by AutoBub and corrected for the camera motion by Optometrist. However cXYZ uses a set of

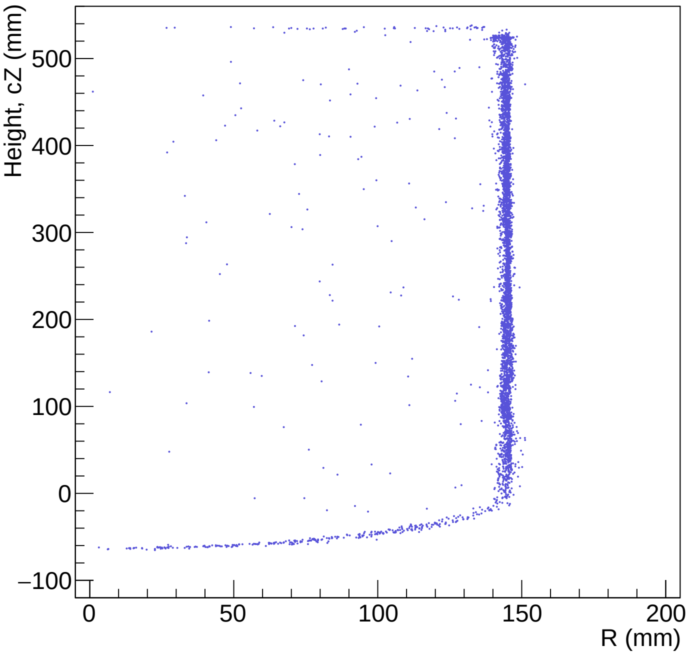

Figure 6.12: Single bubble events from background runs at 2.4 keV Seitz threshold with the camera motion corrected and processed by cXYZ with the camera selection rules.

rules to determine the best camera pair to define the position of a bubble on the basis of the location of the pixel coordinate of the bubble. This algorithm improves the accuracy of the position of the bubble. cXYZ also requires that the frame where the bubble is first seen not differ by more than 6 frames between cameras (17.4ms or 30ms depending on the frame speed).

The result of the camera selection rules can be seen in Figure 6.12, where all data with a single bubble are shown. The uncertainty in the position reconstruction is between 0.9mm and 0.7mm depending on the location in the jar.

cXYZ was optimized to process the entire PICO dataset in less than 1 second with less than 1 megabyte of memory required. cXYZ was designed to work on single bubble events only. Extending cXYZ to multiple bubbles with a robust algorithm to determine the bubble multiplicity accurately could not be completed for this analysis and is left as a future scope of work.

6.2.4 Bubble radius determination

The information presented by AutoBub to cXYZ are the horizontal and vertical pixel coordinates (h_i,v_i) and the image radius of the bubble (r_i). cXYZ uses these inputs to construct three points in the 2D pixel space for each camera, namely: ($h_i - r_i$, v_i), (h_i,v_i) and ($h_i + r_i$, v_i) before processing begins. The radius is added to h_i because the raw images are flipped sideways. These 3 points serve as the bottom, centre and top of the bubble. Bubbles from each camera undergo the same procedure for generating 3 points. Each of these points is then transformed into 3D coordinates. Thus instead of a single coordinate, each bubble now produces 3D positions for the centre, top and bottom. The average of the distance between the top and middle and the bottom and middle is stored as the radius. This data can be used to study the growth of the bubble in different parts of the detector and infer thermodynamic conditions inside the vessel (See Chapter 8).

6.3 Pressure analysis

The transient pressure excursion measurement during an event from the Dytran fast pressure transducer (See 4.3.2) is used to characterize bubble multiplicity. In the previous PICO chambers, the Dytran was used to set the fiducial volume. After the present optical analysis techniques were developed the Dytran is no longer used to define the fiducial volume but it is used to check for incorrect classification of wall events as bulk by the optical analysis.

The general strategy to analyze the fast pressure data is to fit the trace to a polynomial in the time window of bubble expansion. To locate the bounds of the time window, the fast pressure trace is filtered with a Butterworth low pass filter at 40Hz to remove the high frequency component. The time of genesis of the bubble is determined using the piezoelectric acoustic sensors and provides the lower bound of the time window akin to a starting point from where the bubble growth happens. The average of the signal before, t_0, is used to subtract the DC component of the signal. The upper bound of the time window is defined by the point at which the compression of the chamber starts. To find this time, the derivative of the fast pressure trace is taken. An empirically determined threshold is used to calculate the start of the compression t_{end}. The DC subtracted pressure trace between t_0 and t_{end} is fitted to the function $y = at^4$. A graph of a fast pressure trace and the fit is shown in Figure 6.13.

The value of a in the fitted function is the Dytran fast pressure excursion parameter and is useful as a measure of the rate of expansion of the bubble. The raw value of the Dytran fitted parameter is scaled so that a single bulk bubble has a value of 1. The rate of expansion depends on the pressure of the liquid around a bubble. The pressure of the liquid varies with the depth. The Dytran variable is corrected for the pressure differential with depth. The compressibility of the liquid changes with the temperature. The Dytran value is corrected for this effect for all the different run conditions. It was also observed that the mean Dytran value drifts over time although the reasons behind this phenomena are not known. The Dytran variable is also corrected for this effect. A histogram of the bubble multiplicity of events in the bulk as determined by the corrected Dytran value in a dark matter search run is shown in Figure 6.14. In the figure it can be seen that the accuracy of Dytran parameter drops off after 4 bubbles. This is because the correction for the depth is inaccurate for events with multiple bubbles since only a single bubble's depth information is used to correct the signal.

6.4 Acoustic analysis

The PICO-60 experiment was equipped with 8 piezo-electric acoustic sensors. However some of the sensors could not tolerate the pressure conditions and five failed by the time the first dark matter search commenced. Another sensor failed before the second run. The PICO-60 chamber is much larger than PICO-2L chambers. Combined with the new coupling between piezo sensors and the glass wall of the jar resulted in very low signal to noise ratio from the acoustic sensors. The surviving piezo-electric sensors were piezo-3, piezo-4 and piezo-7. Out of these, piezo-4 failed after the first run in January 2017.

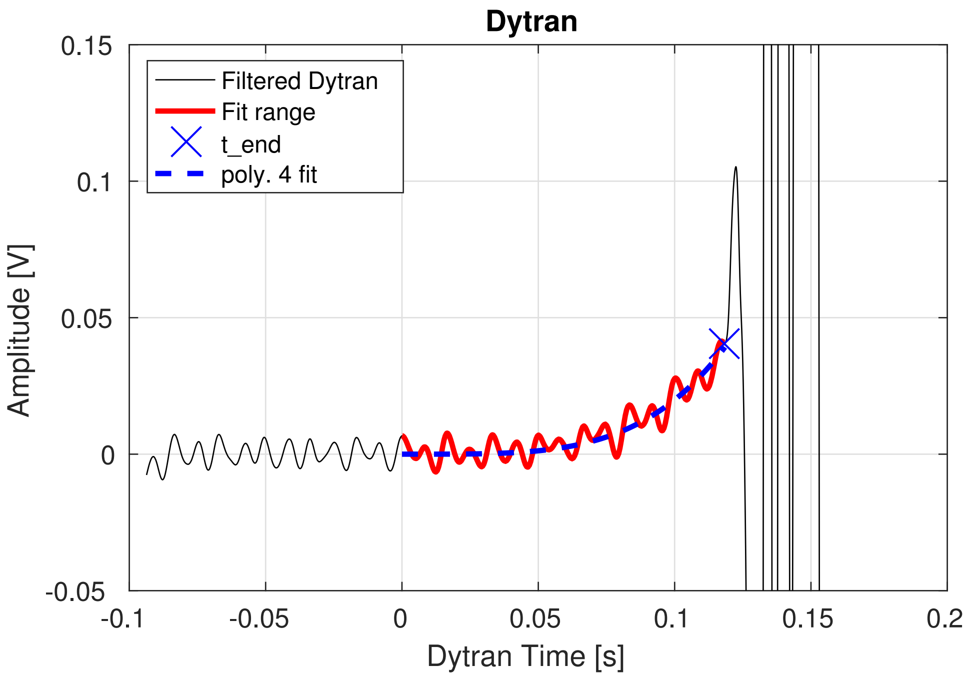

Figure 6.13: A fit to the fast pressure data from the Dytran transducer. The graph shows an event from the 16 °C, 30 psi (2.4 keV Seitz threshold) dataset. (Credit: G. Giroux)

To analyze the acoustic data, the first task is to find the time of origin of the signal, t_0. To do this, the waveforms from the two best sensors (3 and 7) are taken. A first order Butterworth band pass filter between 7 kHz and 15 kHz is applied. This frequency band was empirically found to have the maximum signal to noise ratio for the acoustic signature of the bubble. The signal envelope is then calculated by taking the absolute value of the signal's Hilbert transform. The envelope is smoothed over 250 samples. The threshold for finding the signal starting time t_0 is calculated using the 2000th through the 30000th sample of the signal envelope. The threshold is 7 standard deviations from the noise. If no samples in the envelope exceed the threshold then t_0 is set to 0. The process is shown in Figure 6.15. The t_0 offset and the noise of the acoustic signal was monitored over time to assess any damage or degradation in the response of the piezoelectric sensors. No further degradation in the signal strength of piezo sensor 3 and 7 was seen.

With the time of origin of the signal t_0 determined, the next task is to

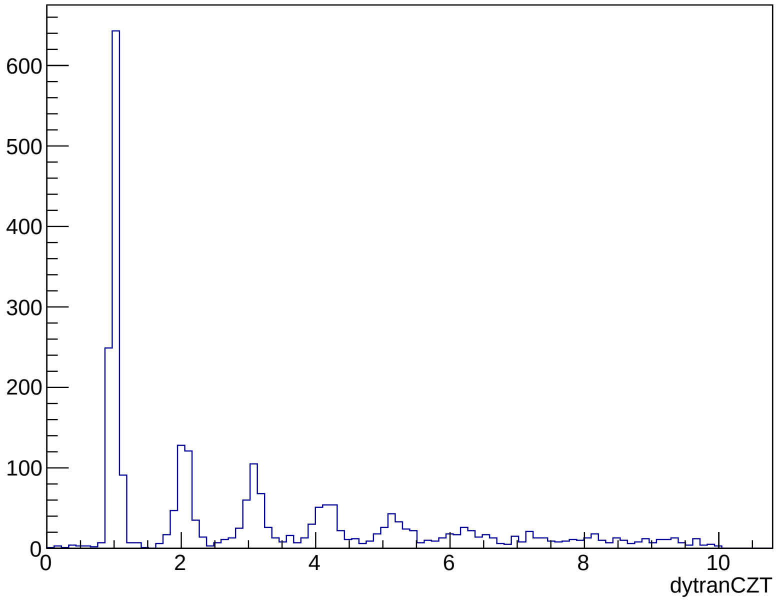

Figure 6.14: Bubble multiplicity from the Dytran fast pressure excursion (dytranCZT) of all the bubbles in the bulk in the 16 °C, 30 psi dataset excluding engineering runs. The fast pressure parameter can be used to determine the bubble multiplicity.

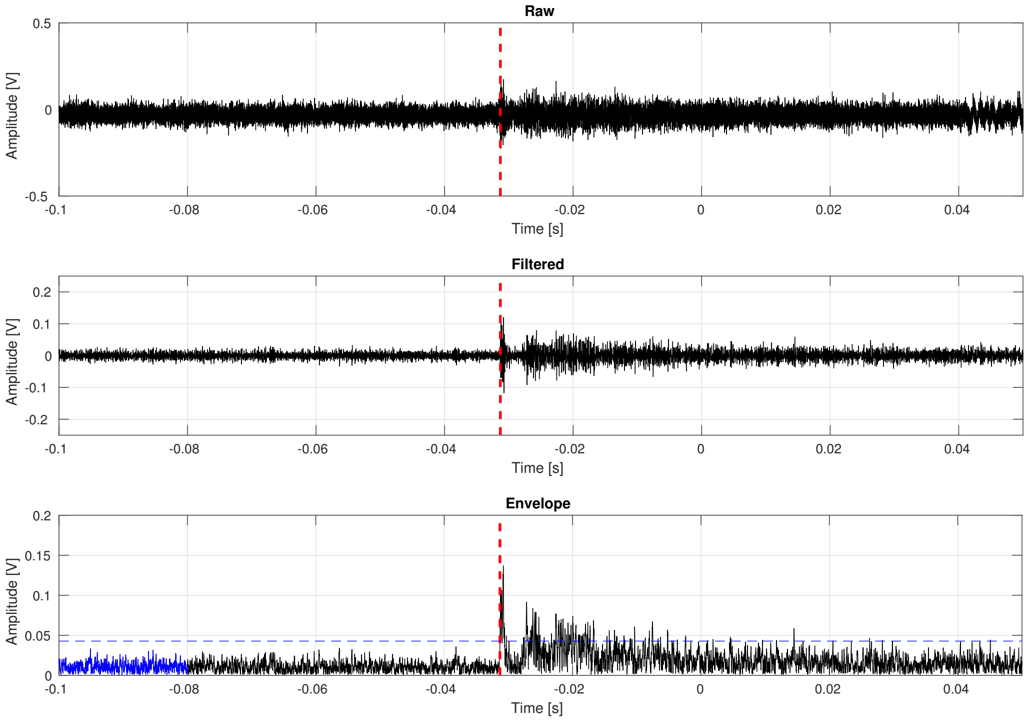

Figure 6.15: Figure illustrating the steps for finding the onset time t_0 in an acoustic signal with an example acoustic trace. Credit: G. Giroux.

calculate the acoustic energy of an event. The acoustic energy of the signal is calculated in 8 different frequency bands in a time window that corresponds to the noise (-0.05 to -0.01 seconds before the signal starts at t_0) and the signal region (-0.0020 to 0.0380 seconds after t_0). In PICO-60 the frequency bin edges of the bands were chosen at 1, 5, 15, 30, 55, 90, 120, 150 and 300 kHz, respectively. The measured acoustic energies in each band are then stored. Different frequency bands offer a window to observe the bubble growth at different time scales. Band 5 and 6 (55-120 kHz) offer the maximum amount of discrimination between a nuclear recoil and an alpha event and are used in the analysis.

The acoustic power measured by each piezoelectric sensor is dependent on the location of the bubble. It is expected to vary with the distance in a $1/R^2$ fashion where R is the distance between the sensor and the bubble. The signal also varies with the angle it makes with the piezoelectric crystal and the depth at which the event occurs. Profile histograms of R^2, Z and ϕ of the acoustic power are generated for each of the eight frequency bins and are fitted with splines as a model for correction functions. The acoustic energy is then corrected for the position.

6.5 Fiducial volume definition

The different types of data that are available for analysis in PICO-60 have been introduced. This section describes how the data is used to determine recoil or WIMP-like events to perform a dark matter search. The PICO-60 analysis begins with imaging and the definition of the fiducial volume.

The geometry of the IV is a cylinder at the top with a sphere at the bottom joined by a part of another sphere called the knuckle. However, when the locations of events were plotted in the R-Z plane along with including the nominal wall geometry it was seen that the jar geometry does not coincide with the locations of the bubbles (assumed to form on the wall of the vessel). The previous three piece geometry along with the location of wall events is shown in Figure 6.16. It was found that the geometry below the cylinder would be

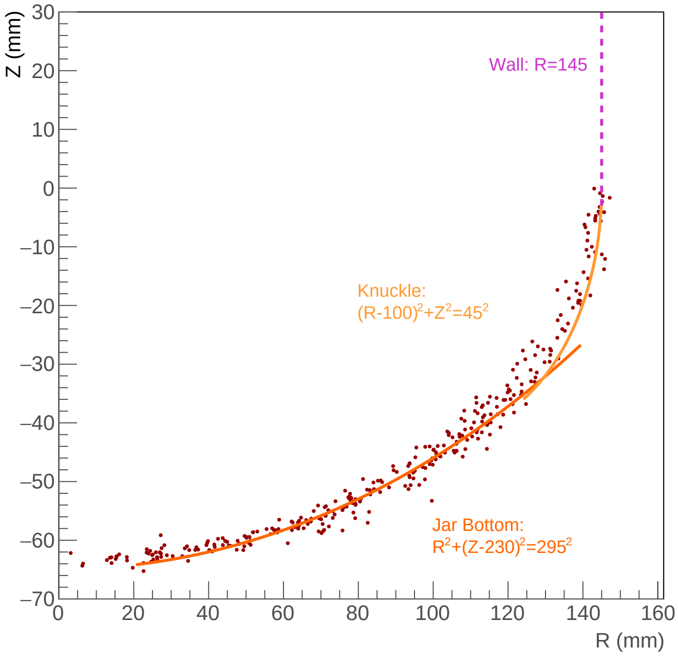

Figure 6.16: The IV R-Z plane with detected events. The old three-piece geometry of the cylindrical jar, the spherical bottom and the part toroid "knuckle" of the vessel is outlined. The wall events from the bottom portion of the jar are overlayed to show the mismatch between the geometry and the location of the events.

better represented by an ellipse in the R-Z plane (which makes the shape a half-spheroid).

The 16 °C, 30 psi (2.4 keV Seitz threshold) background and WIMP search data were fitted to such an oblate spheroid. The result is shown in Figure 6.17, fit to the function $\frac{x^2}{a^2} + \frac{y^2}{b^2} = 1$, were $a = (145.009 \pm 0.225)$ mm and $b = (63.900 \pm 0.118)$ mm. This is in excellent agreement with where the spheroid should meet the cylinder and the bottom of the vessel as applied in the old geometry.

The interface of the buffer liquid with the active liquid generates a lot of nucleations. These events are generally known as "surface events" and can be used to infer the surface level of the active liquid. The surface level varies with the thermodynamic conditions of the active liquid. A histogram showing the number of events as a function of the Z-position can be used to determine the

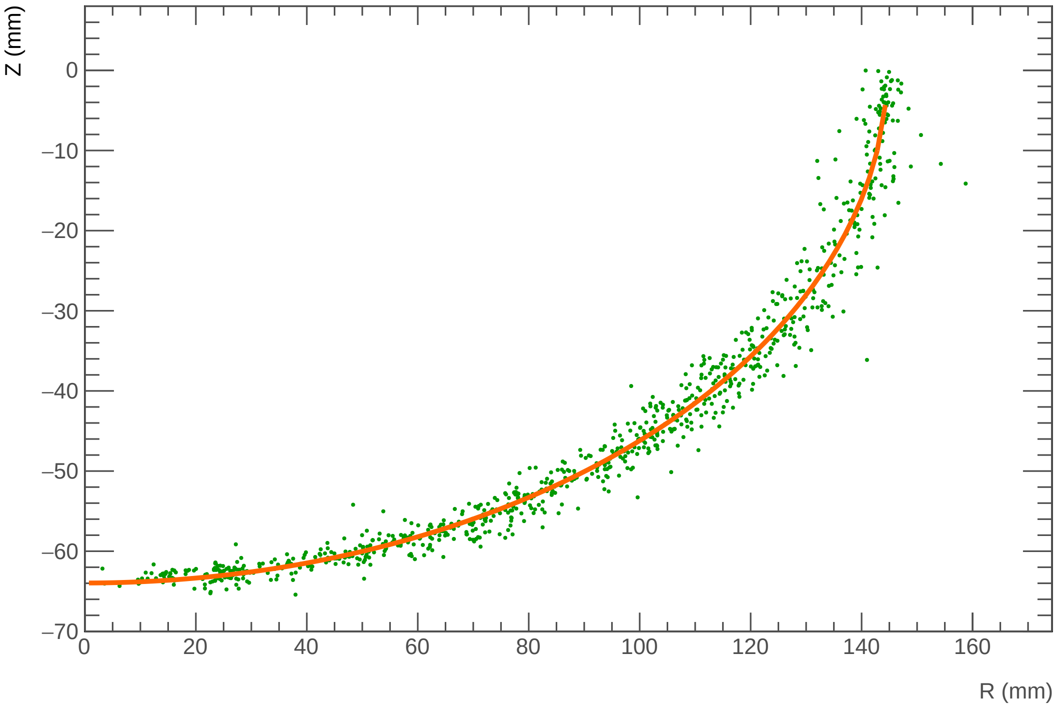

Figure 6.17: R-Z plane with events and the updated geometry.

Location in Z (mm)	Mean deviation from 145mm (in mm)
0-80	0.11±0.09
80-160	0.29±0.05
160-300	-0.071±0.033
300-400	0.24±0.04
400-519	0.49±0.04

Table 6.2: The mean value of deviation from 145 mm for the location of wall events in all 16 °C, 30 psi background data.

position of the surface. These histograms, made with the data from the dark matter searches and background runs, are shown in Figure 6.18. The fiducial zone must exclude these events. The surface level is used to determine the total volume (and thus mass) of the active liquid in the detector.

The radius of the cylindrical portion can similarly be found by fitting the histogram of all events with respect to their radial positions in background and dark matter search runs where most of the nucleations originate at the wall. This number was measured in different parts of the jar, divided into slices in the Z-axis. The recorded values are summarized in Table 6.2. The location of the wall as inferred from the position of wall events is constant with respect to the Z-position. This is a check on the positioning algorithm's accuracy in different parts of the IV. As seen from Table 6.2, the positioning accuracy, although different, is within the specifications of the IV.

With the geometry now defined, an estimate of the total volume could be made. The volume of the half spheroid is $(2.86 \pm 0.02)\,\mathrm{L}$. The volume of the active liquid is different at different thresholds but the mass is assumed to be the same. Here, the calculation for 16 °C at 30 psi (2.4 keV Seitz threshold) is performed. The volume of the cylinder is calculated to be $(35.23 \pm 0.08)\,\mathrm{L}$. The total volume is therefore $(38.0 \pm 0.1)\,\mathrm{L}$. To calculate the error in measurement, the average deviation of the centre of the "wall" as defined by the mean location of all wall events, can be used to repeat the volume calculation; once by taking the higher side of the 1σ confidence interval for the radius of the cylinder and the axes of the spheroid, and again for the lower side. The uncertainty is defined by the difference between the higher and the lower

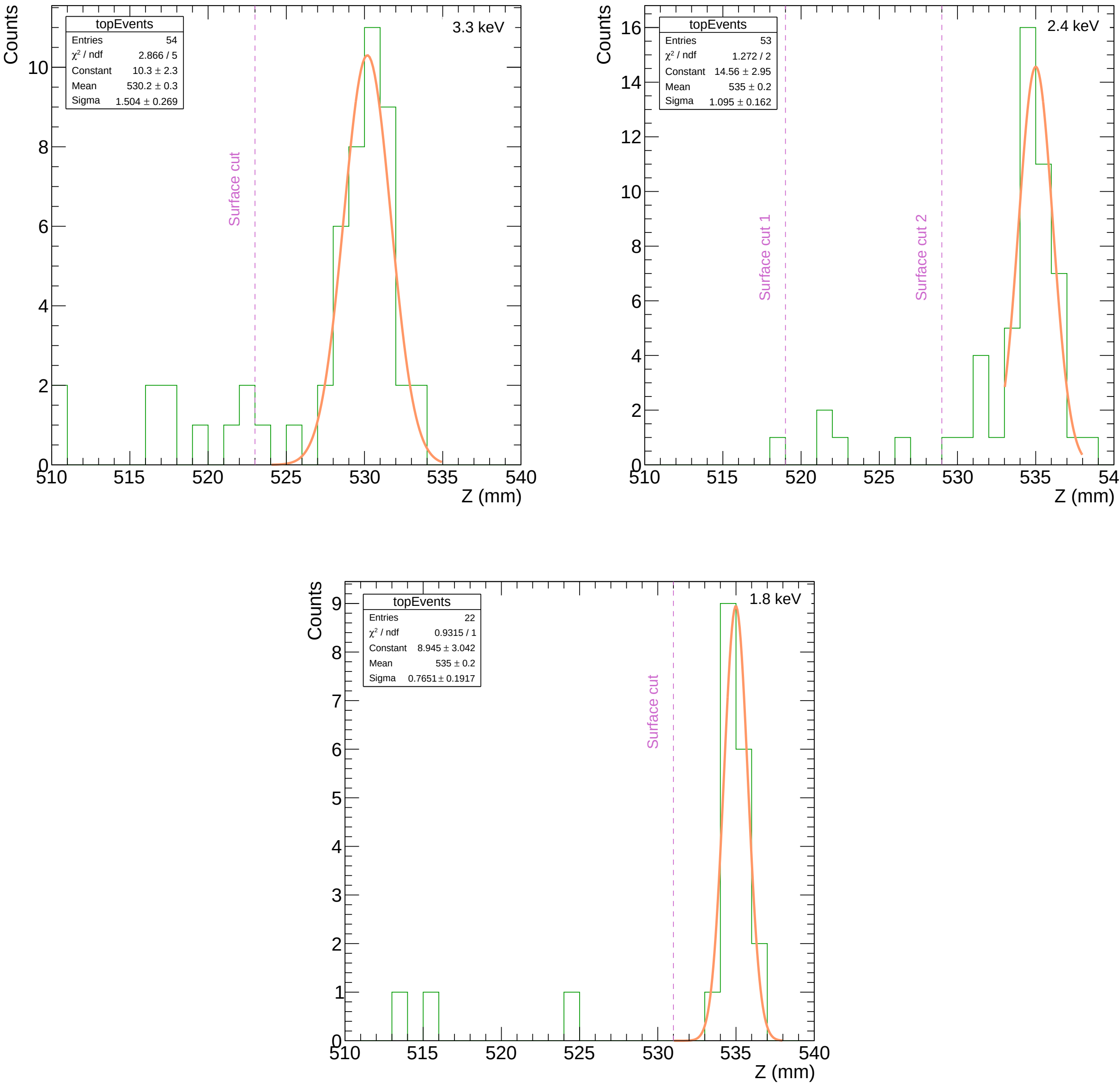

Figure 6.18: The position of the surface for the three different thermodynamic conditions corresponding to Seitz thresholds of 3.3 keV, 2.4 keV and 1.8 keV. The surface can be seen where the number of events spike. The data was taken from background and dark matter search runs.

estimates.

$$V_{total} = (38.0 \pm 0.1)\,\mathrm{L} \tag{6.3}$$

This gives an estimate for the total volume of the liquid at Seitz threshold of (2.4 keV). Assuming the density is constant throughout and is sufficiently accurate as given by REFPROPS [80] at ρ=1.3675 kg/L (at 14.05 °C, 30 psi) the mass of the C_3F_8 is

$$M_{C_3F_8} = (51.96 \pm 0.14)\,\mathrm{kg}. \tag{6.4}$$

The mass was calculated at the other thresholds and found to be consistent with this number.

6.5.0.A Bubble Track Zenith Angle Cut

While the fiducial volume can be entirely defined by the location of the wall events, it is possible to introduce a variable that describes the angle the track of a bubble makes with respect to the zenith, this can be used to increase the fiducial volume by discriminating bulk events from wall events. In the annular region close to the wall, information from the tracks made by the bubbles is used to determine if they originate on the wall or in the bulk. In this case, bubbles with tracks identified by reconstruction quality variable, $Q_{cxyz} = 1$ or 2 (described in Section 6.5.0.B), are considered.

Each bubble in the chamber is tracked for 10 frames after genesis. The angle between a track and the Z-direction is called the zenith angle of the track. The bubbles that are formed in the bulk of the liquid rise vertically due to buoyancy as they expand. Bubbles near the wall of the vessel, however, can only expand inwards and thus the centre of the bubble moves at a zenith angle that is large compared to the bulk events. A graph illustrating tracks in the R-Z plane is shown in Figure 6.19. This angle can be calculated by taking the track in the R-Z plane and fitting the 2D distance from the z-axis (R) versus t to get the slope dR/dt and fitting Z versus t to get dZ/dt. Dividing the two quantities gives dR/dZ, the arctangent of which is the zenith angle

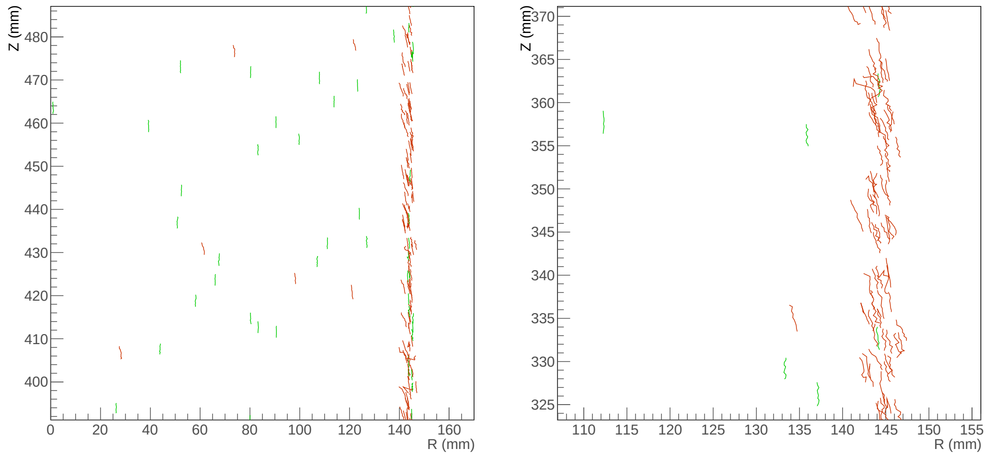

Figure 6.19: (Left) Graph showing bubble tracks in the bulk and (right, zoomed in) tracks near the wall from the run BGB24. Orange tracks fail $\theta_z < 0.11$ and the green tracks pass. The unit of length is mm.

θ_z (variable `z_theta` in the dataset). The statistical errors and the goodness of fits are propagated throughout this calculation and stored along with the zenith angle.

For θ_z to be used to discriminate between bulk events and wall events, a cut value needs to be defined. The initial cut was chosen to be $\theta_z < 0.21$ rad by considering Figure 6.20, that shows the radial position of all single events in the 2.4 keV threshold gamma calibration runs versus their θ_z value. The efficiency of the θ_z cut was evaluated on the data from γ calibration runs at each threshold. Cuts of $0 < Z < 500$ and $d_w > 10$ were applied to select a large sample of bulk single events where d_w is the closest distance of an event from the wall in mm. For the purpose of the efficiency calculation, all the events in this dataset are considered to be true bulk events. The efficiency of θ_z is then the number of events from this dataset that are classified as bulk events divided by the total number of events in the sample. The rationale behind this calculation is that the efficiency of θ_z is that for classifying bulk events.

The initially selected $\theta_z < 0.21$ rad cut has a 95% acceptance. Optimizing a set of cuts is a multi-dimensional problem, and a final round of heuristic

Value	Description
0	cXYZ did not process this event (usually if number of bubbles is not 1 or if cXYZ failed)
1	cXYZ processed this event and successfully reconstructed the full track (all 10 points)
2	cXYZ processed the event but was able to partially reconstruct the track (less than 10 points)
3	cXYZ processed the genesis coordinates of the event but was unable to reconstruct the track
4	cXYZ produced a track > 10 points indicating an IO error.

Table 6.3: The values that reconstruction quality variable Q_{cxyz} can take and their descriptions

optimization was needed to remove wall events and performed. A θ_z cut yielded a value between 0.11 - 0.12 rad based on the thermodynamic conditions with a final efficiency of 90%.

6.5.0.B Image Reconstruction Quality Cut

The reconstruction quality cXYZ is given by Q_{cxyz}. Table 6.3 describes the values this parameter can take and their descriptions. For events outside of the annulus or the wall where the bubble tracking information is not used, Q_{cxyz} need not be considered.

The efficiency of Q_{cxyz} is evaluated by comparing all events in the entire PICO-60 data-set that are single bubble, and is not a part of an engineering run. The efficiency of a good reconstruction with usable track information (Q_{cxyz}=1 or 2) is 99.7 %.

6.5.0.C Frame difference at first detection cut

cXYZ outputs the frame number where it first “sees" the bubble in every camera. Not all cameras see the bubble at the same time due to refraction and viewing angles, so some cameras might detect the presence of the bubble later than others. Normally this would not cause a problem with the localization of the bubble if the time difference between two cameras, used to reconstruct the position, is low. If the time difference is high, then the reconstructed positions are biased and such camera combinations are rejected if an alternative (a

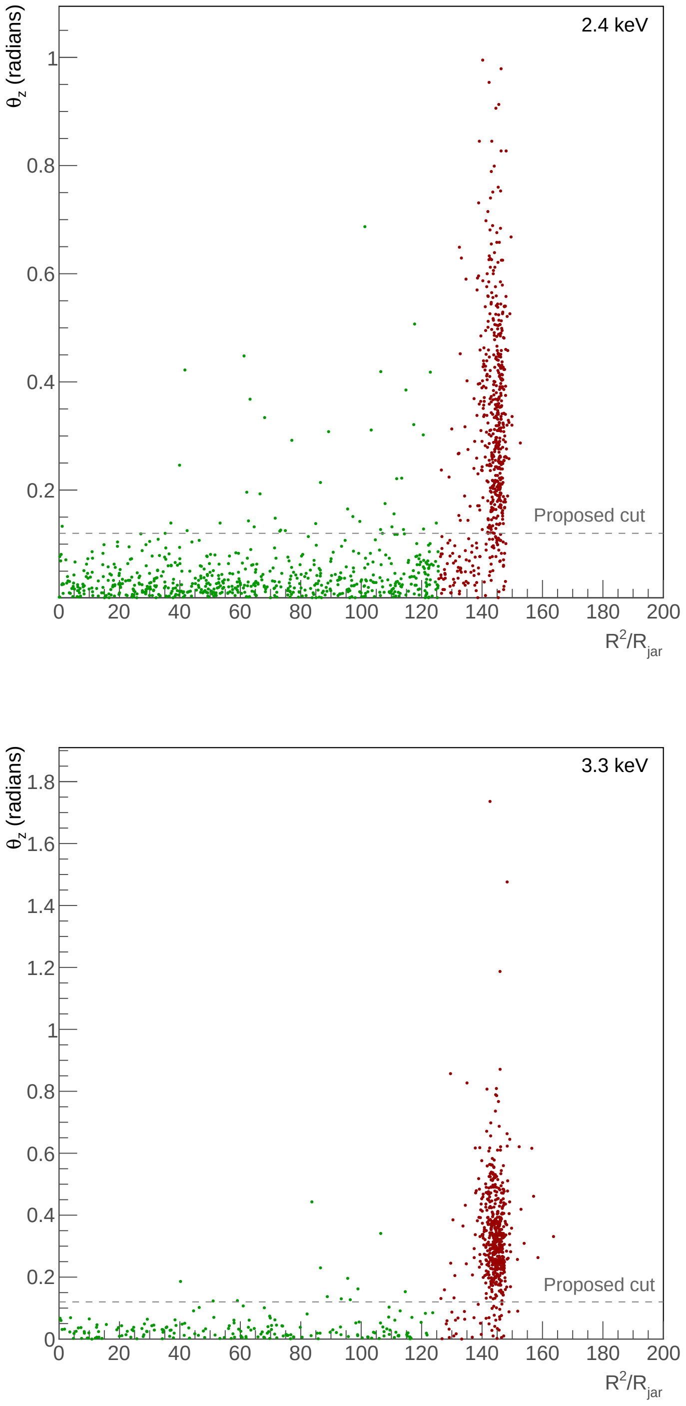

Figure 6.20: The cut on a graph of θ_z versus the radial distance of each single bubble event from the γ-calibration runs at 2.4keV and 3.3 keV Seitz threshold. The bulk events are marked in green and the wall events are marked in red. The efficiency of selecting bulk events is 93.35% for 2.4 keV and 93.68% for 3.3 keV data. The proposed cut value is at 0.11 for the 2.4 keV threshold data and at 0.12 for the 3.3 keV threshold data.

third camera) is available. If only two cameras capture an event, and one of the cameras detect the bubble at a much later time than the other camera, then the position of the bubble has a large error associated with it. This is not a problem for events in the fiducial volume. This is critical for events near the wall, where such a delay makes it impossible to determine if the origin of the event is the wall, and, thus, a cut has to be applied near the walls to exclude such bubbles from the analysis. The quantity ΔF_{gen} (variable `gFrameDiff` in the data) measures the frame difference between the first detection of the bubble in the two cameras used to reconstruct the image. At present a cut of 10 frames (29 ms for the 2.4 keV dataset and 50 ms for the 3.3 keV dataset) is applied.

The efficiency of the cut on the ΔF_{gen} variable is determined by how many events in the fiducial volume passes the cut. Thus the efficiency of the cut is determined by taking a region defined by $0 < Z < 500$ mm and $d_w > 10$ mm. The data used were all the single bulk bubbles from γ calibration runs for the respective threshold. All cuts described in further detail in Section 6.6.2 (data quality) and Section 6.6.3 (single bubble selection) are applied. The efficiency of this cut is 99.3% for the 3.3 keV data, 99.06% for the 2.4 keV dataset and 99.56% for the 1.8 keV data.

6.5.1 Towards a fiducial volume

With all variables in place it is now possible to define a fiducial volume for the PICO-60 extended physics run. There are 3 boundaries of the fiducial volume that need to be defined for each run: the cylindrical part, the spheroid at the bottom, and the surface. The data used to generate the fiducial definitions are the unblind background and the blind dark matter search runs (BGB33 and BGB24). These runs have many more events near the walls in proportion to bulk events, and are thus ideal for setting clear fiducial boundaries.

6.5.1.A Surface

Figure 6.18 was used to determine on a fiducial boundary of the surface. For the 3.3 keV and 1.8 keV the surface definition was set to 523 and 531 mm in Z by

Seitz Threshold	Fiducial surface boundary
3.3 keV	$Z < 523$
2.4 keV	$(Z < 519)$ OR $(Z > 519$ AND $Z < 529$ AND $\Delta F_{gen} < 10)$
1.8 keV	$Z < 531$

Table 6.4: The final definitions of the fiducial surface boundary in the three different thermodynamic conditions defined by their Seitz thresholds.

just selecting a cut that removes all the surface events. For 2.4 keV, a simple surface cut was, initially set at Z=529 mm. However it was observed that there were events between Z=519 mm and Z=529 mm which were ambiguous in origin due to large frame delays in one of the cameras. Since the origin of such events cannot be reliably determined, a $\Delta F_{gen} < 10$ cut was applied to exclude such events.

6.5.1.B Bottom Spheroid

After the re-definition of the geometry at the bottom, a histogram of distance of a bubble from the wall, d_w was made for each of the thermodynamic conditions. One such graph for the 2.4 keV data is shown in Figure 6.21. Note that the bottom is not expected to change with thermodynamic conditions, but it was observed that the bottom started to accumulate water droplets with time. Since the dark matter search with different thresholds were conducted chronologically, these thresholds can be used to separate the run conditions with time.

From the histograms in Figure 6.21, an initial fiducial limit was set at $d_w = 6\,\text{mm}$. However it was noted that there were some events at distances of up to 10 mm from the wall that had a large value of ΔF_{gen}. In addition, some wall events tend to hug the surface of the vessel until they detach themselves giving a large value of the zenith angle of their track. Taking these events into consideration, the final fiducial limits for the spheroidal part of the vessel are summarized in Table 6.5. It was observed that some of the bubbles arising from the wall in the spheroidal region cling to the walls before detaching themselves. The θ_z variable can distinguish these events and a cut of $\theta_z < 0.12$ rad is

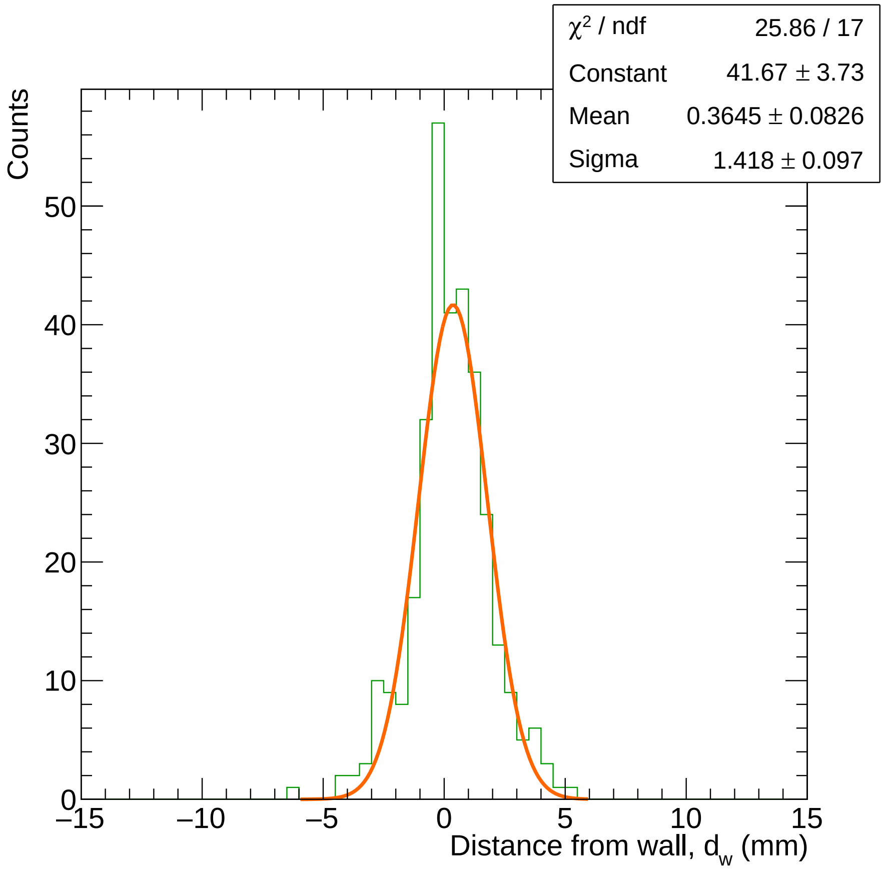

Figure 6.21: Histogram of d_W of all events in the spheroidal part of the jar. Data taken from all 2.4 keV background and dark matter search runs.

Seitz Threshold	Fiducial definition in the bottom spheroid
3.3 keV	($Z < 0$ AND $5 < d_w < 10$ AND $0 < \theta_z < 0.12$) OR ($Z \leq 0$ AND $d_w > 10$)
2.4 keV	$d_w > 5.0$ AND $Z < 0.0$
1.8 keV	$d_w > 5$ AND $Z < 0$ AND $\Delta F_{gen} < 10$

Table 6.5: The final definitions of the fiducial boundary of the spheroidal bottom part for the three different thermodynamic conditions defined here as Seitz thresholds.

applied in this region to exclude these events from the fiducial volume.

6.5.2 Cylindrical section

The cylindrical section can be subdivided into two zones. Events reconstructed in the inner zone up to a certain radius are considered "bulk" without any additional criteria. This is different for the higher frame rate data than the lower frame rate data. For the lower frame rate this zone ranges from the centre to 135 mm. For the faster frame rate 2.4 keV data this section is from the centre to 138 mm and for 1.8 keV it is up to 135 mm.

The second zone is an annular region that uses information from the zenith angle of the track described in Section 6.5.0.A, the goodness of fit for the zenith angle, and the frame difference between the cameras used to detect the bubble to determine if the bubble originates in the bulk of the liquid or the walls. The cuts were chosen heuristically by looking at graphs of θ_z vs d_w. The effect that the θ_z cut has on a wall distribution can be readily seen by comparing the two histograms in Figure 6.22. This figure shows all events between Z=400 mm and 500 mm as a function of the distance from the wall (x-axis), assumed to be at 145 mm. The red histogram shows all events and the green one shows events with a cut on large values of θ_z. Approximately 90% of wall events have a value of $\theta_z > 0.11$ rad. Thus θ_z can be used to identify likely wall events and remove them from the analysis. Figure 6.20 shows an illustration of this cut. In each graph of θ_z versus d_w the bulk events are marked in green and the wall events are marked in red. It can be seen that they belong to two different populations. The cut on θ_z removes most of the wall distribution but keeps the bulk events. The $\theta_z < 0.11$ rad cut, if applied to the entire bulk volume of

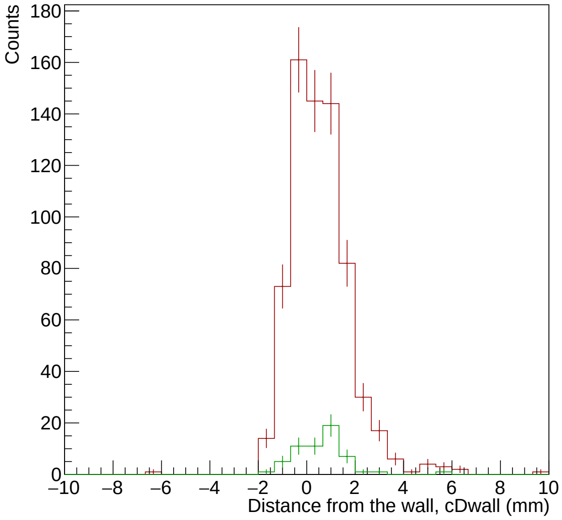

Figure 6.22: Histogram of events near the wall as a function of the distance from the wall (x-axis). The green histogram is with the theta cut and the red one is without. The cut on θ_z reduces the number of wall events, allowing for a larger fiducial zone.

the IV, would impose a penalty on the exposure due to its efficiency. Therefore the application of this cut is restricted to the region near the wall. Other cuts such as the goodness of fit for the track of the bubble and the time-separation of the events (time of detection by the two chosen cameras) are also applied to ensure that this optics analysis is reliable.

6.5.3 Final fiducial definition

The fiducial volume cuts summarized in this section. For the 3.3 keV Seitz threshold the fiducial cuts are the following:

$$\begin{aligned}&(Z < 0 \text{ AND } 5 < d_w < 10 \text{ AND } 0 < \theta_z < 0.12) \text{ OR}\\&(Z \leq 0 \text{ AND } d_w > 10) \text{ OR}\\&(0 < Z < 523 \text{ AND } d_w > 11) \text{ OR}\\&(0 \leq Z < 523 \text{ AND } 4 < d_w < 11 \text{ AND } \theta_z < 0.12\\&\qquad \text{AND } \chi^2(\theta_z) < 20 \text{ AND } \Delta F_{gen} < 10)\end{aligned}$$

For the 2.4 keV Seitz threshold the fiducial cuts are the following:

$(d_w > 5$ AND $Z < 0)$ OR
$(0 < Z < 519$ AND $d_w > 7)$ OR
$(519 < Z < 529$ AND $\Delta F_{gen} < 10$ AND $d_w > 6)$ OR
$(0 < Z < 519$ AND $3 < d_w < 7$ AND $\theta_z < 0.11$ AND $\Delta F_{gen} < 10)$

For the 1.8 keV Seitz threshold the fiducial cuts are the following:

$(d_w > 5$ AND $Z < 0$ AND $\Delta F_{gen} < 10)$ OR
$(0 < Z < 531$ AND $d_w > 10)$ OR
$(0 < Z < 531$ AND $3 < d_w < 10$ AND $\theta_z < 0.21)$

The reconstruction quality cuts applied to events in all thresholds are the following:

$(Q_{cxyz} != 0)$ AND $(Q_{cxyz} != 3)$ AND
NOT $(Q_{cxyz} = 2$ AND $d_w < 10$ AND $\theta_z < 0)$

As a check of the fiducial cuts, the dytran values of events was graphed against the distance from the wall d_w. Checking if any event classified as fiducial is an actual wall event with this variable can be used to determine if the optical analysis is acceptable. Three such graphs were for the three different thresholds are shown in Figure 6.23.

6.5.4 Fiducial mass

The fiducial volume is dependent not only on the fiducial boundaries but also on the optical quality cuts. The strategy here is to define the fiducial volume as total volume multiplied by the efficiency fraction - the idea can be summarized by the concept of an 'equivalent fiducial volume' where the detector is active 100 % of its time in a fiducial volume that has been shrunk by the efficiency factor. For example since $\Delta F_{gen} < 10$ is 99% efficient on actual bulk events it misses real bulk events 1% of the time. Assume that V is the volume between Z=519 mm and Z=529 mm. The ΔF_{gen} cut effectively makes the volume of the active mass between Z=519 mm and Z=529 mm active 99% of the time. This can also be redefined as the volume being 0.99V but active 100 % of the time. This is the 'equivalent fiducial volume'.

The cuts applied are different in different parts of the fiducial volume. So, the total fiducial volume estimation is a sum of all the different pieces

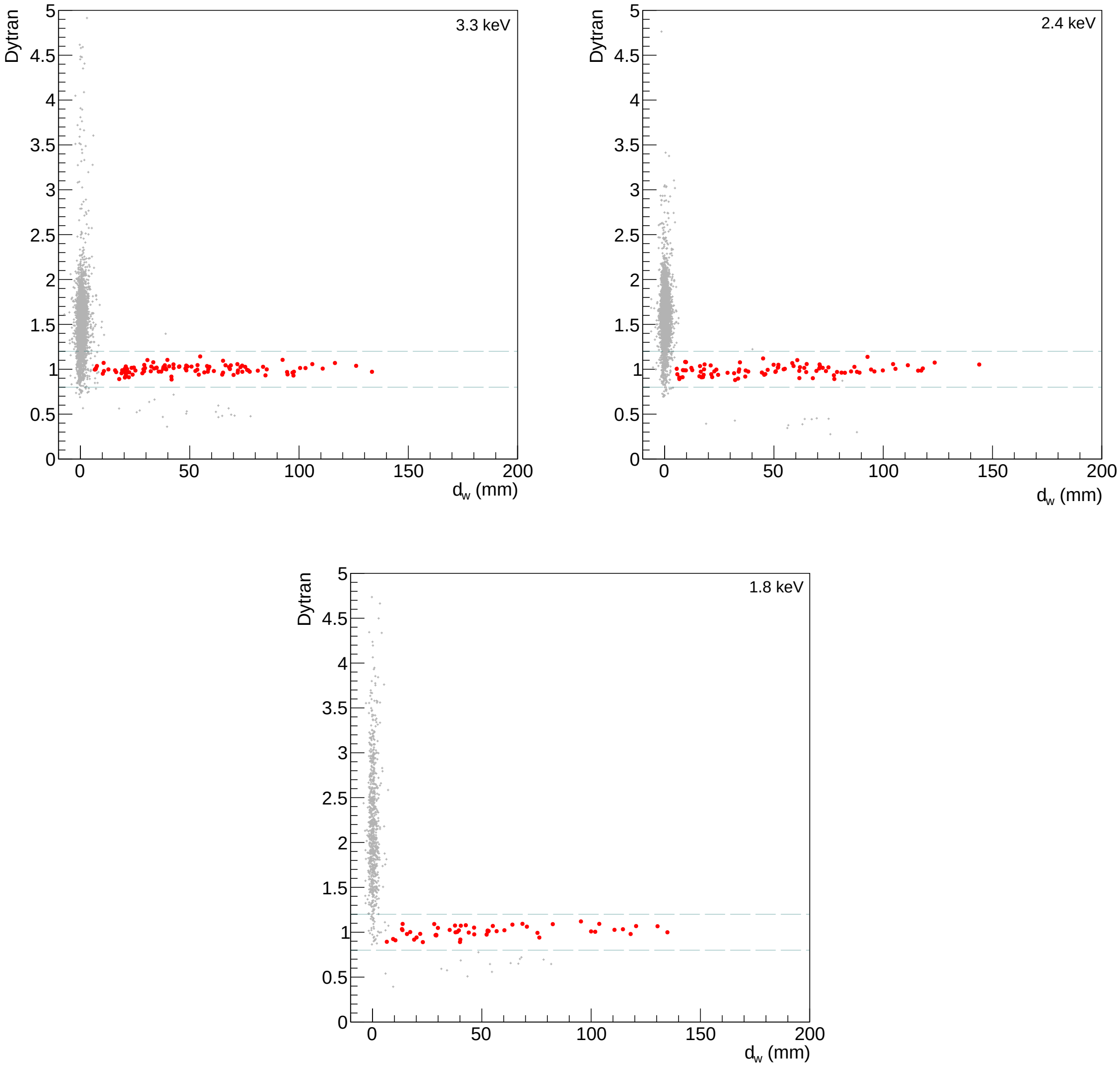

Figure 6.23: Graphs of the Dytran fast pressure excursion parameter against d_w of each single bubble event at the three different thresholds. The red points are the ones classified as fiducial by the optics analysis algorithm.

of fiducial volumes scaled by their appropriate efficiencies determined for the cuts applied on them.

Unless otherwise specified, the efficiency was calculated on bulk single γ calibration events that pass all the data quality cuts for their respective threshold as described in Section 6.6.2 and the single bubble selection cuts as described in Section 6.6.3. The efficiency is defined as the ratio of events that pass the cut that is being considered over the total number of events that the cut is tested on. The construction of the fiducial volume and mass are described under the next three subheadings one for each Seitz threshold:

6.5.4.A Fiducial volume and mass at 3.3 keV (14.05 °C, 30 psi)

The cuts used in the fiducial volume along with their efficiency are summarized here. Each item in the list of cuts is used on different parts of the fiducial volume and are not cumulative.

- ($\boldsymbol{\theta_z < 0.12}$) has an efficiency of 93.68 %.
- ($\boldsymbol{\theta_z < 0.12}$ AND $\boldsymbol{\chi^2(\theta_z) < 10}$ AND $\boldsymbol{\Delta F_{gen} < 10}$) has an efficiency of 91.05 % where $\chi^2(\theta_z)$ is the χ^2 goodness of fit value for the θ_z parameter. The efficiency of $\chi^2(\theta_z)$ and ΔF_{gen} was calculated by taking all calibration and background events in the annulus region where it is applied and counting how many passed the cuts over the total number of events. Only 2 events failed out of 72. The efficiency fraction is then $70/72 = 0.972$. This number multiplied with the efficiency from θ_z gives the 91.05% stated efficiency.

The equivalent fiducial volumes of each section of the fiducial volume definition multiplied with the cut efficiencies are summarized in Table 6.6.

The total fiducial volume at this threshold is then $(34.80 \pm 0.54)\,\mathrm{L}$ and the total fiducial mass is: $(47.82 \pm 0.74)\,\mathrm{kg}$ (92.02% of the active mass in the detector.)

Section of the vessel	Fiducial volume
Cylindrical region above $Z = 0$ ($0 < Z < 523$ AND $d_w > 11$)	$(29.50 \pm 0.45)\,\mathrm{L}$
Annulus region near the wall ($0 < Z < 523$ AND $4 < d_w < 11$ AND $\theta_z < 0.12$ AND $\chi^2(\theta_z) < 20$ AND $\Delta F_{gen} < 10$)	$(2.88 \pm 0.02)\,\mathrm{L}$
Inner spheroidal region ($Z \leq 0$ and $d_W > 10$)	$(2.06 \pm 0.06)\,\mathrm{L}$
Near the walls in the spheroidal region ($Z < 0$ and $5 < d_w < 10$ $0 < \theta_z < 0.12$)	$(0.36 \pm 0.01)\,\mathrm{L}$
Total	$(34.80 \pm 0.54)\,\mathrm{L}$

Table 6.6: The fiducial volume in different parts of the vessel for run BGB33 at 3.3 keV Seitz threshold.

6.5.4.B Fiducial volume and mass at 2.4 keV (16 °C, 30 psi)

The cuts used in the fiducial volume along with their efficiency are summarized here. Each item in the list of cuts is used on different parts of the fiducial volume and are not cumulative.

- $\boldsymbol{\Delta F_{gen} < 10}$ with an efficiency of 99.06 %. The efficiency of ΔF_{gen} was calculated on all calibration and background events in the annulus region (for the cut applied to the annulus region) and the fiducial bulk (for the cut applied to the top region near the surface. Both yielded 99% efficiency. The ΔF_{gen} cut efficiency could not be evaluated solely on the surface since the statistics is too low. (1 event total). The assumption is that the efficiency of the ΔF_{gen} cut does not vary with height. A profile histogram of the efficiency of ΔF_{gen} cut efficiency with height is shown in Figure 6.24 that justifies this assumption.

- $\boldsymbol{\theta_z < 0.11}$ AND $\boldsymbol{\Delta F_{gen} < 10}$ with an efficiency of 86.45% . This was computed by taking the number of events that pass this cut to the total number of events between $60\,\mathrm{mm} < R^2/R_{jar} < 125\,\mathrm{mm}$ where the failure rate of this cut is constant. This is demonstrated by Figure 6.25 showing the constant rate of failures in this region.

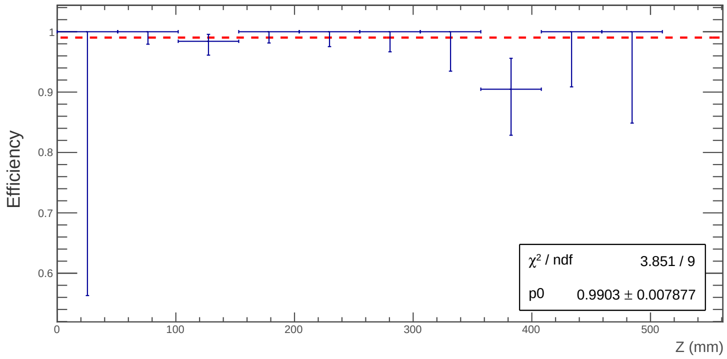

Figure 6.24: The efficiency of ΔF_{gen} over height (Z). It can be seen that the efficiency is consistent in Z.

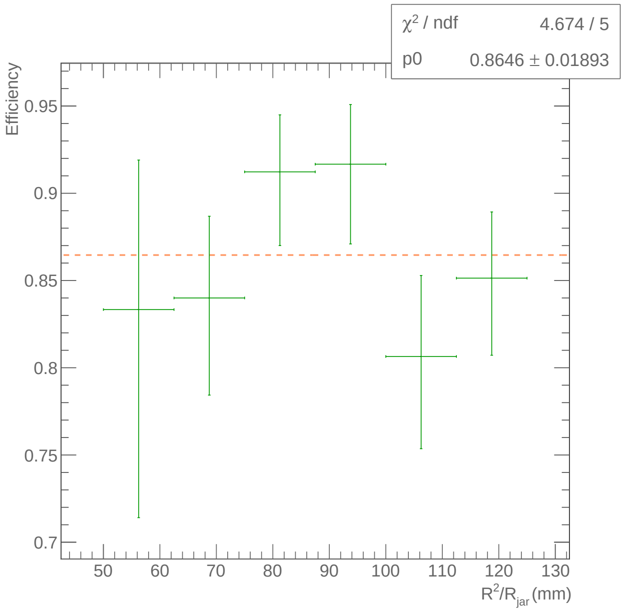

Figure 6.25: The failure rate of θ_z over the range $60\,\mathrm{mm} < R^2/R_{jar} < 125\,\mathrm{mm}$ where it is constant. This range can thus be used to evaluate the efficiency of the cut.

Section of the vessel	Fiducial volume
Cylindrical region above $Z = 0$ $0 < Z < 519$ AND $d_w > 7$	$(31.05 \pm 0.46)\,\mathrm{L}$
Annulus region near the wall $0 < Z < 519$ AND $3 < d_w < 7$ AND $\theta_z < 0.11$ AND $\Delta F_{gen} < 10$)	$(1.68 \pm 0.01)\,\mathrm{L}$
Spheroidal region $d_w > 5$ AND $Z < 0$	$(2.42 \pm 0.07)\,\mathrm{L}$
Interface of C_3F_8 and buffer liquid $519 < Z < 529$ AND $\Delta F_{gen} < 10$ AND $d_w > 6$	$(0.60 \pm 0.06)\,\mathrm{L}$
Total	$(35.75 \pm 0.60)\,\mathrm{L}$

Table 6.7: The fiducial volume in different parts of the vessel for run BGB24 at 2.4 keV Seitz threshold.

The fiducial volume of each section of the fiducial volume definition multiplied with the cut efficiencies are summarized in Table 6.7.

The total fiducial volume is then $(35.75 \pm 0.60)\,\mathrm{L}$ and the total fiducial mass is: $(48.89 \pm 0.82)\,\mathrm{kg}$ (94.08 % of the active mass in the detector). Although the fiducial volume is an imaginary construct and absolute in the context of the experiment, the ability to accurately position the bubble in the fiducial boundary defines the error in the exposure. The error in the fiducial volume is thus be defined using the accuracy of the absolute positioning of the bubble which has an error of ±1 mm.

6.5.4.C Fiducial volume and mass at 1.8 keV (16 °C, 21 psi)

The cuts used in the fiducial volume along with their efficiency are summarized here. Each item in the list of cuts is used on different parts of the fiducial volume and are not cumulative.

- $\boldsymbol{\theta_z < 0.21}$ with an efficiency of 95.62 %
- $\boldsymbol{\Delta F_{gen} < 10}$ with an efficiency of 99.68 %. ΔF_{gen} was again evaluated on bulk γ calibration single events since the statistics was too low in the thin shell region it was applied to.

Section of the vessel	Fiducial volume
Cylindrical region above $Z = 0$ $0 < Z < 531$ AND $d_w > 10$	(30.40 ± 0.46) L
Annulus region near the wall $0 < Z < 531$ AND $3 < d_w < 10$ AND $\theta_z < 0.21$	(3.09 ± 0.03) L
Spheroidal region $d_w > 5$ AND $Z < 0$ AND $\Delta F_{gen} < 10$	(2.05 ± 0.06) L
Total	(35.55 ± 0.54) L

Table 6.8: The fiducial volume in different parts of the vessel for run BGU18 at 1.8 keV Seitz threshold.

The fiducial volume of each section of the fiducial volume definition multiplied with the cut efficiencies are then:

The total fiducial volume is then (35.55 ± 0.54) L and the total fiducial mass is: (48.58 ± 0.74) kg (93.49 % of the active mass in the detector).

6.6 Datasets and livetime selection

Two datasets were acquired at 3.3 keV and 2.4 keV. These were "blinded" for analysis. An additional, shorter, non-blind dataset was acquired at 1.8 keV. A graph of the integrated livetime since the end of the first blinded dark matter search run is shown in Figure 6.26.

6.6.1 Goldenness cuts

Source movements within the environment around the detector were logged and monitored. A "goldenness" variable was defined to remove periods of questionable stability or low-background status for any of the following reasons:

- A run is characterized as entirely "bad" generally due to an extremely low live-fraction.
- A latency period following major disruptions such as a power outage is marked non-golden. A conservative 24 hour latency period was used for the first run of PICO-60 and for the second run this criteria was loosened

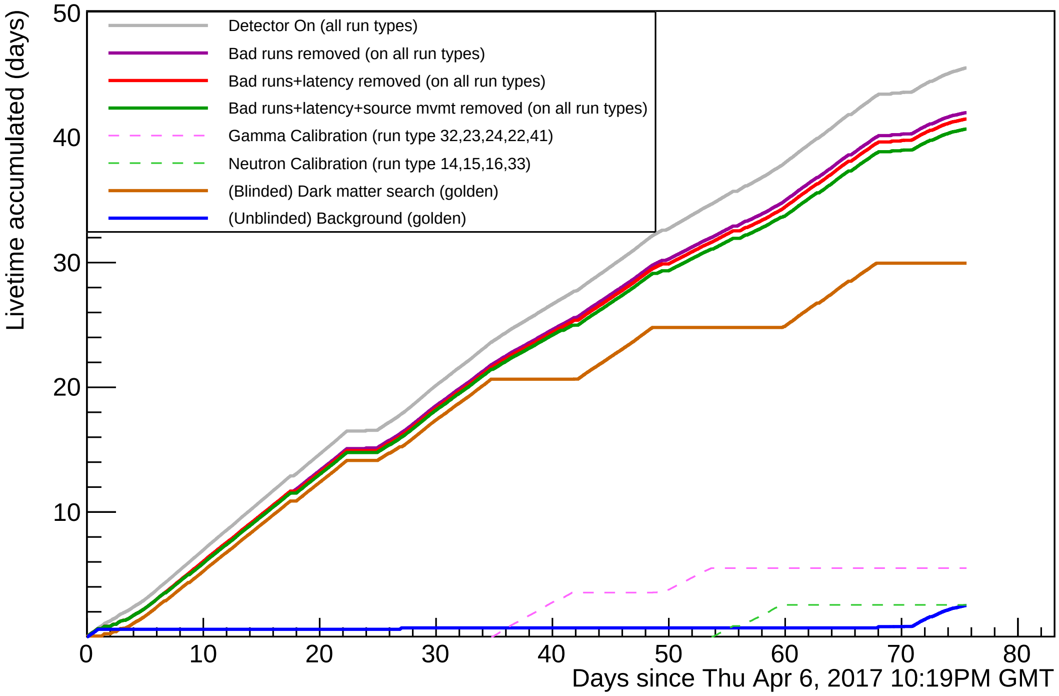

Figure 6.26: The livetime of the detector from when the second blinded dark matter search run started

to 6 hours after it was observed that the original value was needlessly conservative, and in fact no low-AP events occurred during the latency periods.

- A period of 1h was marked non-golden both before and after movements of radioactive sources either by PICO or by other SNOLAB experiments. The time spans 1h before and after the source deployment and again 1h before and after the source removal.

All data analysis excludes periods matching any of the above criteria.

6.6.2 Data quality cuts

This subsection describes the data quality cut to all events before they are considered for processing. A general prescription for all applied cuts is to determine the efficiency of the cut on calibration or unblind background data as appropriate and scale the total exposure of the dark matter search to the efficiency found in this manner. The applied data quality cuts and their efficiencies are listed in Table 6.9. The descriptions of these cuts are outlined below.

6.6.2.A Base event selection cuts

The “base cut” refers to the cuts required to get a valid set of data. The cuts applied are

- The time since the expansion of the chamber (called “expansion time” or t_e) has to be large enough for the detector to be in a stable operational state $t_e > 25s$.

- Exclusion of commissioning or test runs. These runs are collectively known as “engineering runs”. They are performed after commissioning new hardware and testing hardware upgrades.

- Goldenness cut.

- Removal of timeouts (Section 4.6). The timeout events remain in the calculation of the exposure.

Temperature and pressure cuts to select data at a certain Seitz threshold are also applied in this step. These cuts, along with the Seitz threshold condition they represent, are given below.

- 14 °C, 30 psi (3.3 keV Seitz threshold): Data set: BGB33
- 16 °C, 30 psi (2.4 keV Seitz threshold): Data set: BGB24
- 16 °C, 21 psi (1.8 keV Seitz threshold): Data set: BGU18

6.6.2.B Data written successfully with no DAQ errors

Occasionally there were events where a fault with the DAQ system would result in incomplete data being collected. Cuts are applied to remove such events.

6.6.2.C Video triggers

The three trigger types possible are those issued by the cameras, pressure spike triggers when the cameras do not “see” anything yet pressure rises sharply, and timeouts. Only the first kind are considered valid data.

6.6.2.D Pressure in tolerance range

This is a cut that determines if the pressure in the chamber just before the bubble forms is within 1 psi from the set point. At 1.8 keV run condition, the detector could not maintain a stable pressure of 21±1 psi for a certain fraction of the time leading to a 4.4% efficiency loss. The reason for not being able to maintain the pressure within the tolerance is that this run condition is at the edge of the design limit of the detector.

6.6.2.E Efficiencies of the data quality cuts

	Cut and its description	Number of events and/or percent efficiency		
		3.3 keV	2.4 keV	1.8keV
1	Base cut (6.6.2.A)	11408	9012	6123
2	No DAQ errors (6.6.2.B)	11408 [100^{+0}_{-0}%]	9011 [100^{+0}_{-0}%]	6123 [100^{+0}_{-0}%]
3	Video trigger (6.6.2.C)	11406 [100^{+0}_{-0}%]	9011 [100^{+0}_{-0}%]	6123 [100^{+0}_{-0}%]
4	Pressure within tolerance (6.6.2.D)	11405 [100^{+0}_{-0}%]	9004 [99.9^{+0}_{-0}%]	5854 [$95.6^{+0.3}_{-0.3}$%]
	Total	100^{+0}_{-0}%	99.9^{+0}_{-0}%	$95.6^{+0.3}_{-0.3}$%

Table 6.9: Base quality cuts that are applied before any analysis can be performed. The events passing step 4 are used for further analysis.

6.6.3 Single bubble selection cuts

To select single bubble events for the dark matter search analysis of this chapter, and the alpha particle analysis of Chapter 7, optical single bubble classification N_{bub} (variable `nbub`) and Dytran variable were used. Evaluating the efficiency of the single bubble selection requires the assumption that all bulk events created by a gamma interaction are single bubble events. This assumption is made based on the fact that only neutrons can produce multiple bubble events. The number of neutrons expected in the detector fiducial volume is much less than 1 for the combined livetime accumulated with the γ calibration runs and unblind background runs. The strategy is to compare these events with those classified as single bubble events by the video analysis and the Dytran parameter.

The description of each of these cuts are described here.

6.6.3.A Gamma calibration and background event data

All events in gamma calibration runs with run types 22, 23, 24, 32 (^{133}Ba calibration), 41 (^{60}Co calibration) and 0 (unblind background) data were selected for analysis. The events selected also passed all the data quality cuts for their respective threshold as described in Section 6.6.2.

6.6.3.B Fiducialized background and gamma calibration data

The fiducial volume definitions summarized in Section 6.5.3 were used to select the events in gamma calibration and background runs from Section 6.6.3.A. The number of events selected in this step will be compared to the ones tagged as single bubble event by the video and the fast pressure analysis.

6.6.3.C Singles by optics

In this set, the events that were selected in Section 6.6.3.B were compared with the results from the optical analysis. The variable N_{bub}, calculated by cXYZ, is used by the optics analysis to tag the number of bubbles in an event. The result of the cut $N_{bub} = 1$ shows how many such events were tagged correctly and the percentage shows the efficiency by comparing the number correctly tagged with the total number from Section 6.6.3.B.

6.6.3.D Singles by fast pressure excursion (Dytran)

In this set the number of events selected in Section 6.6.3.B are compared to the results from the fast pressure excursion (Dytran) analysis. The Dytran variable is used to determine whether the event has a single bubble using the cut $0.8 < Dytran < 1.2$. The result of the cut shows how many such events are tagged correctly.

6.6.3.E Efficiencies of the single bubble selection cuts

The efficiency of these cuts for the three thresholds under consideration (Section 6.6.3.A to 6.6.3.D) are shown in Table 6.10.

	Cut and its description	Number of events and/or percent efficiency		
		3.3 keV	2.4 keV	1.8keV
5	All γ calibration or background data (6.6.3.A)	3329	2551	2900
6	Fiducial γ or background events (6.6.3.B)	298	861	1091
7	Singles by optics (6.6.3.C)	298 [100^{+0}_{-0}%]	861 [$100^{+0}_{-0.1}$%]	1091 [100^{+0}_{-0}%]
8	Singles by dytran (6.6.3.D)	295 [$99^{+0.5}_{-0.7}$%]	850 [$98.7^{+0.3}_{-0.4}$%]	1064 [$97.5^{+0.4}_{-0.5}$%]

Table 6.10: Efficiency of the optics (N_{bub},) and fast pressure excursion (Dytran) analysis for identifying single bubbles. It is assumed that the bulk events caused by a γ particle are a single bubble event. The efficiency is then measured by the number of such events correctly classified by the cuts.

6.6.4 Nuclear recoil event selection cuts

For the final dark matter search analysis the acoustic information contained in the events needs to be used to discriminate alpha events from nuclear recoils. In this section the cuts used to identify nuclear recoils are described and their efficiency evaluated. The variable that is used to discriminate between alpha events and nuclear recoils is the acoustic parameter or AP. The strategy to measure the efficiency of AP is to select all fiducial single bulk events in neutron and gamma calibration runs and check if they are classified as nuclear recoil events. It is expected that some alpha particles will be in this dataset but the number is small for these calibration runs therefore the expectation of alpha contamination is about 3±1 events per live day.

6.6.4.A Acoustic quality cuts

Acoustic quality cuts are used to maintain a baseline quality of the acoustic data processing. The acoustic quality variables were applied to all the bulk single gamma calibration events, as described in Section 6.6.3.D, for testing their efficiency. This was determined by the number of events that passed the cut.

6.6.4.B Event selection for AP efficiency determintion

To determine the efficiency of the AP selection all fiducial single events as determined by the Dytran variable and optics in the γ and neutron calibration runs for the datasets with 1.8 and 2.4 keV Seitz threshold, were selected. The gamma rejection at 3.3 keV Seitz threshold was on the order of 10^{-11}, so for this dataset only neutron calibration events are available.

6.6.4.C AP cuts

In Figure 6.27, all calibration and background events described in Section 6.6.4.B from each threshold are shown. Scaling factors of 1.34 and 9 are used on the AP of events in the 2.4 keV and 1.8 keV datasets, respectively, to move the neutron peak to an log(AP) value of 0. Also shown are the AP cuts for each threshold. The recoil distribution from combined neutron and gamma calibration is well fit by a gaussian in ln(AP), and the acceptance band is set from $\mu - 3\sigma$ to $\mu + 2\sigma$.

6.6.4.D Determining the efficiency of the AP cut

The efficiency of the cut may be determined in two different ways. One such method is to fit the distribution of the acoustic power with a Gaussian and take the ratio of the area under the gaussian but in the limits of the cut over the total area of the Gaussian. Method two is to take the absolute number of entries that are in such a distribution between the two cuts over the total number of events that lie below the cutoff for alpha particles. Both methods should yield similar results within the statistical uncertainties.

6.6.4.E Nuclear recoil event selection efficiencies

Table 6.11 presents a summary of nuclear recoil event selection cuts and efficiencies.

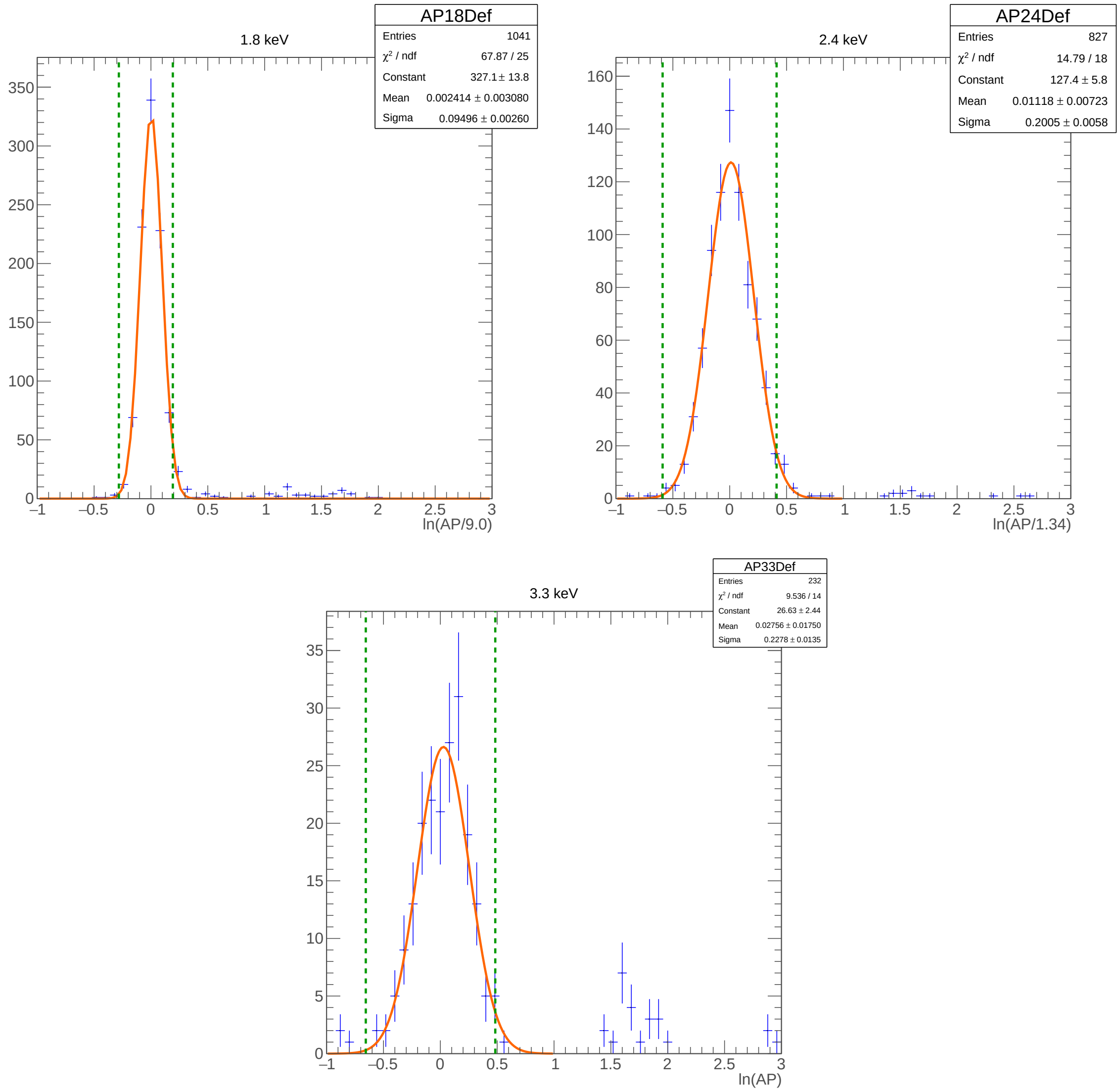

Figure 6.27: APs cut for the data in all three thresholds using both neutron and gamma calibration data, based on parameters of a gaussian fit to the low-AP peak, with boundaries of $\mu - 3\sigma$ and $\mu + 2\sigma$. For the 1.8 keV and 2.4 keV datasets, gamma calibration data are used to show the low-AP recoil band, while the 3.3 keV data set uses neutron calibration.

	Cut and its description	Number of events and/or percent efficiency		
		3.3 keV	2.4 keV	1.8keV
9	Acoustic quality (6.6.4.A)	287 [$97.3^{+0.8}_{-1.1}\%$]	838 [$98.6^{+0.4}_{-0.4}\%$]	1038 [$97.6^{+0.4}_{-0.5}\%$]
10	Event selection for AP efficiency (6.6.4.B)	351	934	1325
11	AP - Method 1 (6.6.4.D)	$95.9^{+0.0}_{-7.3}\%$	$97.4^{+1.6}_{-3.2}\%$	$100^{+0}_{-2}\%$
11	AP - Method 2 (6.6.4.D)	$93.2^{+1.3}_{-1.5}\%$	$96.2^{+0.6}_{-0.7}\%$	$95.0^{+0.6}_{-0.6}\%$

Table 6.11: Efficiency of the acoustic power in determining if an event is a nuclear recoil.

6.6.5 Combined WIMP search efficiency

For selecting WIMP search candidates, data quality (Section 6.6.2), single event selection (Section 6.6.3), fiducial volume selection (Section 6.5.3) and nuclear recoil selection cuts (Section 6.6.4) are combined. The combined efficiency, the exposure and the number of candidate events in each dataset is summarized in Table 6.12.

Seitz threshold (pressure and temperature)	Total efficiency	Fiducial mass	Livetime (live-days)	Exposure (kg·days)	Candidate events
$(3.30 \pm 0.05)\,\mathrm{keV}$ (14.05°C, 30psi)	92.3%	47.82 kg	29.96	1322.37	108
$(2.41 \pm 0.01)\,\mathrm{keV}$ (16°C, 30psi)	95.9%	48.89 kg	29.95	1404.22	87
$(1.8 \pm 00.7)\,\mathrm{keV}$ (16°C, 21psi)	90.88%	48.58 kg	7.04	310.81	52

Table 6.12: Summary of the single bubble selection efficiency, fiducial mass, livetime and exposure to WIMPs for each of the three thresholds at which the PICO-60 experiment conducted a search for dark matter. The numbers presented for the 3.3 keV dataset are from the the updated analysis described in this thesis.

The methods and cuts developed in this chapter are used in the analysis of α particles in Chapter 7, the analysis of the bubble growth and motion in Chapter 8, and the analysis of dark matter search data in Chapter 9.

Chapter 7

Alpha particles observed in PICO-60

The majority of events acquired in the PICO-60 experiment are calibration γ particles or calibration neutrons. However a large fraction of the events in the detector are alpha particles that are emitted by the decay of radon and its daughters in the active liquid. These alpha particles are quite interesting by themselves and are studied in this chapter. PICO uses the acoustic information to discriminate between alpha particles and neutrons but the model of the acoustic emission is incomplete. Studying the alpha particles and their acoustic emission allows for more knowledge to be gained about the origin of the acoustic signal. This chapter is a summary of the properties of the alpha particles observed in the PICO-60 experiment. It should be noted that the six out of eight piezo-electric sensors failed in PICO-60, reducing the quality of the acoustic information available.

7.1 Selection of events

To study the alpha particle interactions it is necessary to select a pure sample of alpha events in the fiducial volume of the detector. The base cuts described in Chapter 6 were applied, but the cuts to select recoil events were altered. The cuts used to select a pure set of alpha events are described here.

- log(AP)>1: AP is the main parameter to discriminate neutrons from alphas. Normally one selects events with $0.5 < AP < 1.5$ at 3.3 keV threshold to select a sample of neutrons but the same parameter can be used to select alphas by choosing a cut value with minimal risk of leakage from neutrons.

AP is somewhat dependent on temperature and pressure, so the value of the AP cut varies in the three different datasets. It was observed that AP scaling is a nonlinear phenomenon, and thus the cutoff points to demarcate alphas from neutrons were heuristically determined from a histogram of the AP of the calibration data superimposed on background data. The α events have AP>2 for 2.4 keV and AP>18 for 1.8 keV threshold data.

- Fiducial volume cut: The fiducial cuts used for dark matter searches as defined in Chapter 6 are used for this study. Events on the wall of the detector (wall events) have a value of AP that is between that of single bulk nuclear recoil events and alpha events. The distribution of AP of these wall events overlaps with the one for the nuclear recoil and the alpha events in the fiducial volume. Thus it is important to reject wall events when performing an analysis of alpha particles in the bulk.

- Run type selection: For 14.05 °C, 30 psi data (3.3 keV Seitz threshold) run types 0 (background), 2 (AmBe neutron calibration), 10 (dark matter search), 14, 15 (Cf-252 neutron calibration), 21 and 22 (Ba-133 γ calibration) were used to maximize statistics. For the 16 °C, 21 psi data (1.8keV Seitz threshold) only background runs were used and for the 16 °C, 30 psi data (2.4 keV Seitz threshold) run types of 0 (background), 100 (dark matter search), 21 and 22 (gamma calibration) runs were used.

- Single bubble selection with dytran: $0.8 <\text{Dytran}< 1.2$ was used to select single bubble events along with optical single event criterion (nbub=1).

7.2 Acoustic characteristics at 3.3 keV

The AP distribution of all the events in the detector from the AmBe and ^{252}Cf sources and background runs in the 14.05 °C and 30 psi is plotted in Figure 7.1.

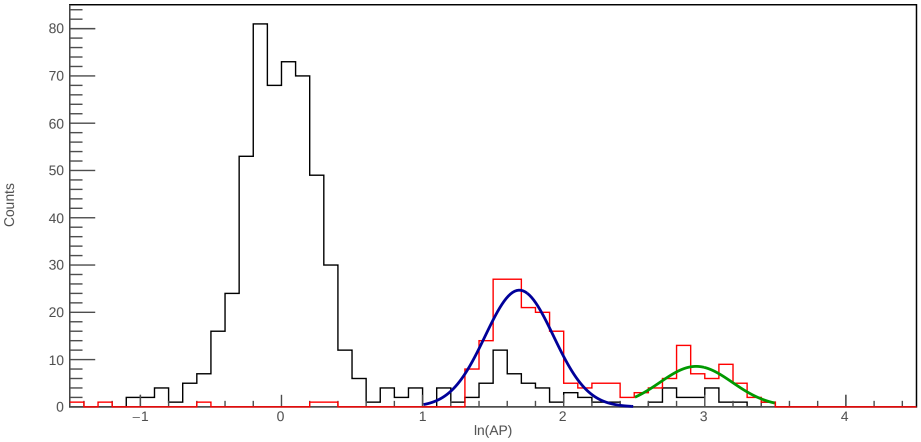

Figure 7.1: AP distribution of all events in the 3.3 keV dataset. The black histogram shows all events in the source run. The red histogram contains events from background and physics runs. The two alpha peaks were fitted with a gaussian.

The alpha events in the plot have three distinct populations at around 0, 1.7 and 2.9 in log(AP). The population at log(AP)=0 are neutron recoils, while the other two are from alphas. The two populations were fitted with Gaussians. The mean and sigma were μ_1=1.68±0.02 with σ_1=0.24 and μ_2=2.93±0.04 with σ_2=0.26. It is interesting in itself that the alpha particles form two peaks in this distribution. It is possible to study if the energy of the emitted alpha particle is correlated to the AP by identifying specific decays. Alphas as a part of the $^{222}\mathrm{Rn}\xrightarrow{\alpha}{}^{218}\mathrm{Po}\xrightarrow{\alpha}{}^{214}\mathrm{Pb}\rightsquigarrow{}^{214}\mathrm{Po}\xrightarrow{\alpha}{}^{210}\mathrm{Pb}$ decay chain (triplets - for the three alpha particles emitted in the chain) arising from decay of ^{238}U may be identified using timing correlations.

There are 216 entries in the background runs, and 274 alphas as defined by log(AP)>1.0 in both types of runs combined in the 3.3 keV data. The data can be used for timing studies to explore the presence of Uranium decay chain alpha particles using the timing signature of alpha events. A histogram of the difference of the time (δ_t) between each alpha event and the previous one in time is made. The histogram is shown in Figure 7.2. It can be noted that the lifetime of the $^{222}\mathrm{Rn}\xrightarrow{\alpha}{}^{218}\mathrm{Po}$ and the $^{218}\mathrm{Po}\xrightarrow{\alpha}{}^{214}\mathrm{Pb}$ decay (the first

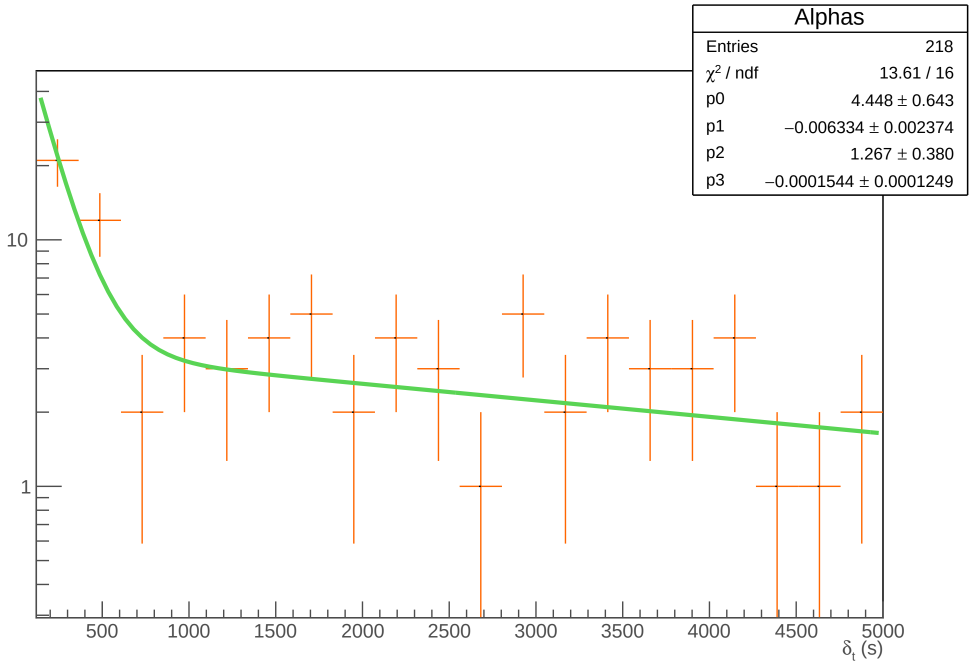

Figure 7.2: Histogram of all δ_t between consecutive events in the 3.3 keV data showing the presence of two different populations of alpha events. The data has been fitted with $p_0 e^{p_1 t} + p_2 e^{p_3 t}$ to determine the two different time scales.

and the second alpha in the chain) is 3.1 min, while the lifetime between the $^{218}\text{Po}\xrightarrow{\alpha}{}^{214}\text{Pb}$ and the ^{214}Po to $\xrightarrow{\alpha}{}^{210}$Pb (second and third alpha in the chain) is 46.7 minutes.

In a histogram of time differences, two distinct time constants can be seen at 166±53s and 6024±3111s. Although low in statistics, these values are the correct order of magnitude for the radon chain where 95% of ^{222}Rn and ^{214}Po decays occur less than 13 minutes apart, and 95% of ^{218}Po and ^{214}Po occur less than 157 minutes apart. The lack of exact agreement arises from low statistics and the fact that the detector compresses for 3 minutes after every event and for 10 minutes after every 10th event so any decay producing an alpha particle during this time is not captured.

Radon triplets can be evaluated in the data. To do this consecutive alpha pairs from the histogram in Figure 7.2 are taken and classified as belonging to the “short pairs" or the “long pairs" based on whether they are separated by less than 13 minutes or less than 157 minutes apart. Matches between the two

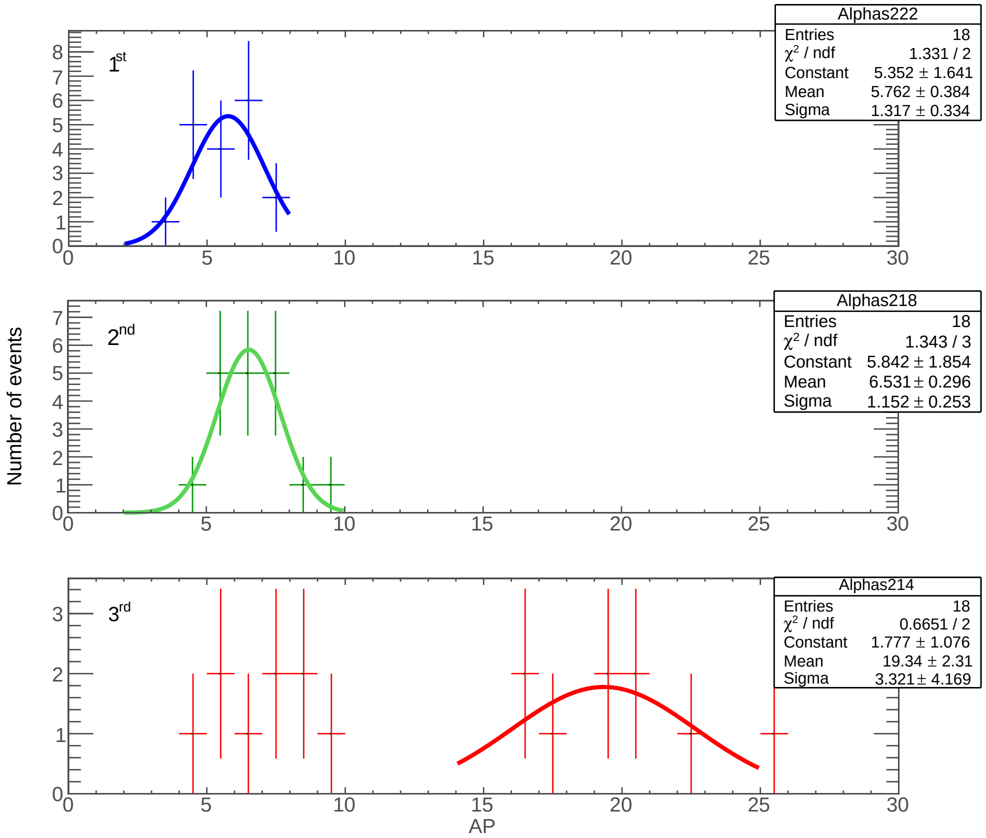

Figure 7.3: Histograms of APs of 3.3 keV Seitz threshold alpha triplets in the 14.05 °C, 30 psi data.

sets of alpha event pairs were made by looking if any of the second events in the short pairs is the first event in a long pair. The matched triplets can then be studied.

A total of 24 such triplets were found in the 3.3 keV data set consisting of background, physics and calibration datasets. Twelve such events were found in the blinded physics run. Histograms of the AP of the 1^{st}, 2^{nd} and 3^{rd} alpha in each triplet were then plotted in Figure 7.3, and fitted to gaussian distributions. Note: for the third alpha, there were two populations observed. This is due to leakage in the sample due to the method of classifying the alphas. The low AP population of the third alpha can be taken as impurity in the sample and were thus ignored in the Gaussian fit.

From this plot, a three point calibration can be performed for alpha energy with AP. ^{222}Rn decay produces a 5.5 MeV alpha, ^{218}Po decay produces a 6.0 MeV alpha, and ^{214}Po decay produces a 7.7 MeV alpha. A graph of the alpha energy versus AP is shown in Figure 7.4 with the error bars being the width of the Gaussians. The calibration extracted from this fit is

$$\log(\mathrm{AP}) = 0.562E_{\alpha} - 1.515 \tag{7.1}$$

where E_{α} is the alpha particle energy. This relationship shows that higher energy alpha particles have a higher acoustic emission that can be explained if higher energy alphas produce more proto-bubbles. Fitting log(AP)=0 (the AP of nuclear recoil events) in this equation gives $E_{\alpha} = 2.7\,\mathrm{MeV}$. This is the energy of an α particle to produce the same acoustic energy as a neutron in the detector. Therefore an α particle with $E_{\alpha} < 3.5\,\mathrm{MeV}$ cannot be resolved from neutrons. This number is derived by calculating the α energy of an event with an AP 2σ away from the mean of neutron events in the 3.3 keV data. Below this energy the α particle track does not seem to nucleate a bubble but the daughter nuclear recoil track does. This result appears to be consistent with the model of sound generation described in Section 3.5. This feature of the PICO bubble chamber potentially opens up an application of superheated liquids in spatially resolving α-spectrometers.

7.3 Acoustic characteristics at 2.4 and 1.8 keV

No large exposure of background runs was collected at the lower Seitz thresholds. Using the same technique as described in Section 7.2, three alpha triplets were isolated at 1.8 keV. The AP of these events is shown in Figure 7.5. Firm conclusions cannot be drawn based on this statistics.

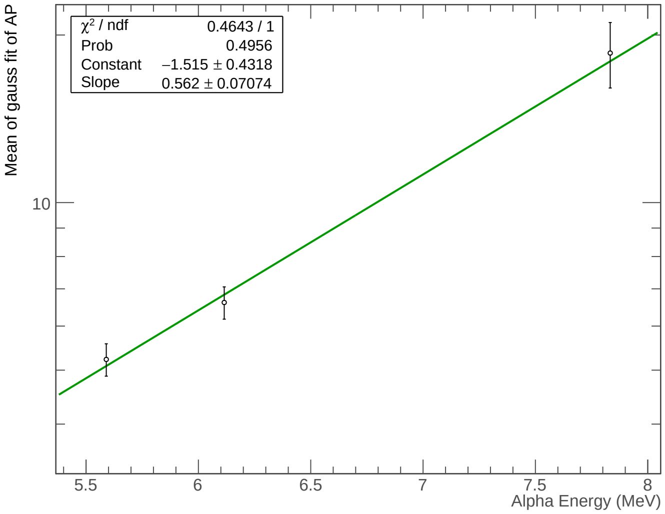

Figure 7.4: Three point calibration for alphas with ln(AP) for 3.3 keV data.

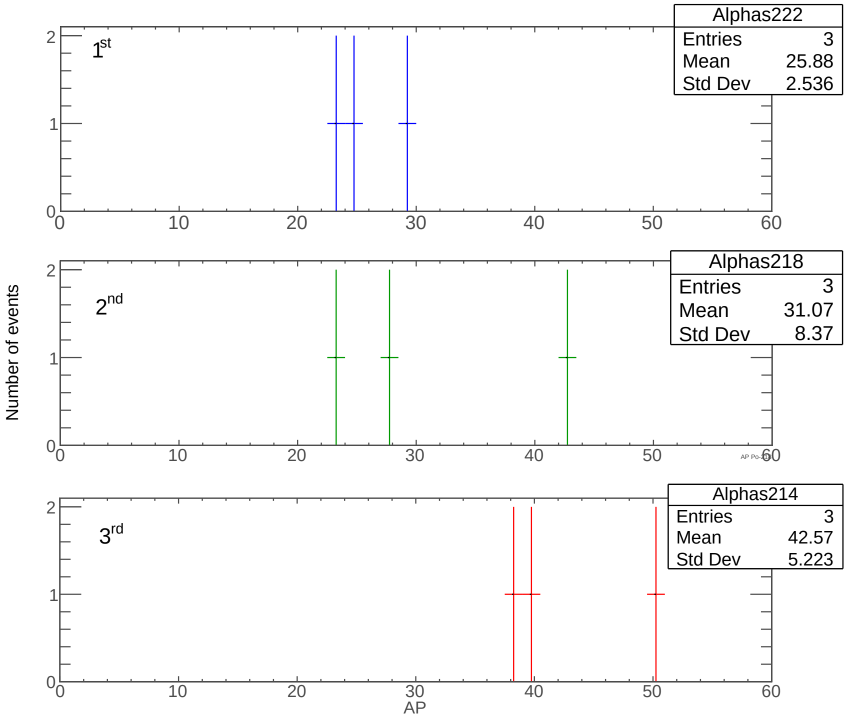

Figure 7.5: Histogram of APs of the alpha triplets at 1.8 keV Seitz threshold.

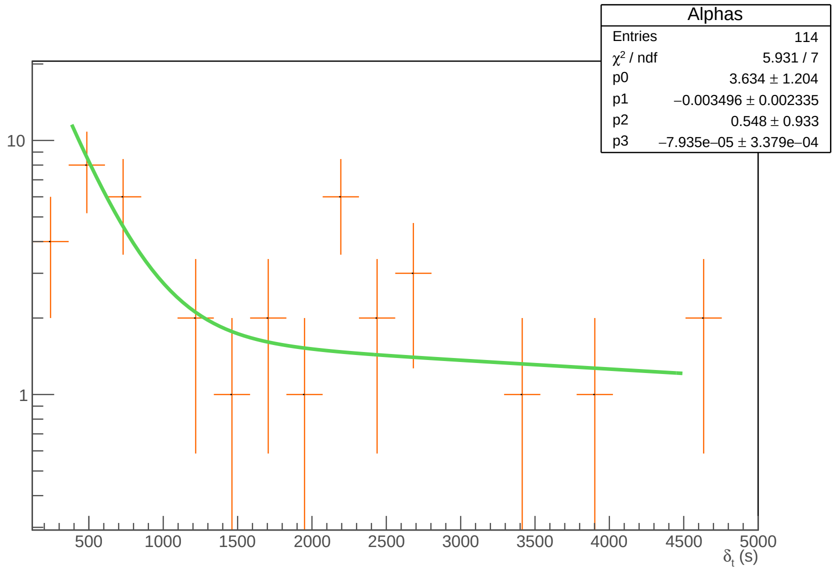

Figure 7.6: Timing correlations of alpha events from the 2.4 keV dataset showing the presence of two populations of alpha events. The fit function is $p_0 e^{p_1 t} + p_2 e^{p_3 t}$.

Looking at the 2.4 keV dataset most of the events that conform to a triplet come from the blinded dark matter search data. Following the prescription set out in Section 7.2 their timing correlation is shown in Figure 7.6. The presence of two different time scales can be seen even though the data is sparse. The AP of the triplets were graphed once again and are shown in Figure 7.7. It is to be noted that the AP of the alpha particles in 2.4 keV data did not scale with the same constant as the neutrons and gammas with respect to the 3.3 keV data.

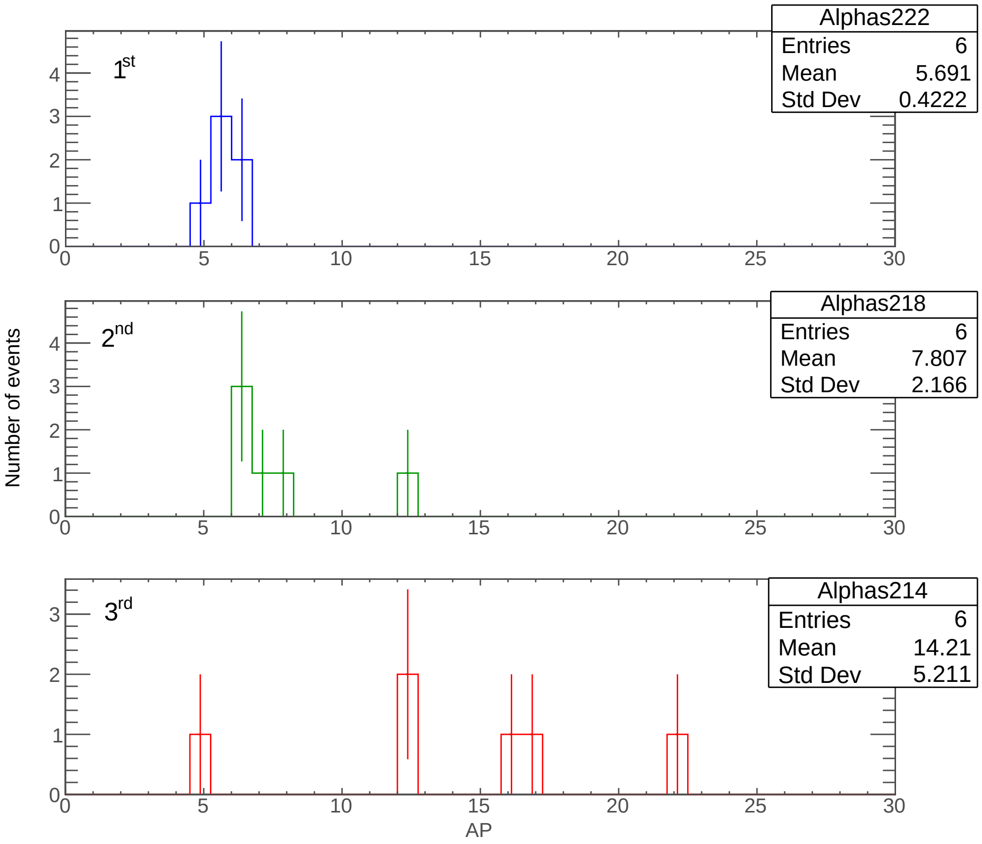

Figure 7.7: Histogram of APs of the alpha triplets at 2.4 keV Seitz threshold.

Chapter 8

Bubble growth and dynamics

The new position reconstruction algorithm consisting of AutoBub and cXYZ (described in Chapter 6) makes it possible to study the growth of a bubble after its genesis and to track its trajectory. This tracking was used to discriminate between bubbles that arise in the fiducial volume from ones that arise from, or near, the vessel wall. Studying bubble growth at such timing resolution in a bubble chamber presents a unique opportunity to gather information about the thermodynamic properties associated with the bubble growth. Determination of the temperature and pressure inside the inner vessel, which is otherwise impossible to directly instrument, is a future scope of work that directly follows the studies presented in this chapter.

It is prudent to divide the detector into sections based on proximity to a heat source or sink, and study each section separately. The viewports can function as a heat source due to the cameras and LEDs. Based on the location of a viewport, the detector is divided into four quadrants. Seen from the top on the X-Y plane, the sections are defined by the angle in this plane, ϕ. Figure 8.1 provides a visualization of the quadrants on the X-Y plane. The bounds for ϕ for the four sections are

- **Nearest to the camera with LEDs:** ϕ = [-3π/4, -π/4]
- **Furthest from the camera with LEDs:** ϕ = [π/4, 3π/4]
- **The two sides with respect to the viewports:** ϕ = [-π/4, π/4] and [3π/4, -3π/4]

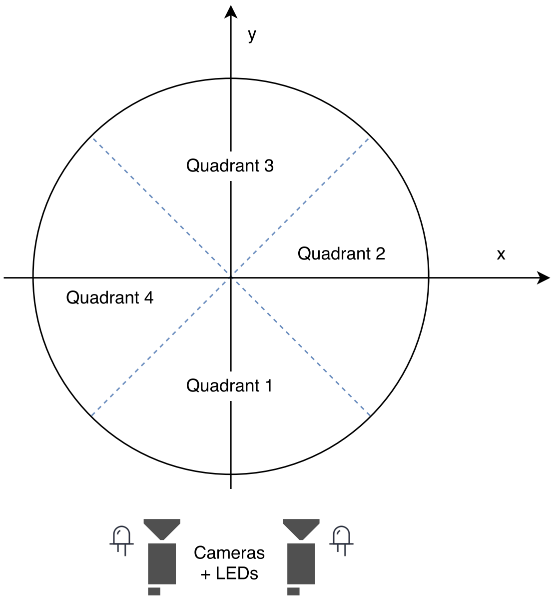

Figure 8.1: Top view of the vessel divided into four quadrants based on the proximity of the viewports and LEDs. Quadrant 1 is the nearest to the viewports and quadrant 3 is the furthest. The x and y axes labelled here are those used by cXYZ of Chapter 6.

8.1 Growth model

The time resolution of the imaging data is 340 Hz. Therefore the time difference between each frame is 2.9 ms. At this time-scale the bubble growth is in the thermal growth regime (Section 3.4). In this regime the growth is isothermal and driven by the heat of the surrounding liquid entering the bubble through the diffusion barrier defining the edge of the bubble. It is modelled by the equation [74, 95]

$$\frac{dR}{dt} = \left[\frac{3}{\pi}\right] \frac{k}{L\rho_v} \frac{T - T_b}{(Dt)^{1/2}}, \tag{8.1}$$

where k is the liquid thermal conductivity, L is the latent heat, D is thermal diffusivity, T is the temperature of the liquid far away from the bubble, T_b is the temperature inside the bubble, and ρ_v is the density of the gas inside the bubble. This is the derivative form of the equation but for practical measurements the integral form is required, which is given by

$$R = \frac{6k}{\pi L \rho_v \sqrt{D}}(T - T_b)(\sqrt{t} - \sqrt{t_0}). \tag{8.2}$$

8.2 Fitting the growth to the model

The time evolution of the size of bubbles within PICO-60 can be fitted to Equation 8.2. Graphs showing the time evolution of several bubbles selected randomly at 16 °C, 30 psi are shown in Figure 8.2. The last two points are not fitted since the bubble is no longer spherical at that point due to its motion. The constants k, L, ρ_v and D can be found from tables [81] or from the REFPROPS database [80].

To test if the theory predicts data accurately, a dataset must be chosen. This dataset was comprised of bubbles in background runs. These have the most separation in time between events, and the detector is more likely to be in thermal equilibrium in this dataset than any of the other ones. Here, background runs include all dark matter search runs unless stated otherwise.

Returning to the fitting function $y = a(\sqrt{t + t_0})$, it can be seen that parameter a measures the rate of the growth and can be used to determine how fast or slow a bubble grows. This is called the growth factor. It is expected that bubbles should grow faster with a decrease in pressure since T_b drops with pressure.

Section 8.3.2 will show that anomalies are seen in the growth rates of the bubbles that are closest to the viewports. Conversely, bubbles in quadrant 3 are less likely to be affected by a heat source or sink and are chosen for the following studies.

8.3 Growth rate versus pressure

It is expected that the growth rate will vary with pressure since the degree of superheat, $T - T_b$, varies with pressure. There is a pressure differential of approximately 1 psi between the top and bottom of the jar. This study uses

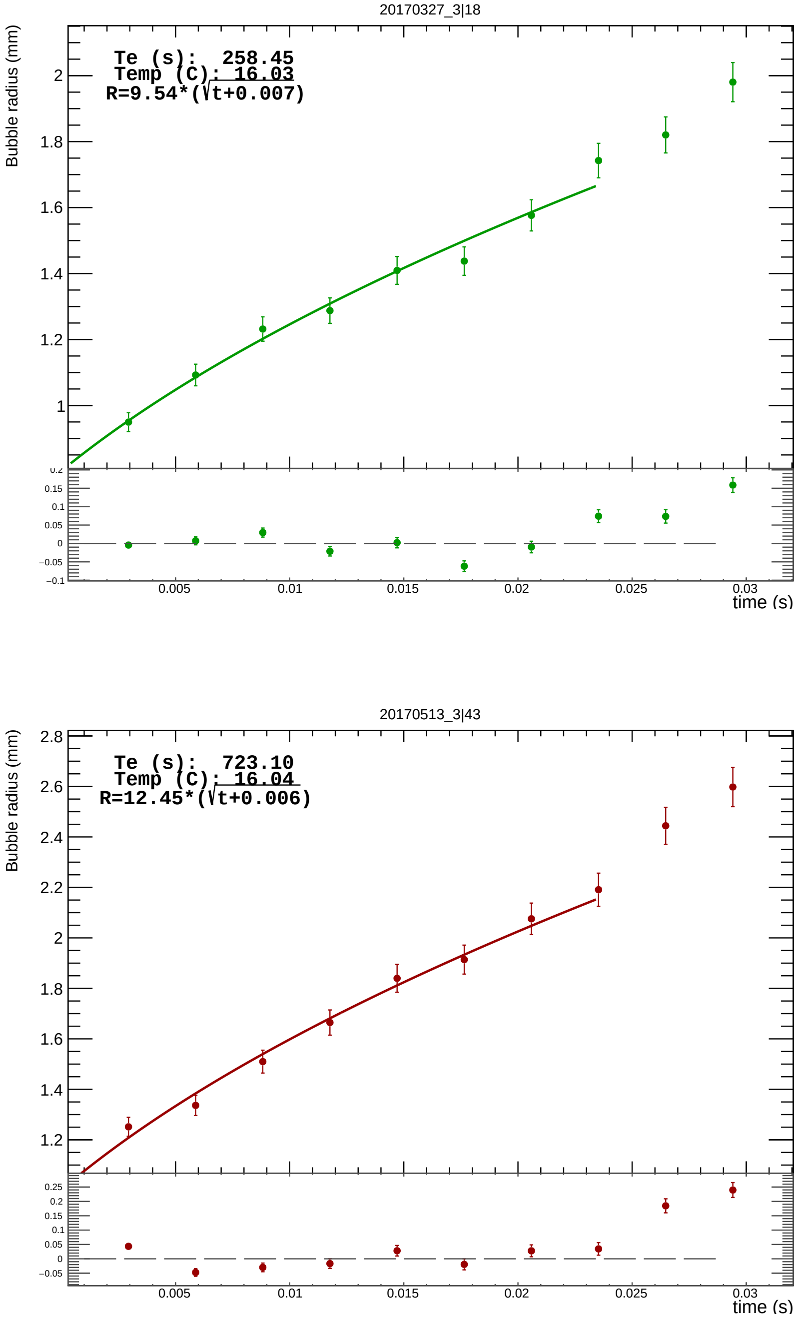

Figure 8.2: The time evolution of the radius of two selected bubbles fitted to Equation 8.2. The lower graph is opposite to the cameras and the LEDs the upper graph on the side that is nearer.

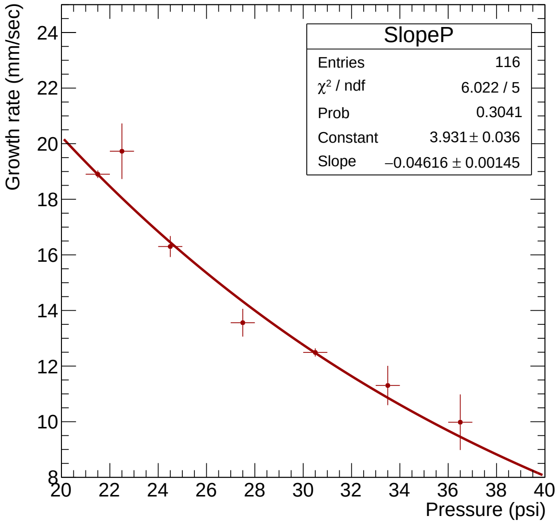

Figure 8.3: The profile histogram of the bubble growth rate a with varying pressure. The data is fitted to the function y=ae^{bx}.

several different runs taken at different pressures but the same temperature (16 °C).

8.3.1 Between runs with same temperature

A small section of the detector between Z=200-300 mm is chosen and the bubble growth rate a is plotted against pressure; see Figure 8.3. The data is fitted to the function $y = ae^{bx}$ where x is the pressure. The data fits the model and the growth rate increases with decreasing pressures.

8.3.2 Pressure differential with height

There is a pressure differential of 1 psi between the top and bottom of the IV related via $h\rho g$; where h is the height, ρ is the density and g is the acceleration due to gravity. An assumption can be made that thermal fluctuations do not cause an appreciable change in the density of the liquid or temperature in a large fraction of the detector. The rate of growth with the liquid head would then increase with increasing Z position $\propto h$. The growth rate as a function of the height is shown in Figure 8.4. The effect of the growth rate

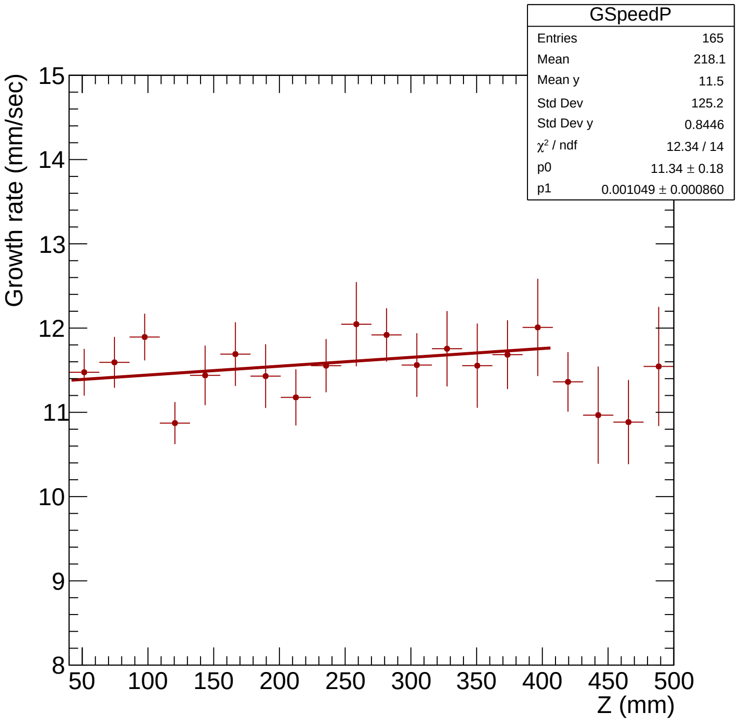

Figure 8.4: The bubble growth rate, a, as a function of height in quadrant 3. The data is fitted to the function y=$p_0 h$.

with height is small compared to the errors so the data is inconclusive. Near the surface boundary (above Z $\simeq$ 350mm), convection and flows cause systematic uncertainties in the growth rate determination (see Section 8.5, and thus the fit was not performed in this region.

The previous sections were described with the events in quadrant 3, far from the LEDs, unless otherwise mentioned. The LEDs near quadrant 1 can exert significant influence on the growth rate of the bubbles since it can act as a thermal source. Figure 8.5 shows a profile histogram of the bubble growth over the length of the inner vessel in quadrant 1. It can be readily seen that the rate of growth of the bubbles drops near the position of the viewports.

8.4 Temperature of each bubble

Jakob [96] was the first to attempt to find a solution describing the growth of the bubble during the thermal growth. Nikolay Kolev offers a detailed

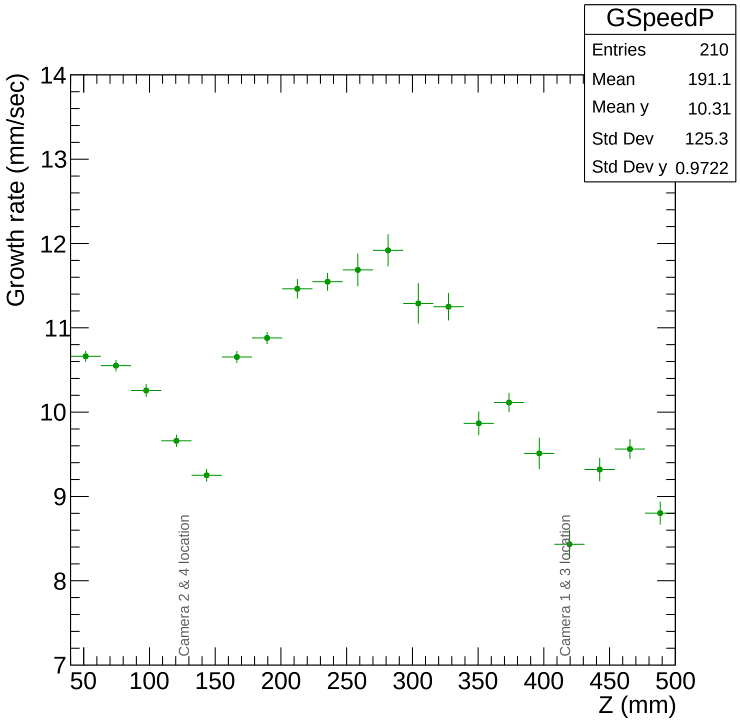

Figure 8.5: The bubble growth rate “a” with varying Z position in quadrant 1. The location of the viewports (and therefore the cameras with the LED rings) are marked.

derivation of the growth of the bubble in the thermal regime in [97]. The formula derived for the growth regime is

$$\frac{dR}{dt} = \frac{B}{2\sqrt{t}}\left[1 - \frac{T_2^{1\sigma} - T'(p)}{T_2 - T'p}\right]\frac{R_1}{3\rho_1}\frac{d\rho}{dt} \tag{8.3}$$

where $B = Ja\sqrt{12a_l/\pi}$. The subscript 1 denotes gas and 2 denotes liquid. Here a_l is the thermal diffusivity of the liquid. Ja is known as the Jakob number in honour of Jakob who was the first to derive it [96, 97]. $T_2^{1\sigma}$ is the liquid-side bubble interface temperature. This is expected to be less than that of the liquid because when the superheated liquid turns into vapour the consumed heat of vaporization reduces the temperature. $T'(p)$ is the boiling point, which is dependent on pressure and can be calculated with the linearized Clausius-Clapeyron relation [98, 99]. T_2 is the superheated liquid temperature. R_1 is the density of the gas bubble, and ρ_1 is the density of the gas. Ja can be computed as

$$Ja = \frac{\rho_l c_p (T - T_b)}{\rho_b L}. \tag{8.4}$$

The model that is applied in this thesis is a simplified version of Equation 8.3. The assumptions are:

- The temperature inside the bubble is the same everywhere, and is equal to the temperature at the thermal boundary between the bubble and the liquid. This temperature is the boiling point of the liquid. In effect, this assumption sets $T_2^{1\sigma} = T'(p)$.
- The density of the gas, ρ_1, remains constant and can be taken as the density of the gas at the boiling point.

Under these assumptions Equation 8.3 simplifies to dR/dt = B/2$\sqrt{t}$. Integrating and substituting for B, one finds R=Ja$\sqrt{\frac{12a_l}{\pi}}\sqrt{t}$. This is known as the Plesset and Zwick model [72], which was presented at the beginning of the Chapter as Equation 8.2.

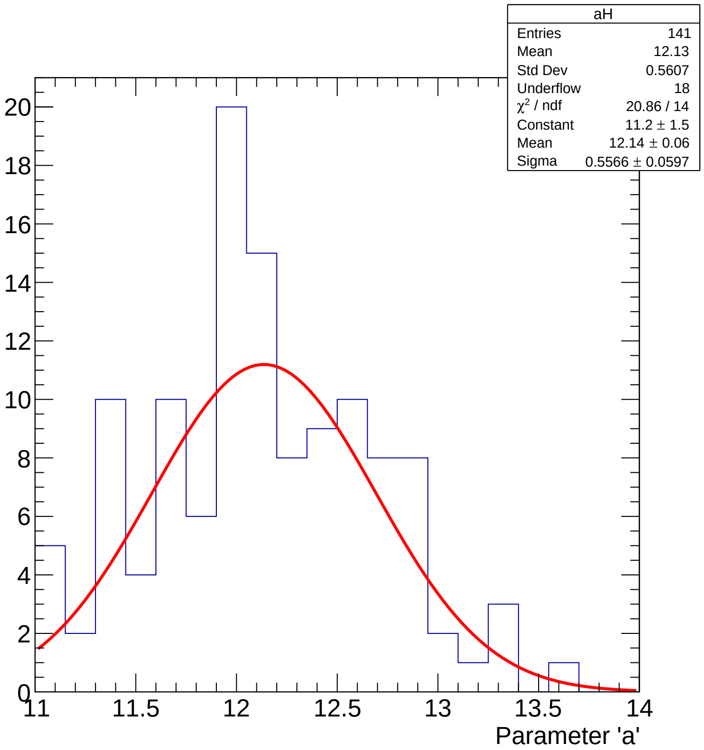

Figure 8.6: The bubble growth factor, a, for all events in quadrant 3 of the detector.

Experimental data available from PICO-60 was fitted to the model and compared with the expected growth rate from Equation 8.2 as

$$R(t) = a\sqrt{t - t_0}. \tag{8.5}$$

The parameter a is given by $\mathrm{Ja}\sqrt{\frac{12a_l}{\pi}}$. Applying the definition of the Jakob number, it is therefore possible to calculate the superheated liquid temperature. Histogram of a was constructed for events in quadrant 3 of the detector and shown in Figure 8.6.

It can be seen that the mean value of the growth factor from the fits is $a = 12.14 \pm 0.05$ mm/$\sqrt{s}$. Assuming that each bubble did not deviate much from the mean temperature of 16 °C in quadrant 3, the Plesset and Zwick model predicts a growth factor of 10.89 mm/$\sqrt{s}$. The values do not agree to 1σ, but Avdeev reports that the Plesset and Zwick model underestimates the growth rate by about 10% [100]. This arises from assumptions made in

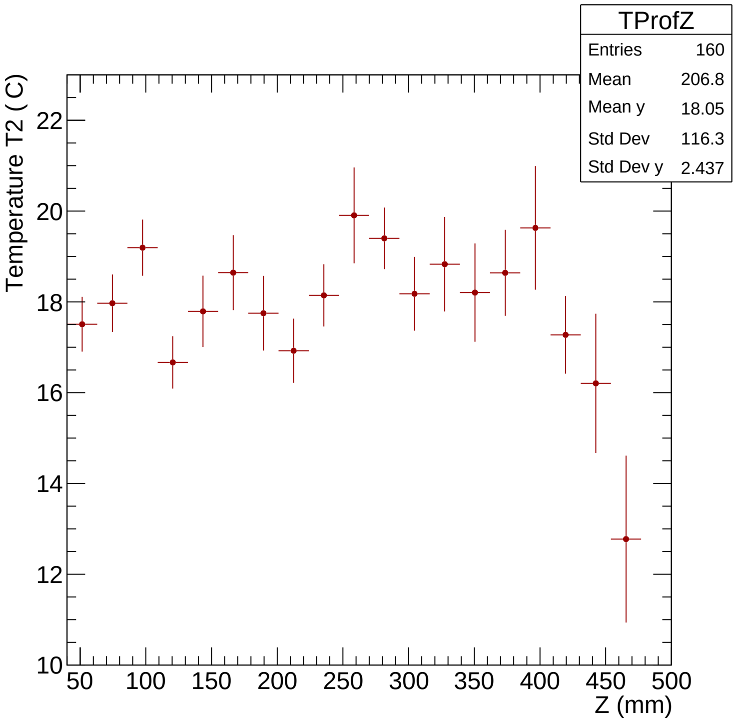

Figure 8.7: Profile histogram of the temperature derived from the growth of the bubbles profiled along Z in quadrant 3. The dataset used is 16 °C, 30 psi.

the model which do not hold in many thermodynamic conditions. Improved models by Mikic [101, 102] and Mohammadein [103] are available to correct for this discrepancy but were not used in this thesis.

With this model Figure 8.4 was re-drawn to consider the temperature scale shown in Figure 8.7. The same treatment of events in quadrant 3 results in a mean temperature of approximately 4 °C warmer than the set point, and a temperature excursion of about 9 °C. Clearly such a large variation indicates a systematic effect that needs to be further studied. The next section explores the motion of the bubbles in the IV which could be used to infer the presence of a flow.

8.5 Velocity profiles in the detector

Chapter 6 introduced the variable θ_z, that is a measurement of the zenith angle of the bubble's track as it rises. The data used to construct this variable, the radial velocity and the vertical velocity of the bubble, can be independently

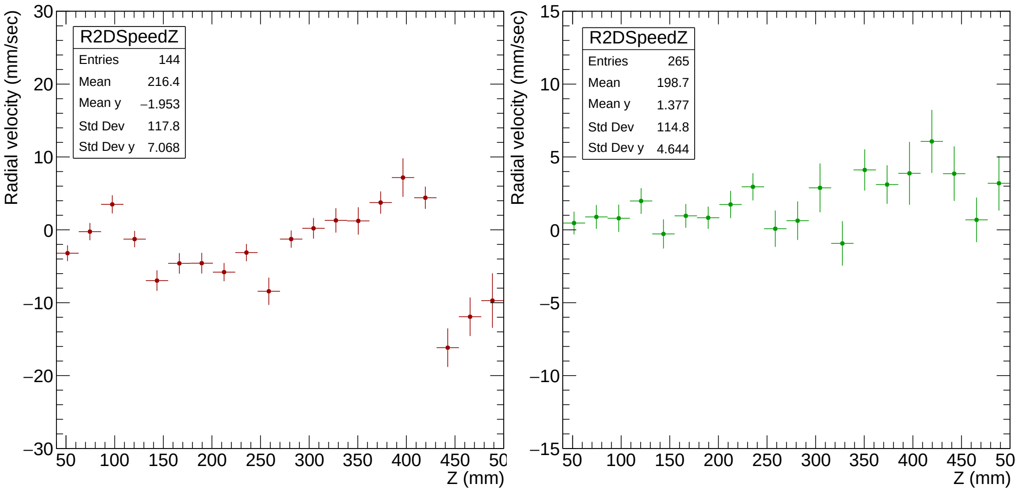

Figure 8.8: Profile histograms along Z of the radial component of the velocity of the bubble. The dataset used is 16 °C, 30 psi. The red histogram (left) is for quadrant 3 and the green one (right) is for quadrant 1.

examined. In Figure 8.8, profile histograms of the radial velocity along Z in quadrants 1 and 3 are shown. In quadrant 3, the radial velocity fluctuates at the bottom and the top of the chamber, suggesting a flow. In quadrant 1, there appears to be some amount of flow, but it is more uniform than quadrant 3. In Figure 8.9, profile histograms of the vertical velocity along Z in quadrants 1 and 3 are shown. In quadrant 3 the vertical velocity appears to remain constant until Z≈400 mm when it rises, possibly due to the proximity to the surface. In quadrant 1, a variation of the vertical velocity is seen at Z≈ 120 mm and Z≈ 370 mm, near the LEDs. This graph can be compared with the bubble growth profile of Figure 8.5. This motion likely generates the systematic effect in determining the bubble growth rate possibly by distorting the shape of the bubble or by cooling or heating the liquid around the bubble.

To conclude this section, it is likely that there is a flow pattern introduced by the LEDs that produces a systematic effect in determining the bubble radii in quadrant 1 by adding a different heat exchange mechanism that is not a part of the single Plesset-Zwick model. To derive the temperatures of the bubbles in quadrant 1, a correction to compensate for this flow must be used. This is not done in this thesis and is left as a future avenue for exploration.

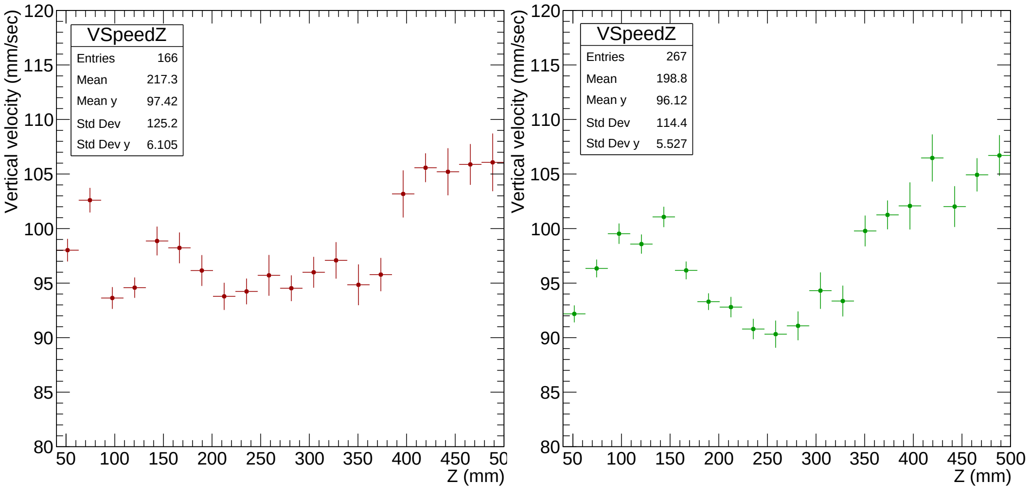

Figure 8.9: Profile histograms along Z of the vertical velocity of the bubble. The dataset used is 16 °C, 30 psi. The red histogram (left) is for quadrant 3 and the green one (right) is for quadrant 1.

Chapter 9

WIMP search result

The methods and the cuts presented in Chapter 6 are used to analyze the dark matter search data. All blinded dark matter search runs are designated a special run type. For 3.3 keV, the blinded run was run_type=10. Although the analysis was published in [64], and this dataset was no longer blinded, it was treated with the same consideration as a blinded run. The 2.4 keV data was designated run_type=100 and the acoustic information was blinded to prevent access to information about discrimination of nuclear recoil events from alpha events.

9.1 Pre-unblinding

After all analysis cuts were applied, a list of potential candidate events was generated for each threshold. A potential candidate here denotes that an event passed all cuts before unblinding. Only α-events and recoil like neutron or WIMP candidates remain at this point. Graphs showing the position of such events in the R-Z plane are shown in Figure 9.1.

9.2 Post unblinding

The unblinding of run BGB33 in January 2017 revealed no candidate low AP events (Figure 9.2). The unblinding and re-processing of the dataset BGB24 was performed between Oct 31-Nov 1, 2017 after the analysis cuts were frozen and the collaboration approved the unblinding.

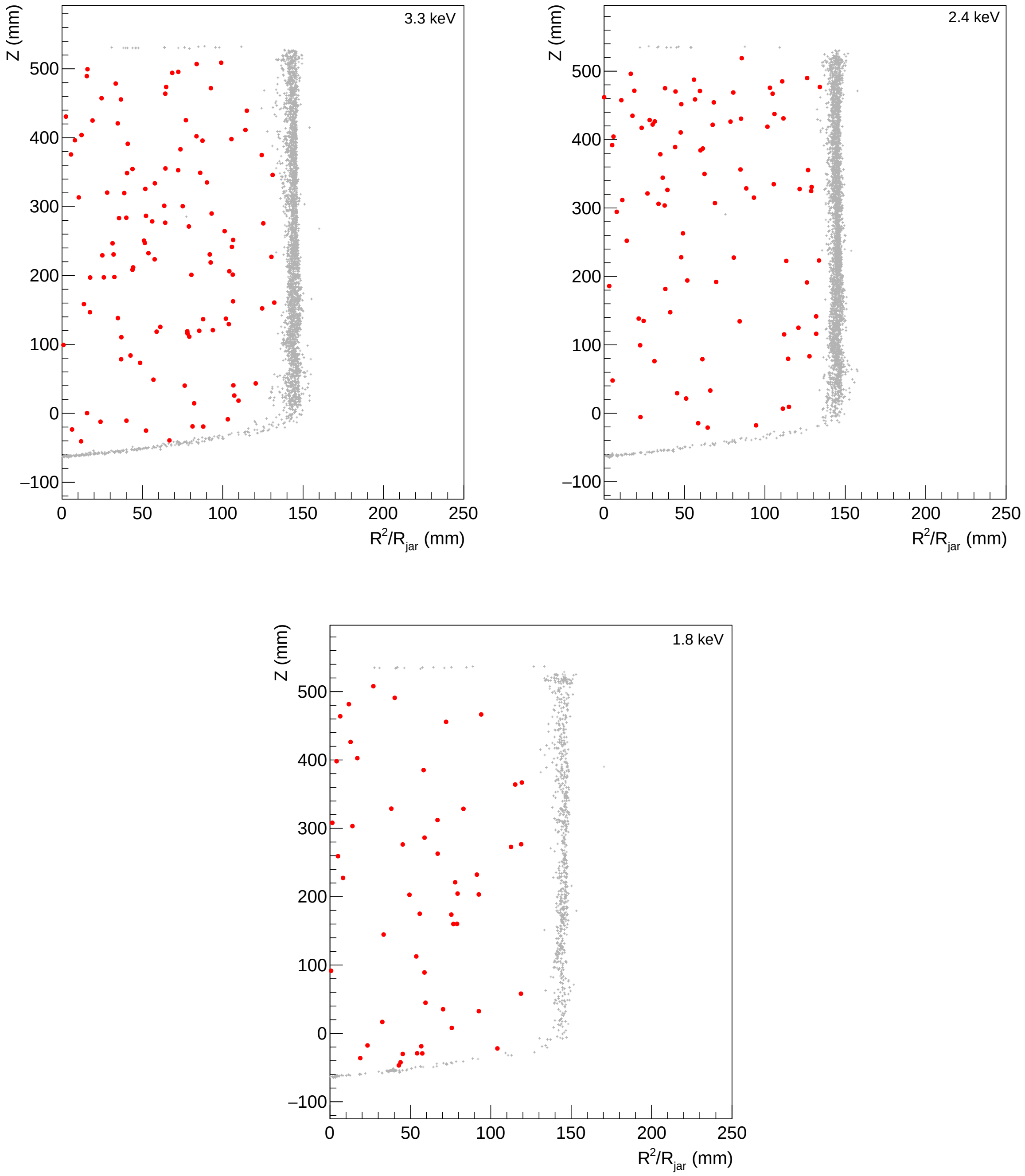

Figure 9.1: Potential candidate events for each Seitz threshold before unblinding. Note that the AP of the 3.3 keV and 1.8 keV dataset were already available and not blinded for the analysis, but were treated the same as the blinded data.

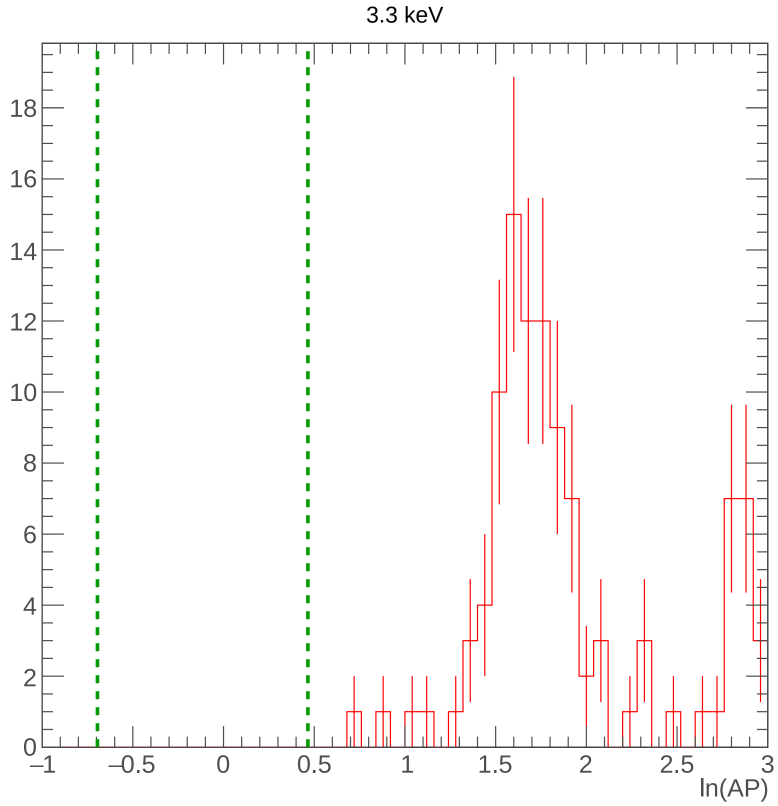

Figure 9.2: All events in BGB33. The green lines are the AP cut bounds for nuclear recoils.

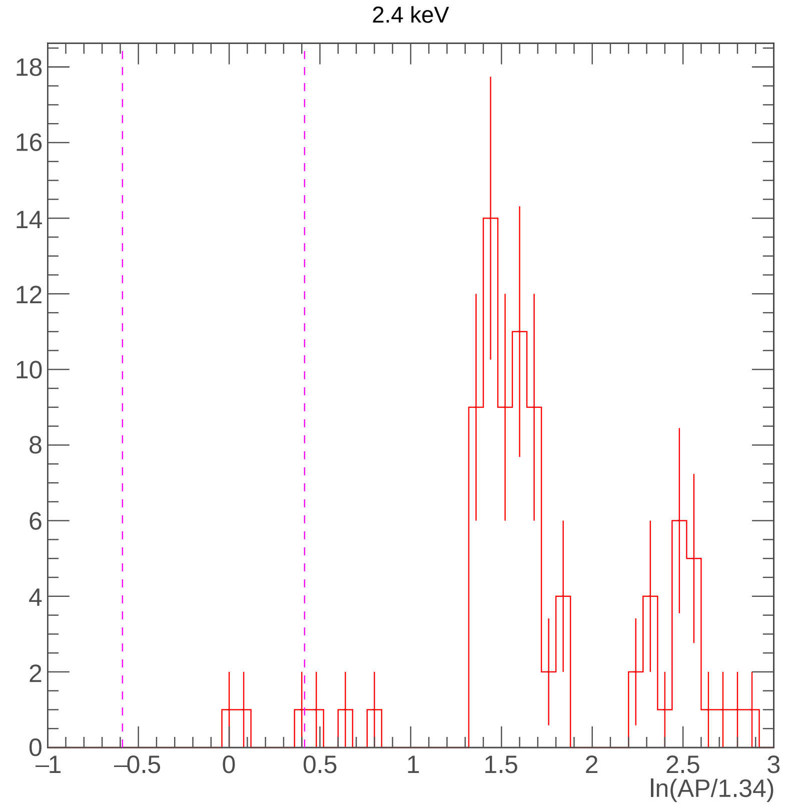

Figure 9.3: All events in BGB24. The pink lines are the AP cut bounds and the events in these bounds are dark matter candidate events.

9.3 Signal

The post unblinding AP distribution of run BGB24 is shown in Figure 9.3, along with the AP cuts. There were three candidate events in the dark matter search run. Figure 9.4 shows the vessel position of all 3 low AP events in the dark matter run.

This number is above the expected number of neutron single events, 0.53±0.40 (predicted from known U and Th activities in the detector materials and by using GEANT4 simulations) and the expected number of gamma events at 0.34±0.31 (from the rate of gammas measured at different thresholds). Background subtraction is not performed on the dataset and every background event is treated as a dark matter candidate event.

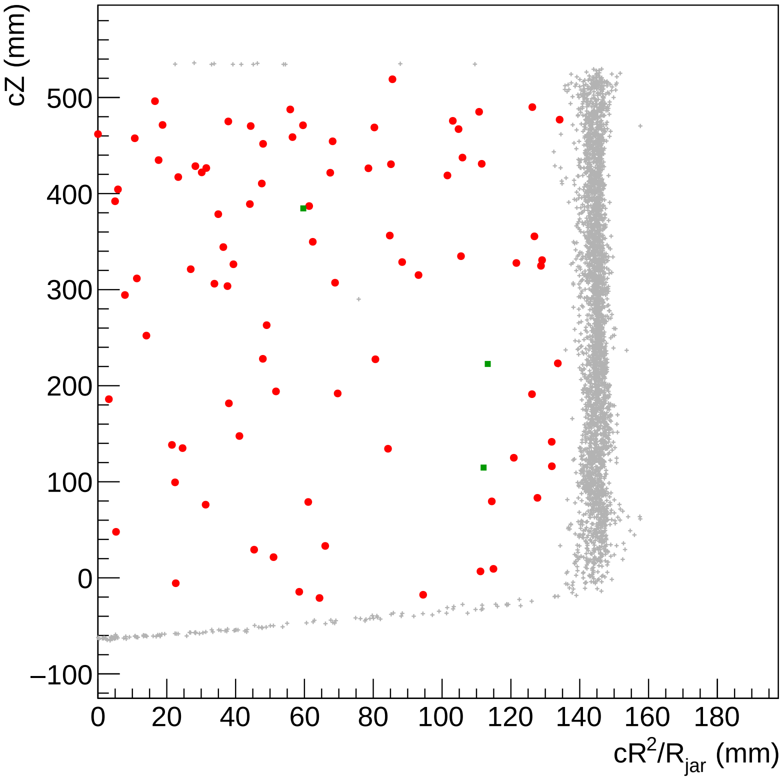

Figure 9.4: All events in BGB24. The grey plus signs are events that have been rejected by one or more cuts, the red circles are events that have been rejected by AP and the green squares are WIMP candidate events.

9.4 Interpretation

Looking back at Figure 9.3, the first alphas can be observed at $ln(AP/1.34) \simeq 1.5$ and neutrons at ln(AP/1.34)$\lesssim$0.5. There is a third population of events with AP values between these two ranges. The origin of this population is unknown. This population is also seen in run BGU18 but not in BGB33. The rate of these events seems to increase with decreased threshold. Alpha timing studies (analogous to the ones shown in Chapter 7) show that these events appear to be not consistent with alphas from the ^{238}U decay chain. These events need to be studied further, since they may be an indication that the suppression of events by cleanliness has approached its limit at these low thresholds. To address this the water buffer liquid will be removed in PICO-40L to eliminate water droplets as a source of nucleation.

Dataset BGB33 has 0 nuclear recoil events and BGB24 has three. An observation of three events is 3.0 standard deviations from the expected background. Since there is an extra class of events in the signal window, the three candidates in dataset BGB24 are interpreted to not be dark matter. Equation 2.4 is used to calculate exclusion limits from the two data sets. The limits may be combined via a simple merge using the formula $\frac{1}{\sigma_{merged}} = \frac{1}{\sigma_{24}} + \frac{1}{\sigma_{33}}$ where $\frac{1}{\sigma_{merged}}$ is the merged exclusion limit, $\frac{1}{\sigma_{24}}$ and $\frac{1}{\sigma_{33}}$ are the exclusion limit from the 2.4 keV and 3.3 keV data respectively assuming that each one of them had three nuclear recoil-like events.

In order to report an upper limit, the experimental data is assumed to be Poisson distributed. Calculation of the cross section of a 30 GeV/c^2 WIMP (see Section 2.4) provides an upper limit of $\sigma_{SDp} < 3.15 \times 10^{-41}$ cm^2. The calculation can be repeated for WIMP masses of 1 GeV to 10^3 GeV at 90% confidence upper limit to produce the spin-dependent WIMP-proton exclusion curve in Figure 9.6 and spin independent WIMP-nucleon version in Figure 9.5. The results presented in this thesis are the world leading constraints on spin-dependent WIMP-proton couplings for direct detection experiments. A comparison of the results from a few competing spin dependent experiments is shown in Figure 9.7.

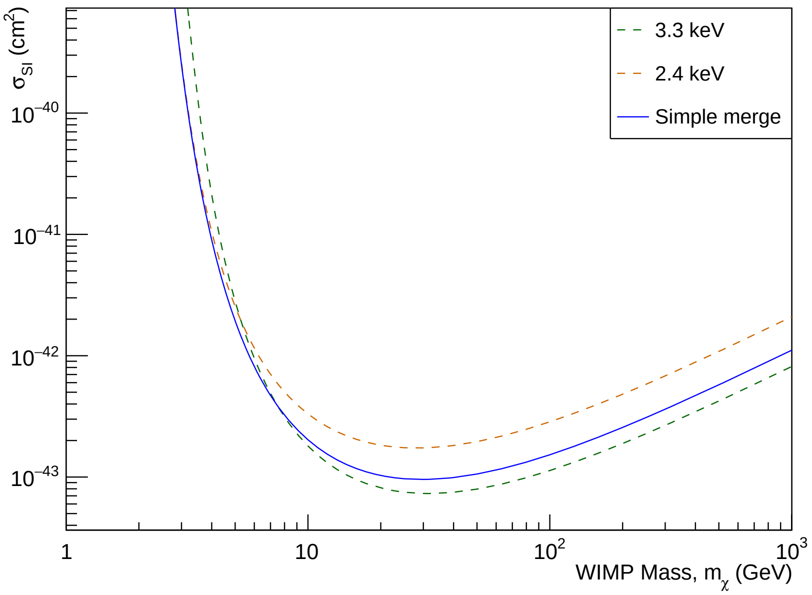

Figure 9.5: Spin independent WIMP-nucleon exclusion curve with BGB33 (green dashes), BGB24 (red dashes) and a simple merge combination (blue solid line) of the two exposures.

9.5 The 1.8 keV dataset

The AP distribution of run BGU18 post unblinding has been shown in Figure 9.8 along with the AP cuts. There were ten candidate events in the dark matter search run. This run was excluded from the calculation of the exclusion curve since it was background limited due to the presence of the nuclear recoil like events (expected to be gamma interactions). This run demonstrates the operational stability of PICO-60 at a low threshold.

9.6 Discussion

In the PICO-60 run BGB33, there were no background events observed. The motivation behind BGB24 and BGU18 was to explore the limits of operational stability and establish the background rate. The observation of three events in BGB24 and 10 events in BGU18 shows that PICO-60 has achieved its design goal and decomissioning PICO-60 was the best option after the runs completed. PICO-40L is being built with a reduction of gamma and neutron

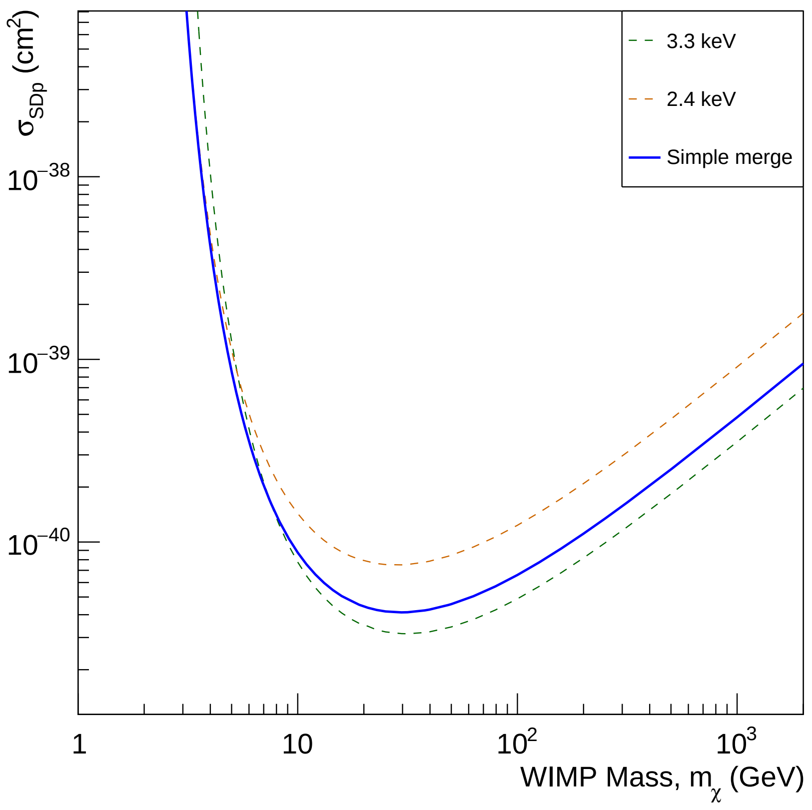

Figure 9.6: Spin dependent WIMP-proton exclusion curve with BGB33 (green dashes), BGB24(red dashes) and a simple merge combination (blue solid line) of the two exposures.

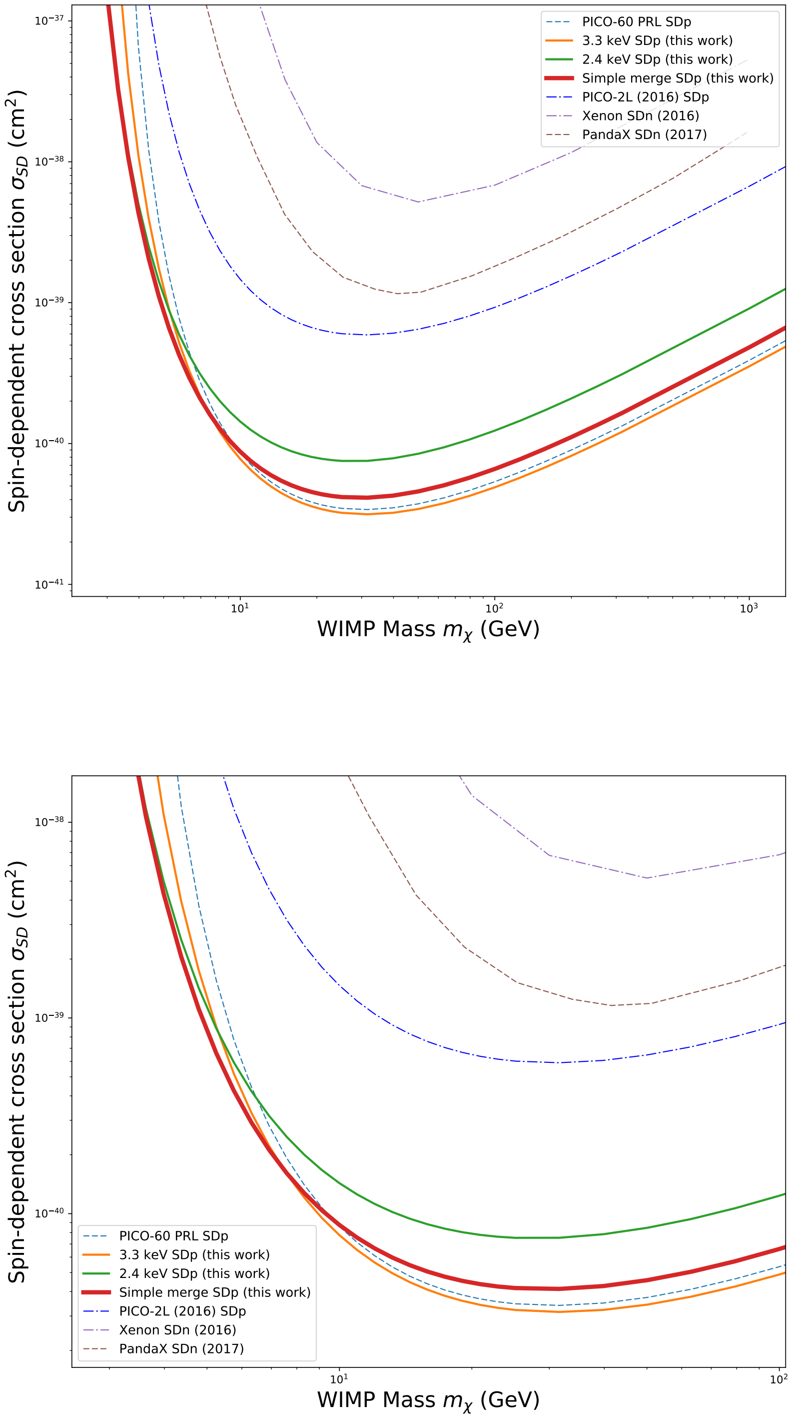

Figure 9.7: Comparison of the limit generated from the analysis presented in this thesis with a few competing experiments such as PICO-2L, PICO-60 run-1, PandaX and XENON. It should be noted that PandaX and Xenon limits are for the WIMP-neutron interaction and are not directly comparable.

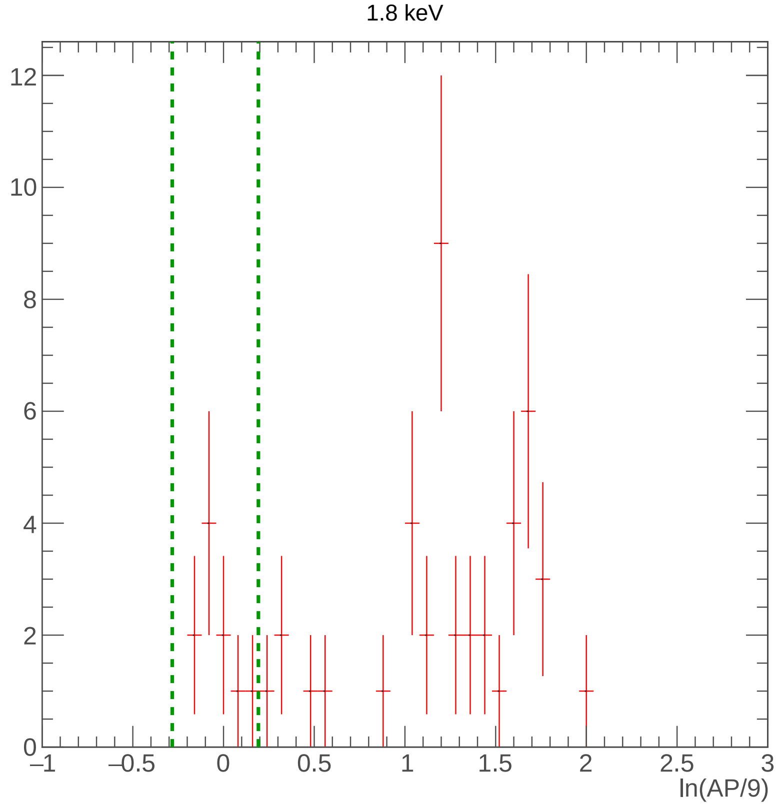

Figure 9.8: All events in BGU18. The green lines are the AP cut bounds and the events in these bounds are gamma, neutrons or dark matter candidate events.

fluxes of the IV to achieve a reduction of the neutron background and as a technology demonstrator for PICO-500.

Chapter 10

Conclusion and further scope of research

The bubble chamber design of PICO-60 enabled it to operate free from backgrounds caused by electrons and gamma rays at 3.3 keV threshold. Piezoelectric sensors have been used to discriminate reliably between alpha decay events and nuclear recoil events.

PICO-60 demonstrated a background free 30 day dark matter search exposure, but the sensitivity of the experiment was limited primarily by neutron flux. Towards the end of the run the glass started "fogging up" due to accumulation of water droplets on the glass jar deteriorating the optics as time went by. The next iteration of PICO is the PICO-40L experiment which eliminates the buffer liquid by changing the design of the experiment. In addition it will use a larger pressure vessel to provide better neutron shielding. PICO-40L serves as a prototype for demonstrating technology that will be used for a tonne scale PICO detector, PICO-500.

Experience gained by studying particulate contamination in PICO-60 provides expertise and knowledge about how to characterize and eliminate particulates and particulate-related backgrounds. The development of AutoBub and improvements to the position reconstruction system have produced a much more accurate bubble reconstruction.

The PICO experiments are ongoing projects that are offering many unique opportunities for further research. This ranges from improving the performance of AutoBub for multi-bubbles to re-designing the optical system so that the accuracy and the bubble size determination can be improved. Different fluids may be tested to probe different regions of the parameter space (such as a hydrogen based target for low mass WIMPs) and even detect different signals (such as solar neutrinos with a hydrofluorocarbon target).

The ultimate limit of the reach of a PICO type detector as a dark matter search experiment is the coherent neutrino scattering limit. For Xe and heavy noble gas targets this limit will be reached in the current generation of detectors since the coherent ν-nucleus scattering has a higher cross section in these than in PICO's light fluorine target. PICO detectors can yet be scaled up before they are expected to be limited by the coherent ν-nucleus scattering. PICO is the leading spin dependent direct dark matter search experiment and will stay in that position for the foreseeable future with PICO-40L and PICO-500 currently in construction and in the design phase respectively.

Bibliography

[1] Planck Collaboration, Ade, P. A. R., Aghanim, N., et al. Planck 2013 results. XVI. Cosmological parameters. pages 67–67, March 2013.

[2] Serjeant, Stephen. *Observational Cosmology*. Cambridge University Press, 2010. ISBN 0-521-15715-3.

[3] Sigurdson, Kris, Doran, Michael, Kurylov, Andriy, Caldwell, Robert, and Kamionkowski, Marc. Dark-matter electric and magnetic dipole moments. *Physical Review D*, 70(8):083501–083501, October 2004. doi: 10.1103/PhysRevD.70.083501.

[4] Kolb, Edward and Turner, Michael. *The Early Universe*. Avalon Publishing, February 1994. ISBN 978-0-8133-4645-8.

[5] Amole, C., Ardid, M., Asner, D. M., et al. Dark matter search results from the PICO-60 CF 3 I bubble chamber. *Physical Review D*, 93(5), March 2016. ISSN 2470-0010, 2470-0029. doi:10.1103/PhysRevD.93.052014.

[6] Jeans, JH. The Motions of the Stars in a Kapteyn Universe. *Monthly Notices Roy. Astrom. Soc.*, 82:122–122, 1922.

[7] Zwicky, F. Die Rotverschiebung von extragalaktischen Nebeln. *Helvetica Physica Acta*, 6:110–127, 1933.

[8] Rubin, V. C., Thonnard, N., and Ford, W. K., Jr. Rotational properties of 21 SC galaxies with a large range of luminosities and radii, from NGC 4605 /R = 4kpc/ to UGC 2885 /R = 122 kpc/. *The Astrophysical Journal*, 238:471–471, June 1980. doi:10.1086/158003.

[9] Markevitch, Maxim. Chandra observation of the most interesting cluster in the Universe. pages 5–5, November 2005.

[10] Massey, Richard, Rhodes, Jason, Ellis, Richard, et al. Dark matter maps reveal cosmic scaffolding. *Nature*, 445(7125):286–90, January 2007. doi: 10.1038/nature05497.

[11] Jarosik, N., Bennett, C. L., Dunkley, J., et al. Seven-Year Wilkinson Microwave Anisotropy Probe (WMAP) Observations: Sky Maps, Systematic Errors, and Basic Results. *Astrophysical Journal Supplement Series*, pages 42–42, January 2010.

[12] Kessler, Richard, Becker, Andrew C., Cinabro, David, et al. First-year Sloan Digital Sky Survey II supernova results: Hubble diagram and cosmological parameters. *The Astrophysical Journal Supplement Series*, 185(1):32–84, November 2009. doi:10.1088/0067-0049/185/1/32.

[13] Riess, Adam G., Macri, Lucas, Casertano, Stefano, et al. A redetermination of the hubble constant with the hubble space telescope from a differential distance ladder. *The Astrophysical Journal*, 699(1):539–563, July 2009. doi:10.1088/0004-637X/699/1/539.

[14] Ryden, Barbara. *Introduction to Cosmology.* Addison-Wesley, San Francisco, 2003. ISBN 978-0-8053-8912-8.

[15] Rubin, Vera C. and Ford, W. Kent, Jr. Rotation of the Andromeda Nebula from a Spectroscopic Survey of Emission Regions. *The Astrophysical Journal*, 159:379–379, February 1970. doi:10.1086/150317.

[16] Begeman, K. G., Broeils, A. H., and Sanders, R. H. Extended rotation curves of spiral galaxies: Dark haloes and modified dynamics. *Monthly Notices of the Royal Astronomical Society*, 249(3):523–537, April 1991. doi:10.1093/mnras/249.3.523.

[17] Carignan, Claude, Chemin, Laurent, Huchtmeier, Walter K., and Lockman, Felix J. The Extended H i Rotation Curve and Mass Distribution of M31. *The Astrophysical Journal*, 641(2):L109–L112, April 2006. doi: 10.1086/503869.

[18] Gastaldello, Fabio, Buote, David A., Humphrey, Philip J., Zappacosta, Luca, Bullock, James S., Brighenti, Fabrizio, and Mathews, William G. Probing the Dark Matter and Gas Fraction in Relaxed Galaxy Groups with X-Ray Observations from *Chandra* and *XMM-Newton*. *The Astrophysical Journal*, 669(1):158–183, November 2007. ISSN 0004-637X, 1538-4357. doi:10.1086/521519.

[19] Clowe, Douglas, Bradač, Maruša, Gonzalez, Anthony H., Markevitch, Maxim, Randall, Scott W., Jones, Christine, and Zaritsky, Dennis. A Direct Empirical Proof of the Existence of Dark Matter. *The Astrophysical Journal*, 648(2):L109–L113, September 2006. doi:10.1086/508162.

[20] Stocke, John T., Shull, J. Michael, and Penton, Steven V. The Baryon Content of the Local Intergalactic Medium. pages 25–25, July 2004.

[21] Bradač, Maruša, Allen, Steven W., Treu, Tommaso, Ebeling, Harald, Massey, Richard, Morris, R. Glenn, von der Linden, Anja, and Applegate, Douglas. Revealing the Properties of Dark Matter in the Merging Cluster MACS J0025.4-1222. *The Astrophysical Journal*, 687(2):959–967, November 2008. doi:10.1086/591246.

[22] Milgrom, M. A modification of the Newtonian dynamics as a possible alternative to the hidden mass hypothesis. *The Astrophysical Journal*, 270:365–365, July 1983. doi:10.1086/161130.

[23] Bekenstein, Jacob. Relativistic gravitation theory for the modified Newtonian dynamics paradigm. *Physical Review D*, 70(8):083509–083509, October 2004. doi:10.1103/PhysRevD.70.083509.

[24] Randall, Scott W., Markevitch, Maxim, Clowe, Douglas, Gonzalez, Anthony H., and Bradač, Marusa. Constraints on the Self-Interaction Cross Section of Dark Matter from Numerical Simulations of the Merging Galaxy Cluster 1E 0657-56. *The Astrophysical Journal*, 679(2):1173–1180, June 2008. ISSN 0004-637X, 1538-4357. doi:10.1086/587859.

[25] Planck Collaboration, Ade, P. A. R., Aghanim, N., et al. Planck 2015 results. XIII. Cosmological parameters. February 2015.

[26] Friedman, A. Über die Krümmung des Raumes. *Zeitschrift für Physik*, 10(1):377–386, December 1922. ISSN 1434-6001, 1434-601X. doi:10.1007/BF01332580.

[27] Smoot, George F. COBE observations and results. pages 1–10. ASCE, 1999. ISBN 978-1-56396-847-1. doi:10.1063/1.59326.

[28] Komatsu, E., Smith, K. M., Dunkley, J., et al. SEVEN-YEAR WILKINSON MICROWAVE ANISOTROPY PROBE (WMAP) OBSERVATIONS: COSMOLOGICAL INTERPRETATION. *The Astrophysical Journal Supplement Series*, 192(2):18–18, February 2011. doi:10.1088/0067-0049/192/2/18.

[29] Eisenstein, Daniel J., Zehavi, Idit, Hogg, David W., et al. Detection of the Baryon Acoustic Peak in the Large-Scale Correlation Function of SDSS Luminous Red Galaxies. *The Astrophysical Journal*, 633(2):560–574, November 2005. ISSN 0004-637X, 1538-4357. doi:10.1086/466512.

[30] Ling, F S, Nezri, E, Athanassoula, E, and Teyssier, R. Dark matter direct detection signals inferred from a cosmological N-body simulation with baryons. *Journal of Cosmology and Astroparticle Physics*, (1002):012–012, February 2010.

[31] Bertone, Gianfranco, Hooper, Dan, and Silk, Joseph. Particle dark matter: Evidence, candidates and constraints. *Physics Reports*, 405(5-6):279–390, January 2005. ISSN 03701573. doi:10.1016/j.physrep.2004.08.031.

[32] Harvey, David, Massey, Richard, Kitching, Thomas, Taylor, Andy, and Tittley, Eric. The nongravitational interactions of dark matter in colliding galaxy clusters. *Science (New York, N.Y.)*, 347(6229):1462–5, March 2015. doi:10.1126/science.1261381.

[33] Ackermann, M., Ajello, M., Albert, A., et al. Limits on Dark Matter Annihilation Signals from the Fermi LAT 4-year Measurement of the Isotropic Gamma-Ray Background. *arXiv:1501.05464 [astro-ph]*, January 2015.

[34] Lu, Bo-Qiang and Zong, Hong-Shi. Limits on dark matter from AMS-02 antiproton and positron fraction data. *Physical Review D*, 93(10), May 2016. ISSN 2470-0010, 2470-0029. doi:10.1103/PhysRevD.93.103517.

[35] Peter, Annika H. G. and Benson, Andrew J. Dark-matter decays and Milky Way satellite galaxies. *Physical Review D*, 82(12):123521–123521, December 2010. doi:10.1103/PhysRevD.82.123521.

[36] Schneider, Peter. *Extragalactic Astronomy and Cosmology.* Springer Berlin Heidelberg, Berlin, Heidelberg, 2006. ISBN 978-3-540-33174-2 978-3-540-33175-9. doi:10.1007/978-3-540-33175-9.

[37] Peccei, R. D. and Quinn, Helen R. CP Conservation in the Presence of Pseudoparticles. *Physical Review Letters*, 38(25):1440–1443, June 1977. doi:10.1103/PhysRevLett.38.1440.

[38] Stern, Ian P. Axion dark matter searches. pages 456–461. March 2014. doi:10.1063/1.4883465.

[39] Feng, Jonathan L., Matchev, Konstantin T., and Wilczek, Frank. Neutralino dark matter in focus point supersymmetry. *Physics Letters B*, 482(4):388–399, June 2000. ISSN 03702693. doi:10.1016/S0370-2693(00) 00512-8.

[40] Peter, Annika H.G., Gluscevic, Vera, Green, Anne M., Kavanagh, Bradley J., and Lee, Samuel K. WIMP physics with ensembles of direct-detection experiments. *Physics of the Dark Universe*, 5-6:45–74, December 2014. ISSN 22126864. doi:10.1016/j.dark.2014.10.006.

[41] Lewin, J.D. and Smith, P.F. Review of mathematics, numerical factors, and corrections for dark matter experiments based on elastic nuclear recoil. *Astroparticle Physics*, 6(1):87–112, December 1996. doi:10.1016/S0927-6505(96)00047-3.

[42] Archambault, S., Archer, A., Benbow, W., et al. Dark matter constraints from a joint analysis of dwarf Spheroidal galaxy observations with VERITAS. *Physical Review D*, 95(8), April 2017. ISSN 2470-0010, 2470-0029. doi:10.1103/PhysRevD.95.082001.

[43] Barger, Vernon, Keung, Wai-Yee, Shaughnessy, Gabe, and Tregre, Adam. High energy neutrinos from neutralino annihilations in the Sun. *Physical Review D*, 76(9):095008–095008, November 2007. doi:10.1103/PhysRevD.76.095008.

[44] Battaglieri, Marco, Belloni, Alberto, Chou, Aaron, et al. US Cosmic Visions: New Ideas in Dark Matter 2017: Community Report. *arXiv:1707.04591 [astro-ph, physics:hep-ex, physics:hep-ph]*, July 2017.

[45] Collaboration, CMS. Search for dark matter produced with an energetic jet or a hadronically decaying W or Z boson at sqrt(s) = 13 TeV. *Journal of High Energy Physics*, 2017(7), July 2017. ISSN 1029-8479. doi:10.1007/JHEP07(2017)014.

[46] Cushman, P., Galbiati, C., McKinsey, D. N., et al. Snowmass CF1 Summary: WIMP Dark Matter Direct Detection. pages 47–47, October 2013.

[47] Lippincott, Hugh. Recent Results from PICO - Searching for Dark Matter with Bubble Chambers. In *Joint Experimental-Theoretical Physics Seminar*. 2015.

[48] Tovey, D.R., Gaitskell, R.J., Gondolo, P., Ramachers, Y., and Roszkowski, L. A new model-independent method for extracting spin-dependent cross section limits from dark matter searches. *Physics Letters B*, 488(1):17–26, August 2000. doi:10.1016/S0370-2693(00)00846-7.

[49] Behnke, E., Besnier, M., Bhattacharjee, P., et al. Final results of the PICASSO dark matter search experiment. *Astroparticle Physics*, 90(Supplement C):85 – 92, 2017. ISSN 0927-6505. doi:https://doi.org/10.1016/j.astropartphys.2017.02.005.

[50] Amole, C., Ardid, M., Asner, D. M., et al. Dark Matter Search Results from the PICO-2L C_3F_8 Bubble Chamber. *Physical Review Letters*, 114(23):231302–231302, June 2015. doi:10.1103/PhysRevLett.114.231302.

[51] Felizardo, M., Girard, T. A., Morlat, T., et al. Final Analysis and Results of the Phase II SIMPLE Dark Matter Search. *Physical Review Letters*, 108(20), May 2012. ISSN 0031-9007, 1079-7114. doi:10.1103/PhysRevLett.108.201302.

[52] Seitz, Frederick. On the Theory of the Bubble Chamber. *Physics of Fluids*, 1(1):2–2, January 1958. ISSN doi:10.1063/1.1724333. doi:10.1063/1.1724333.

[53] Kuźniak, M., Amaudruz, P.-A., Batygov, M., et al. DEAP-3600 Dark Matter Search. *Nuclear and Particle Physics Proceedings*, 273-275:340–346, April 2016. ISSN 24056014. doi:10.1016/j.nuclphysbps.2015.09.048.

[54] Amaudruz, P.-A., Batygov, M., Beltran, B., et al. Measurement of the scintillation time spectra and pulse-shape discrimination of low-energy β and nuclear recoils in liquid argon with DEAP-1. *Astroparticle Physics*, 85:1–23, December 2016. ISSN 09276505. doi:10.1016/j.astropartphys.2016.09.002.

[55] Boccone, V, Lightfoot, P K, Mavrokoridis, K, et al. Development of wavelength shifter coated reflectors for the ArDM argon dark matter detector. *Journal of Instrumentation*, 4(06):P06001–P06001, June 2009. ISSN 1748-0221. doi:10.1088/1748-0221/4/06/P06001.

[56] Akerib, D. S., Alsum, S., Araújo, H. M., et al. Results from a Search for Dark Matter in the Complete LUX Exposure. *Physical Review Letters*, 118(2), January 2017. ISSN 0031-9007, 1079-7114. doi:10.1103/PhysRevLett.118.021303.

[57] Agnese, R., Anderson, A. J., Asai, M., et al. Search for Low-Mass Weakly Interacting Massive Particles with SuperCDMS. *Physical Review Letters*, 112(24), June 2014. ISSN 0031-9007, 1079-7114. doi:10.1103/PhysRevLett.112.241302.

[58] Tiffenberg, Javier, Sofo-Haro, Miguel, Drlica-Wagner, Alex, Essig, Rouven, Guardincerri, Yann, Holland, Steve, Volansky, Tomer, and Yu, Tien-Tien. Single-electron and single-photon sensitivity with a silicon Skipper CCD. *Physical Review Letters*, 119(13), September 2017. ISSN 0031-9007, 1079-7114. doi:10.1103/PhysRevLett.119.131802.

[59] Aguilar-Arevalo, A., Amidei, D., Bertou, X., et al. First Direct-Detection Constraints on eV-Scale Hidden-Photon Dark Matter with DAMIC at SNOLAB. *Physical Review Letters*, 118(14), April 2017. ISSN 0031-9007, 1079-7114. doi:10.1103/PhysRevLett.118.141803.

[60] Arnaud, Q., Asner, D., Bard, J.-P., et al. First results from the NEWS-G direct dark matter search experiment at the LSM. *arXiv:1706.04934 [astro-ph, physics:physics]*, June 2017.

[61] Ng, Kenny C. Y., Beacom, John F., Peter, Annika H. G., and Rott, Carsten. Solar atmospheric neutrinos: A new neutrino floor for dark matter searches. *Physical Review D*, 96(10), November 2017. ISSN 2470-0010, 2470-0029. doi:10.1103/PhysRevD.96.103006.

[62] Aubin, F., Auger, M., Genest, M. H., et al. Discrimination of nuclear recoils from alpha particles with superheated liquids. *New Journal of Physics*, 10, July 2008. ISSN 1367-2630. doi:10.1088/1367-2630/10/10/103017.

[63] Fitzpatrick, A. Liam, Haxton, Wick, Katz, Emanuel, Lubbers, Nicholas, and Xu, Yiming. The Effective Field Theory of Dark Matter Direct Detection. *Journal of Cosmology and Astroparticle Physics*, 2013(02):004–004, February 2013. ISSN 1475-7516. doi:10.1088/1475-7516/2013/02/004.

[64] Amole, C., Ardid, M., Arnquist, Isaac J., et al. Dark Matter Search Results from the PICO-60 C_3F_8 Bubble Chamber. *Physical review letters*, 118(25):251301, 2017.

[65] Lewin, J.D. and Smith, P.F. Review of mathematics, numerical factors, and corrections for dark matter experiments based on elastic nuclear recoil. *Astroparticle Physics*, 6(1):87–112, December 1996. doi:10.1016/S0927-6505(96)00047-3.

[66] Fitzpatrick, A. Liam, Haxton, Wick, Katz, Emanuel, Lubbers, Nicholas, and Xu, Yiming. Model Independent Direct Detection Analyses. *arXiv:1211.2818 [hep-ph]*, November 2012.

[67] Barger, Vernon, Keung, Wai-Yee, and Shaughnessy, Gabe. Spin dependence of dark matter scattering. *Physical Review D*, 78(5):056007, September 2008. doi:10.1103/PhysRevD.78.056007.

[68] Aprile, E., Aalbers, J., Agostini, F., et al. The XENON1T Dark Matter Experiment. *arXiv:1708.07051 [astro-ph, physics:hep-ex, physics:physics]*, August 2017.

[69] Beltrán, Maria, Hooper, Dan, Kolb, Edward W., Krusberg, Zosia A. C., and Tait, Tim M. P. Maverick dark matter at colliders. *Journal of High Energy Physics*, 2010(9):37, September 2010. ISSN 1029-8479. doi:10.1007/JHEP09(2010)037.

[70] Sirunyan, A. M., Tumasyan, A., Adam, W., et al. Search for dark matter produced with an energetic jet or a hadronically decaying W or Z boson at s=13 TeV. *Journal of High Energy Physics*, 2017(7):14, July 2017. ISSN 1029-8479. doi:10.1007/JHEP07(2017)014.

[71] Collaboration, CMS. Search for new physics in the monophoton final state in proton-proton collisions at sqrt(s) = 13 TeV. *arXiv:1706.03794 [hep-ex]*, June 2017.

[72] Zwick, Stanley Alan. *The Growth and Collapse of Cavitation Bubbles*. Ph.D. thesis, January 1955.

[73] Dergarabedian, Paul. *The Rate of Growth of Vapor Bubbles in Superheated Water*. Ph.D. thesis, March 1952.

[74] Plesset, M. S. and Zwick, S. A. The Growth of Vapor Bubbles in Superheated Liquids. *Journal of Applied Physics*, 25(4):493–500, April 1954. doi:10.1063/1.1721668.

[75] Harper, Mark J. and Rich, Jeremy C. Radiation-induced nucleation in superheated liquid droplet neutron detectors. *Nuclear Instruments and Methods in Physics Research Section A: Accelerators, Spectrometers, Detectors and Associated Equipment*, 336(1-2):220–225, 1993.

[76] Apfel, Robert E. The superheated drop detector. *Nuclear Instruments and Methods*, 162(1):603–608, June 1979. ISSN 0029-554X. doi:10.1016/0029-554X(79)90735-3.

[77] Norman, Amos and Spiegler, P. Radiation Nucleation of Bubbles in Water. *Nuclear Science and Engineering*, 16(2):213–217, June 1963. doi: dx.doi.org/10.13182/NSE63-A26502.

[78] Halzen, Francis and Martin, Alan D. *Quarks and Leptons: An Introductory Course in Modern Particle Physics*. Wiley, New York, 1st edition edition, January 1984. ISBN 978-0-471-88741-6.

[79] L.D. Landau & E.M. Lifshitz. *Fluid Mechanics*.

[80] Lemmon, Eric W, Huber, Marcia L., McLinden, Mark O., and Bell, Ian. Reference Fluid Thermodynamic and Transport Properties Database (REFPROP), 2009-04-22T16:52-04:00.

[81] Vacek, Vic. Fluorocarbon C3F8 Properties. Technical report, CERN, March 1999.

[82] Jauregui, Eric Vazquez and Venegas, Alberto Noel Cruz. PICO-60 neutron backgrounds estimation. Technical Report 3054v1, 2017.

[83] Undagoitia, Teresa Marrodan and Rauch, Ludwig. Dark matter direct-detection experiments. September 2015. doi:10.1088/0954-3899/43/1/013001.

[84] Duncan, Fraser, Barr, Allan, Lawson, Ian, McFarlane, Ken, and Venne, Stephane. SNOLAB Technical Reference Manual. Technical report, Sudbury, 2016.

[85] Clark, Kenneth. *A New and Improved Spin-Dependent Dark Matter Exclusion Limit Using the PICASSO Experiment*. Thesis, November 2009.

[86] Klaasen, K. Galileo Solid-State Imaging Subsystem Calibration Report: Part 2. Technical report, Pasadena, California, 1993.

[87] Bertrand, Patrick and Lu-Tao, Weng. Time-of-Flight Secondary Ion Mass Spectrometry (ToF-SIMS). In *Microbeam and Nanobeam Analysis*, Mikrochimica Acta Supplement, pages 167–182. Springer, Vienna, 1996. ISBN 978-3-211-82874-8 978-3-7091-6555-3. doi:10.1007/978-3-7091-6555-3_8.

[88] Becker, J. Sabine. Inductively coupled plasma mass spectrometry (ICP-MS) and laser ablation ICP-MS for isotope analysis of long-lived radionuclides. *International Journal of Mass Spectrometry*, 242(2):183–195, April 2005. ISSN 1387-3806. doi:10.1016/j.ijms.2004.11.009.

[89] Advantec. Advantec H020A025A. https://octopart.com/h020a025a-advantec-56748350.

[90] US Military. Military Standard 1246C Product cleanliness levels and contamination control program. Military Standard MIL-STD-1246C FSC 3694, US Army Missile Command, Redstone Arsenal, April 1994.

[91] Itseez, WIllow Garage, and Intel. OpenCV, October 2017.

[92] Otsu, Nobuyuki. A Threshold Selection Method from Gray-Level Histograms. *IEEE Transactions on Systems, Man, and Cybernetics*, 9(1):62–66, January 1979. ISSN 0018-9472, 2168-2909. doi:10.1109/TSMC.1979.4310076.

[93] Suzuki, Satoshi and Abe, Keiichi. Topological structural analysis of digitized binary images by border following. *Computer Vision, Graphics, and Image Processing*, 30(1):32–46, April 1985. ISSN 0734-189X. doi:10.1016/0734-189X(85)90016-7.

[94] Teh, C.-H. and Chin, R.T. On the detection of dominant points on digital curves. *IEEE Transactions on Pattern Analysis and Machine Intelligence*, 11(8):859–872, Aug./1989. ISSN 01628828. doi:10.1109/34.31447.

[95] Prosperetti, Andrea and Plesset, Milton S. Vapour-bubble growth in a superheated liquid. *Journal of Fluid Mechanics*, 85(02):349, March 1978. ISSN 0022-1120, 1469-7645. doi:10.1017/S0022112078000671.

[96] Jakob, Max. Kondensation und Verdampfung. *Zeitschrift des Vereins Deutscher Ingenieure*, 76(48):1161–1170, 1932.

[97] Kolev, Nikolay Ivanov. *Multiphase Flow Dynamics 3*. Springer Berlin Heidelberg, Berlin, Heidelberg, 2012. ISBN 978-3-642-21371-7 978-3-642-21372-4. doi:10.1007/978-3-642-21372-4.

[98] Clausius, R. Ueber die bewegende Kraft der Wärme und die Gesetze, welche sich daraus für die Wärmelehre selbst ableiten lassen. *Annalen der Physik und Chemie*, 155(4):500–524, 1850. ISSN 00033804, 15213889. doi:10.1002/andp.18501550403.

[99] Clapeyron, Benoît Paul Émile. *Journal de l'École polytechnique / publié par le Conseil d'instruction de cet établissement*. Gauthier-Villars, Paris, 1834. Ark:/12148/bpt6k4336791.

[100] Avdeev, A. A. Laws of vapor bubble growth in the superheated liquid volume (thermal growth scheme). *High Temperature*, 52(4):588–602, July 2014. ISSN 0018-151X, 1608-3156. doi:10.1134/S0018151X14040026.

[101] Mikic, B. B. Bubble growth rates in non-uniform temperature field. *Progress in Heat and Mass Transfer*, pages 283–293, 1969.

[102] Mikic, B.B, Rohsenow, W.M, and Griffith, P. On bubble growth rates. *International Journal of Heat and Mass Transfer*, 13(4):657–666, April 1970. ISSN 00179310. doi:10.1016/0017-9310(70)90040-2.

[103] Mohammadein, S. A. and Mohamed, K. G. Growth of a Vapour Bubble in a Superheated Liquid of Variable Surface Tension and Viscosity Between Two-phase Flow. *Applied Mathematics & Information Sciences*, 7(6):2311–2318, November 2013. ISSN 1935-0090, 2325-0399. doi: 10.12785/amis/070622.

Appendices

Appendix A

Run types in PICO-60

Run type	Description	Remarks
0	Background	Unblind data
10	Background (Dark matter search)	Blind data with 200 Hz frame rate for images.
100	Background (Dark matter search)	Blind data with 340 Hz frame rate for images.
2	Neutron calibration	AmBe source at the bottom of the ST.
14	Neutron calibration	^{252}Cf source 40cm from the bottom of the ST.
15	Neutron calibration	^{252}Cf source 60cm from the bottom of the ST.
16	Neutron calibration	^{252}Cf source 80cm from the bottom of the ST.
21	Gamma calibration	^{133}Ba source 100cm from the bottom of the ST.
22	Gamma calibration	^{133}Ba source 45cm from the bottom of the ST.
23	Gamma calibration	^{133}Ba source 120cm from the bottom of the ST.
24	Gamma calibration	^{133}Ba source 10cm from the bottom of the ST.
32	Gamma calibration	^{133}Ba source 45cm from the bottom of the ST. Used just after the frame rate change.
41	Gamma calibration	^{60}Co source 45cm from the bottom of the ST. Used just after the frame rate change.
99	Engineering / test / commissioning	Do not use for analysis

Table A.1: A list of run types used in PICO-60. ST stands for "source tube", a tube next to the detector in which the sources were deployed. The camera frame rate was upgraded on January 25, 2017 from 200Hz to 340Hz.

Appendix B

Full list of sensors in PICO-60

Type	Fluid	Location and function	Make and model	Range	Signal
PI-1	PG	outer volume glycol pressure	McMaster 3845K3	600 PSIG	none
PT-2	PG	slow response BC pressure	Setra 2251-0500P-A-C4-11-B1	500 PSIA	4-20mA
PT-3	PG	fast response BC pressure	Noshok 100-500-2-1-2-1	500 PSIG	4-20mA
ZT-4	—	BC bellows position	Unimeasure JX-PA-3.8-N-1-21S-31N	3.8 inches	1000 ohms
PT-5	PG	Ultra-fast dynamic pressure response	Dytran 2005V	50 psi dynamic	4-20mA
ZT-6	—	piston position	Balluf BTL5-E10-M0203-Z-S3L	8 inches	4-20mA
PIT-7	A	recompression air supply Ashcroft	20X 1005 HD 02L	160 PSIG	4-20mA
FI-8	PG	pump recycle	Kobold VKM 6103	0.05-0.3 GPM	none
WT-9	PG	diaphragm tank weight	Honeywell Sensotec C2W	0-100 lb	4-20mA
WE-9	PG	diaphragm tank weight	Honeywell 53	0/100 lb	none
PI-10	A	diaphragm tank air pressure	Wilkerson with regulator	60 PSIG	none
LI-11	PG	degassing chamber	John C Ernst Inc. 415-05	0-16"	none
ZI-12	—	BC bellows position indicator	ruler and pointer	-2.0" to +2.0"	none

PT-14	A	atmospheric pressure	Noshok 100-30A-2-1-2-1	0 to 30 psia	4-20mA
LS-15	PG	Glycol drip pan	McMaster 4646K12		contact
LI-21	W	water tank level indicator	Dwyer Magnehelic	0-20"	none
MS-22	W	camera enclosure water sensor	Dwyer Series WD2	digital	contact
LT-23	W	water tank level sensor	Echotouch LU20-5000	0.5’-18’	4-20mA
TE-30	PG	outer volume shell temp	Minco S101733PD3S80		100 ohm
TT-30	PG	outer volume shell temp	Minco TT176 PD1N	0-50C	4-20mA
TE-31	PG	outer volume shell temp	Minco S101733PD3S80		100 ohm
TT-31	PG	outer volume shell temp	Minco TT176 PD1N	0-50C	4-20mA
TE-32	PG	outer volume shell temp	Minco S101733PD3S80		100 ohm
TT-32	PG	outer volume shell temp	Minco TT176 PD1N	0-50C	4-20mA
TE-33	PG	outer volume shell temp	Minco S101733PD3S80		100 ohm
TT-33	PG	outer volume shell temp	Minco TT176 PD1N	0-50C	4-20mA
TE-34	W	chiller return temperature	Minco S17624PDZT36B		100 ohm
TE-35	W	chiller supply temperature	Minco S17624PDZT36B		100 ohm
PT-41	PG	hydraulic pump pressure	Noshok 100-500-2-1-2-1	500 PSIG	4-20mA
PT-43	PG	hydraulic pump pressure	Noshok 100-500-2-1-2-1	500 PSIG	4-20mA
PI-44	V	vacuum pump inlet	McMaster 38465K11	-30"Hg-0 psig	none
PI-45	PG	degassing chamber	Noshok 500 series	-30"Hg-0 psig	none
FS-46	PG	hydraulic pump flow switch	Ameritrol IX-1875	directional	contact
FS-47	PG	hydraulic pump flow switch	Ameritrol IX-1876	directional	contact

FI-50	W	chiller return flow	Orange 2421FG-1-E-2.5-B	10 GPM	none
PI-54	A	Accumulator charge pressure	US Gage brass, 2.5" diameter	0-400 psig	none
FI-55	PG	Sight glass degassing tank top fill	LDI industries F155	visual only	none
PI-74	A	degassing tank dry gas backfill	US Gage brass, 2.5" diameter	-30"Hg-0-30 psi	none
PT-83	C3F8	bubble chamber pressure	Noshok 612-300-2-1-T-20’	300 PSIG	4-20mA
TE-84	W	outer vessel temperature	Minco S17624PDZT36B		100 ohm
TS-85	W	outer vessel temperature	Minco CT325 PD 2 C 1-20	70C	
TE-86	W	outer vessel temperature	Minco S17624PDZT36B		100 ohm
TS-87	W	outer vessel temperature	Minco CT325 PD 2 C 1-20	70C	
PI-90	W	Water system pressure	Ashcroft	-30-0-+100	none
TE-91	W	Water temperature	Omega HSRTD-3-100-A-240-E		100 ohm
TE-92	W	Water temperature	Omega HSRTD-3-100-A-240-E		100 ohm
TE-93	W	Water temperature	Omega HSRTD-3-100-A-240-E		100 ohm
TE-94	W	Water temperature	Omega HSRTD-3-100-A-240-E		100 ohm
TE-95	W	Water temperature	Omega HSRTD-3-100-A-240-E		100 ohm
TE-96	W	Water temperature	Omega HSRTD-3-100-A-240-E		100 ohm
TE-97	W	Water temperature	Omega HSRTD-3-100-A-240-E		100 ohm
TE-98	W	Water temperature	Omega HSRTD-3-100-A-240-E		100 ohm

Table B.1: A full list of all the instrumentation in PICO-60 except the cameras. along with their manufacturer, model and function. PG stands for propylene glycol / MEG, W stands for water, V for vacuum and A for air.